LBL--16347-Vol.1

DE91 015477

FRACTURE DETECTION IN CRYSTALLINE ROCK USING ULTRASONIC REFLECTION TECHNIQUES
Volume I

Stephen P. Palmer

Lawrence Berkeley Laboratory
University of California
Berkeley, California 94720

November 1982

This work was supported, in part, by the Assistant Secretary for Nuclear Energy, Office of Waste Isolation of the U.S. Department of Energy under Contract Number DE-AC03-76SF00098. Funding for this project is administered by the Office of Nuclear Waste Isolation at Battelle Memorial Institute.

The United States Department of Energy has the right to use this thesis for any purpose whatsoever including the right to reproduce all or any part thereof.

MASTER

Fracture Detection in Crystalline Rock Using Ultrasonic Reflection Techniques

Copyright © 1982

by

Stephen Philip Palmer

PREFACE

This report is one of a series documenting the results of the Swedish-American cooperative research program in which the cooperating scientists explore the geological, geophysical, hydrological, geochemical, and structural effects anticipated from the use of a large crystalline rock mass as a geologic repository for nuclear waste. This program has been sponsored by the Swedish Nuclear Power Utilities through the Swedish Nuclear Fuel Supply Company (SKBF), and the U.S. Department of Energy (DOE) through the Lawrence Berkeley Laboratory.

The principal investigators are L.B. Nilsson and O. Degerman for SKBF, and N.G.W. Cook, P.A. Witherspoon, and J.E. Gale for LBL. Other participants will appear as authors of the individual reports.

Previous technical reports in this series are listed below.

1. Swedish-American Cooperative Program on Radioactive Waste Storage in Mined Caverns by P.A. Witherspoon and O. Degerman. (LBL-7049, SAC-01).

2. Large Scale Permeability Test of the Granite in the Stripa Mine and Thermal Conductivity Test by Lars Lundstrom and Haken Stille. (LBL-7052, SAC-02).

3. The Mechanical Properties of the Stripa Granite by Graham Swan. (LBL-7074, SAC-03).

4. Stress Measurements in the Stripa Granite by Hans Carlsson. (LBL-7078, SAC-04).

5. Borehole Drilling and Related Activities at the Stripa Mine by P.J. Kurfurst, T. Hugo-Persson, and G. Rudolph. (LBL-7080, SAC-05).

6. A Pilot Heater Test in the Stripa Granite by Hans Carlsson. (LBL-7086, SAC-06).

7. An Analysis of Measured Values for the State of Stress in the Earth's Crust by Dennis B. Jamison and Neville G.W. Cook. (LBL-7071, SAC-07).

8. Mining Methods Used in the Underground Tunnels and Test Rooms at Stripa by B. Andersson and P.A. Halen. (LBL-7081, SAC-08).

9. Theoretical Temperature Fields for the Stripa Heater Project by T. Chan, Neville G.W. Cook, and C.F. Tsang. (LBL-7082, SAC-09).

10. Mechanical and Thermal Design Considerations for Radioactive Waste Repositories in Hard Rock. Part I: An Appraisal of Hard Rock for Potential Underground Repositories of Radioactive Waste by N.G.W. Cook; Part II: In Situ Heating Experiments in Hard Rock: Their Objectives and Design by N.G.W. Cook and P.A. Witherspoon. (LBL-7073, SAC-10).

11. Full-Scale and Time-Scale Heating Experiments at Stripa: Preliminary Results by N.G.W. Cook and M. Hood. (LBL-7072, SAC-11).

12. Geochemistry and Isotope Hydrology of Groundwaters in the Stripa Granite: Results and Preliminary Interpretation by P. Fritz, J.F. Barker, and J.E. Gale. (LBL-8285, SAC-12).

13. Electrical Heaters for Thermo-Mechanical Tests at the Stripa Mine by R.H. Burleigh, E.P. Binnall, A.O. DuBois, D.O. Norgren, and A.R. Ortiz. (LBL-7063, SAC-13).

14. Data Acquisition, Handling, and Display for the Heater Experiments at Stripa by Maurice B. McEvoy. (LBL-7063, SAC-14).

15. An Approach to the Fracture Hydrology at Stripa: Preliminary Results by J.E. Gale and P.A. Witherspoon. (LBL-7079, SAC-15).

16. Preliminary Report on Geophysical and Mechanical Borehole Measurements at Stripa by P. Nelson, B. Paulsson, R. Rachiele, L. Andersson, T. Schrauf, W. Hustrulid, O. Duran, and K.A. Magnussen. (LBL-8280, SAC-16).

17. Observations of a Potential Size-Effect in Experimental Determination of the Hydraulic Properties of Fractures by P.A. Witherspoon, C.H. Amick, J.E. Gale, and K. Iwai. (LBL-8571, SAC-17).

18. Rock Mass Characterization for Storage in Nuclear Waste in Granite by P.A. Witherspoon, P. Nelson, T. Doe, R. Thorpe, B. Paulsson, J.E. Gale, and C. Forster. (LBL-8570, SAC-18).

19. Fracture Detection in Crystalline Rock Using Ultrasonic Shear Waves by K.H. Waters, S.P. Palmer, and W.F. Farrell. (LBL-7051, SAC-19).

20. Characterization of Discontinuities in the Stripa Granite--Time Scale Heater Experiment by R. Thorpe. (LBL-7083, SAC-20).

21. Geology and Fracture System at Stripa by A. Okliewicz, J.E. Gale, R. Thorpe, and B. Paulsson. (LBL-8907, SAC-21).

22. Calculated Thermally Induced Displacements and Stresses for Heater Experiements at Stripa by T. Chan and N.G.W. Cook. (LBL-7061, SAC-22).

23. Validity of Cubic Law for Fluid Flow in a Deformable Rock Fracture by P.A. Witherspoon, J. Wang, K. Iwai, and J.E. Gale. (LBL-9557, SAC-23).

24. Determination of In-Situ Thermal Properties of Stripa Granite from Temperature Measurements in the Full-Scale Heater Experiments: Methods and Primary Results by J. Jeffry, T. Chan, N.G.W. Cook and P.A. Witherspoon. (LBL-8424, SAC-24).

25. Instrumentation Evaluation, Calibration, and Installation for Heater Tests Simulating Nuclear Waste in Crystalline Rock, Sweden by T. Schrauf, H. Pratt, E. Simonson, W. Hustrulid, P. Nelson, A. DuBois, E. Binnall, and R. Haught. (LBL-8313, SAC-25)

26. Part I: Some Results From a Field Investigation of Thermo-Mechanical Loading of a Rock Mass When Heater Canisters are Emplaced in the Rock by M. Hood. Part II: The Application of Field Data from Heater Experiments Conducted at Stripa, Sweden for Repository Design by M. Hood, H. Carlsson, and P.H. Nelson. (LBL-9392, SAC-26).

27. Progress with Field Investigations at Stripa by P.A. Witherspoon, N.G.W. Cook, and J.E. Gale (LBL-10559, SAC-27).

28. A Laboratory Assessment of the Use of Borehole Pressure Transients to Measure the Permeability of Fractured Rock Masses by C.B. Forster and J.E. Gale. (LBL-8674, SAC-28).

29. Thermal and Thermomechanical Data for In Situ Heater Experiments at Stripa, Sweden by T. Chan, E. Binnall, P. Nelson, O. Wan, C. Weaver, K. Ang, J. Braley, and M. McEvoy. (LBL-11477, SAC-29).

30. The Effect of Radon Transport in Groundwater Upon Gamma Ray Borehole Logs by P.H. Nelson, R. Rachiele, and A. Smith. (LBL-11180, SAC-30).

31. Strength and Permeability Tests on Ultra-Large Stripa Granite Core by R. Thorpe, D.J. Watkins, W.E. Ralph, R. Hsu, and S. Flexser. (LBL-11203, SAC-31).

32. Ultrasonic and Acoustic Emission Results from the Stripa Heater Experiments. Part I: A Cross-Hole Investigation of a Rock Mass Subjected to Heating by B.N.P. Paulsson and M.S. King. Part II: Acoustic Emission Monitoring During Cool-Down of the Stripa Heater Experiment by R. Rachiele. (LBL-10975, SAC-32).

33. Numerical Modeling to Assess Possible Influence of the Mine Openings on Far-Field In Situ Stress Measurements at Stripa by T. Chan, V. Guvanasen, and N. Littlestone (LBL-12469, SAC-33).

34. A Field Assessment of the Use of Borehole Pressure Transients to Measure the Permeability of Fractured Rock Masses by C.B. Forster and J.E. Gale. (LBL-11829, SAC-34).

35. Water Inflow into Boreholes During the Stripa Experiments by P.H. Nelson, R. Rachiele, J.S. Remer and H.S. Carlsson (LBL-12547, SAC-35).

36. Petrology and Radiogeology of the Stripa Pluton by H. Wollenberg, S. Flexser, and L. Andersson. (LBL-11654, SAC-36).

37. Geohydrological Data from the Macopermeability Experiment at Stripa, Sweden by C.R. Wilson, J.C.S. Long, R.M. Galbraith, K. Karasaki, H.K. Endo, A.O. DuBois, M.J. McPherson, and G. Ramqvist. (LBL-12520, SAC-37).

38. Characterization of Discontinuities in the Stripa Granite--Full-Scale Heater Experiments by B.N.P. Paulsson, P.H. Nelson, and P.J. Kurfurst. (LBL-9063, SAC-38).

39. Application of Borehole Geophysics at an Experimental Waste Storage Site by P.H. Nelson, K.A. Magnusson, and R. Rachiele. (LBL-11982, SAC-39).

40. Laboratory Investigations of Thermomechanical Properties of Stripa Granite by L. Myer and R. Rachiele. (LBL-13435, SAC-40)

41. Petrologic Changes and Damage in the Stripa Quartz Monzonite in Response to Heater Tests by S. Flexser, H. Wollenberg, and D.E. Wedge. (LBL-14929, SAC-41).

42. Fracture Mapping in the Ventilation Drift at Stripa: Procedures and Results by A. Rouleau, J.E. Gale, and J. Galeshta. (LBL-13071, SAC-42).

43. Thermal Analysis of the Stripa Heater Test Data from the Full Scale Drift by I. Javandel and P.A. Witherspoon. (LBL-13217, SAC-43).

44. In Situ Stress Measurements at the Stripa Mine, Sweden by T.W. Doe, K. Ingevald, L. Strindell, B. Leijon, W. Hustrulid, A. Tarikka, M. Holmberg, E. Majer, and H. Carlsson. (LBL-15009, SAC-44).

EDITOR'S NOTE

One of the difficult problems at Stripa was to detect the presence of fractures within the rock mass. The present work presents new results on a method of fracture detection using ultrasonic reflection techniques and reveals the power of this approach. These results, when properly applied, will be an important component of site characterization work on crystalline rock masses.

Fracture Detection in Crystalline Rock Using Ultrasonic Reflection Techniques

By

Stephen Philip Palmer

A.B. (University of California) 1974
M.S. (University of California) 1978

DISSERTATION

Submitted in partial satisfaction of the requirements for the degree of

DOCTOR OF PHILOSOPHY

in

Engineering Science

in the

GRADUATE DIVISION

OF THE

UNIVERSITY OF CALIFORNIA, BERKELEY

Approved: ..... Chair ..... Date 11 Nov 82

..... Nov. 11, 82

.... Chi-yuen Wang ... Nov. 11, 82

.....

FRACTURE DETECTION IN CRYSTALLINE ROCK USING ULTRASONIC REFLECTION TECHNIQUES

Stephen Philip Palmer

Abstract

This research was initiated to investigate using ultrasonic seismic reflection techniques to detect fracture discontinuities in a granitic rock. Initial compressional (P) and shear (SH) wave experiments were performed on a 0.9 × 0.9 × 0.3 meter granite slab in an attempt to detect seismic energy reflected from the opposite face of the slab. It was found that processing techniques such as deconvolution and array synthesis could improve the standout of the reflection event.

During the summers of 1979 and 1980 SH reflection experiments were performed at a granite quarry near Knowles, California. The purpose of this study was to use SH reflection methods to detect an *in situ* fracture located one to three meters behind the quarry face. These SH data were later analyzed using methods similar to those applied in the laboratory. Interpretation of the later-arriving events observed in the SH field data as reflections from a steeply-dipping fracture was inconclusive.

Subsequent laboratory experiments showed that the shear velocity of the granite increases from 10-20% when going from a dry to water-saturated condition, and that the shear attenuation constant decreases by a factor of three under these conditions. An artificial fracture was created by shimming two granite slabs to give a 1.5 millimeter air

gap. P and SH reflection data recorded prior to and after filling the gap with water confirmed previous theoretical predictions concerning reflection from a fluid-filled fracture. While keeping the gap water-filled, advances in the SH reflection arrival time monitored over the following week indicated that water was absorbed a minimum of 10 centimeters into the granite slab. The most likely interpretation of the SH field data is that the later-arriving events are Love waves that result from a low velocity surface layer created by drying of the granite during the hot, dry California summer.

Thomas V. McEvilly
Chairman, Thesis Committee
11 Nov 82

Table of Contents

		pages
Acknowledgements		ii-iii
Chapter I	Introduction	1-4
References		5-6
Chapter II		
Section 1	Preliminary Theoretical Considerations	7-24
Section 2	Description of the Experimental System	25-39
Section 3	Initial SH Experiments	40-80
Section 4	Initial P Experiments	81-96
Section 5	Conclusions	97-98
References		99-100
Chapter III		
Section 1	Introduction	101-116
Section 2	Field Experiments at the Shaw Quarry	117-152
Section 3	Conclusions	153-155
References		156
Chapter IV		
Section 1	Introduction	157-158
Section 2	P and S Velocities of Raymond Granite	159-169
Section 3	Water Gap Experiment #1	170-195
Section 4	Water Gap Experiment #2	196-257
Section 5	Phase Spectra and Arrival Time Analysis	258-284
Section 6	Conclusions	285-288
References		289
Chapter V		
Section 1	Reexamination of the Field Work at the Shaw Quarry	290-308
Section 2	Final Statements	309-317
References		318
Appendix I		319-321
Appendix II		322-337
References		338

Acknowledgements

First, I would like to thank my parents for their encouragement and support during this ordeal. Without their help the following manuscript would not have been completed.

It was my great priviledge to work with Kenneth H. Waters during his various visits to Berkeley as a Phoebe Apperson Hearst lecturer. Indeed it was Ken's suggestions and support that motivated this research.

I would like to thank Shimon Coen, Bill Farrell, and Frank Morrison for their aid and assistance in my education process. I would especially like to express my gratitude to Mike King and Tom McEvilly for encouraging me during the low points of this research, and for their many worthwhile suggestions and discussions.

Many friends contributed to this work through their enthusiasm and support. My thanks to all of them (you know who you are). Special appreciation goes to good friend and colleague Mike Hoversten for many stimulating discussions during lunch. Many thanks are due to Dave Aldridge and Lynn Moses for their efforts as the field crew during the experiments at the Shaw quarry.

The first portion of this research was performed with funds provided by the Swedish-American Cooperative Program on Radioactive Waste Storage in Mined Caverns in Crystalline Rock through the Lawrence Berkeley Laboratory under University of California contract W-7405-ENG-48. Many thanks to Phil Nelson for his support of this research project.

Financial support and tuition payments were provided by the Jane Lewis Fellowship and the Domestic Mining and Mineral and Mineral Fuel Conservation Fellowship, sponsored by the Department of Health, Education, and Welfare.

The students in the Engineering Geoscience group contributed moral support amidst the trials and tribulations of academic life. Special thanks to Jim Jardine and Joe Lamb for their invaluable assistance in this project, and to Richie V. Lukes for the excellent fabrication of the support racks used in the field study.

I would like to thank Joe Peters of the Cold Springs Granite Company, and especially Bob Warnert of the Raymond Granite Company, for their assistance in obtaining a suitable site for the field study. Also, my thanks to Jeanne Larson and Don Duncan of the United States Forest Service for providing accommodations during the field study at the nearby San Joaquin Experimental Range. Also many thanks to Paula Conant for typing the final version of this manuscript.

Finally, I would like to dedicate this work to anyone who thinks that the outcome of a previously unperformed experiment can be successfully predicted in all cases.

CHAPTER I

Introduction

The permeability of a crystalline rock body is controlled primarily by the presence of interconnected fractures within the body. Thus, accurate determination of the location and orientation of discrete fractures within a rock mass would be extremely useful information for hydrologists involved in estimating permeability and other hydraulic parameters. Information regarding the nature of the material filling the fractures is also desirable, as water flow is usually confined to "open" fractures (i.e. those fractures not completely filled by calcite, epidote, clay, etc.). The detection of fractures and other geological discontinuities near the working face of a mine or tunnel would also aid in the prediction of roof collapse and other mine safety problems. In fact, most fatal mining accidents occur in areas of advancing or development work, and most fatal roof-fall accidents occur within ten feet of the working face (Mongan and Miller, 1962).

The purpose of this research is to develop a high-frequency seismic reflection system that can detect fracture discontinuities within a crystalline rock mass. Besides being able to detect the position and orientation of the fracture plane, it is also desired that the nature of the fracture interstitial material be determined from analysis of the reflection data. The ultrasonic reflection system developed during this research was tested under various laboratory conditions so that its limitations could be determined. The applicability of these reflec-

tion methods to fracture detection in an ideal field situation was tested at a local granite quarry. Unfortunately, no field application in an underground environment could be conducted because of the limitations of the research project.

The development of a physical system capable of generating interpretable ultrasonic seismic reflection data is described in Chapter II. Both compressional (P) and horizontally polarized shear (SH) wave reflection data were obtained under various laboratory conditions, and a number of signal processing techniques were used to simplify the analysis of the reflection data. In Chapter III the results of a field test are presented in which an attempt was made to detect a naturally occurring, in situ fracture using the reflection techniques developed in the laboratory. The results of this field test suggested that a series of laboratory experiments be conducted to study the effect of different interstitial fluids (air or water) on the reflection of P and SH waves from a planar fracture. These experiments are described in detail in Chapter IV. In Chapter V the results of the field experiment are examined in light of the results of the laboratory fracture study. A reevaluation of the field experiment is presented, as well as conclusions regarding the practicality of this technique for fracture detection in an underground environment.

Some of the earliest references in the geophysical literature relevant to this study are the results of a number of seismic modeling experiments published in the mid-1950's (e.g. Levin and Hibbard, 1955; Evans, 1959). In these experiments low-frequency (1 to 100 Hz) seismic wave propagation in a layered earth is modeled using laboratory scale

physical models and a consequently higher frequency band (10 to 300 kHz). The results of these studies have shown that easily interpretable P and SH reflection data can be obtained at ultrasonic frequencies on a number of simple laboratory models. Indeed, this sort of seismic scale modeling is presently an area of active geophysical research, especially with regard to its application in petroleum exploration seismology (Dampney, Mohanty, and West, 1972; Waters, Palmer, and Farrell, 1978; Palmer, Smith, and Waters, 1981; Tatham, Goolsbee, Massell, and Nelson, 1981).

The application of ultrasonic reflection methods to fracture detection in a mining environment was initially studied during the late 1950's (Szendrei and Lochner, 1958; Lutsch, 1959). Further research into practical applications of the technique continued into the mid-1970's, meeting with limited success in the detection of in situ fractures (Yu, 1967; Gupta, 1972; Yu and Telford, 1973). However, at least one private company has been able to demonstrate the commercial use of an ultrasonic reflection method in the site planning of an underground construction project (Price, 1973). A more recent reference presents a successful case study in which a number of sandstone and sylvite beds were detected within a salt dome using a sonar (acoustic reflection) system (Unterberger, 1978).

All of the previously mentioned studies involved with in situ fracture detection have used only compressional (P) wave reflection techniques. Certain theoretical and practical considerations, which will be elaborated in Chapter II, suggest that a single, thin, water-filled fracture can be more easily detected using SH, rather than P wave, reflection methods. This research then represents the first

published attempt at using ultrasonic frequency SH reflection methods to detect *in situ* naturally occurring fractures.

References--Chapter I

Dampney, C. N. G., Mohanty, B. B., and West, G. F.; 1972; "A Calibrated Model Seismic System"; Geophys.; V. 37; No. 3; pp. 445-455.

Evans, J. F., 1959; "Seismic Model Experiments with Shear Waves"; Geophys.; V. 24; No. 1; pp. 40-48.

Gupta, R. R.; 1972; "Seismic Determination of Geological Discontinuities Ahead of Rapid Excavation"; Advanced Research Projects Agency Report No. 6311; 82 pp.

Levin, F. K. and Hibbard, H. D.; 1955; "Three-Dimensional Seismic Model Studies"; Geophys.; V. 20; No. 1; pp. 19-32.

Lutsch, A.; 1959; "The Experimental Determination of the Extent and Degree of Fracture of Rock Faces by Means of an Ultrasonic Pulse Reflection Method"; Journal of South African Institute of Mining and Metallurgy; V. 59; No. 8; pp. 412-429.

Mongan, C. E. and Miller, T. C.; 1962; "Use of Sonic Techniques in Exploring Coalmine Roof Strata: A Progress Report"; International Symposium on Mining Research; Univ. of Missouri; V. 2; pp. 669-679.

Palmer, S. P., Smith, J. A., and Waters, K. H.; 1981; "Fracture Detection in Crystalline Rocks Using Ultrasonic Reflection Techniques"; Intl. Journ. of Rock Mechanics and Mining Sciences; V. 18; No. 5; pp. 403-414.

Price, T. O.; 1975; "Demonstration of Acoustical Underground Survey System in the Washington Metropolitan Area"; Federal Highway Administration Report No. FHWA-RD-75-82; 106 pp.

Szendrei, M. S. and Lochner, J. P. A.; 1958; "The Determination of the Extent of Fracture of Rock Faces by Some Means"; Journal of South African Institute of Mining and Metallurgy; V. 59; No. 4; pp. 202-214.

Tatham, R. H., Goolsbee, D. V., Massell, W. F., and Nelson, H. R.; 1981; "Seismic Shear Wave Observations in a Physical Model Experiment"; Presented in Oct., 1981 at the 51st Annual International Meeting of the Society of Exploration Geophysicists.

Unterberger, R. R.; 1978; "Radar and Sonar Probing of Salt"; Paper presented at the 5th International Salt Symposium; Hamburg, Germany; May, 1978.

Waters, K. H., Palmer, S. P., and Farrell, W. E.; 1978; "Fracture Detection in Crystalline Rock Using Ultrasonic Shear Waves"; L.B.L. Report 7051; 46 pp.

Yu, Thiann-Ruey; 1967; "Ultrasonic System for Fracture Detection in Rock Faces"; Submitted in partial fulfillment of the requirements of the M. Eng. degree; McGill University; 103 pp.

Yu, T. R. and Telford, W. M.; 1973; "An Ultrasonic System for Fracture Detection in Rock Faces"; Canadian Mining and Metallurgical Bulletin; V. 66; No. 1; pp. 96-101.

CHAPTER II

Section 1

Preliminary Theoretical Considerations

Prior to assembling the physical components of the ultrasonic reflection system, it was necessary to establish the theoretical behavior of compression (P) and horizontally polarized shear (SH) wave reflection from a simple fracture model. The results of this study suggest that SH reflection techniques are superior to P wave methods in detecting thin, water-filled fractures. However, determination of the interstitial fluid of the fracture (air or water) is only possible using P wave reflection data. Thus, the results of this study encouraged the development of both P and SH reflection systems.

Treatment of the source-free elastodynamic wave equation in an isotropic, homogeneous, linear elastic whole space frequently involves methods that separate the compressional (P) and shear (S) components of the vector displacement. The source-free elastodynamic wave equation can be written:

$$\rho \frac{\partial^2 \bar{u}}{\partial t^2} = (\lambda+\mu)\nabla[\nabla\cdot\bar{u}] + \mu\nabla^2\bar{u} \qquad \text{[II.1.1]}$$

where ρ = the density of the medium, λ = the Lame parameter of the medium, μ = the shear modulus of the medium, and $\bar{u}$ the vector displacement. In a Cartesian coordinate system the component of motion can be determined by starting with the vector identity:

$$\nabla^2\bar{u} = \nabla[\nabla\cdot\bar{u}] - \nabla\times[\nabla\times\bar{u}]$$

Substituting this into II.1.2, then:

$$\rho\frac{\partial^2\bar{u}}{\partial t^2} = (\lambda+2\mu)\nabla[\nabla\cdot\bar{u}] - (\nabla\times[\nabla\times\bar{u}])\mu \qquad \text{[II.1.2]}$$

To obtain the P wave equation of motion, let $\theta = \nabla\cdot\bar{u}$, and taking the divergence of II.1.2;

$$\rho\frac{\partial^2\theta}{\partial t^2} = (\lambda+2\mu)\nabla^2\theta \qquad \text{[II.1.3a]}$$

Compressional (P) waves then propagate with a velocity $\alpha = \sqrt{\frac{\lambda+2\mu}{\rho}}$

In order to determine the shear (S) wave equation of motion, let $\bar{\Omega} = \nabla\times\bar{u}$, and taking the curl of Equation II.1.1, then:

$$\rho\frac{\partial^2\bar{\Omega}}{\partial t^2} = u\nabla^2\bar{\Omega} \qquad \text{[II.1.3b]}$$

where the identity $\nabla\times[\nabla[\nabla\cdot\bar{u}]] = \bar{0}$ is used. Shear (S) wave then propagate with velocity $\beta = \sqrt{\mu/\rho}$, where $\beta < \alpha$.

Figure II-1-1 depicts a monochromatic plane elastic wave propagating through a linear, isotropic whole space. The total displacement of a plane elastic wave $\bar{u}$ can be separated into its compressional u_p and shear u_s components, as shown in this figure. As a matter of convenience the Cartesian coordinate system is defined so that the unit wave normal $\bar{\nu}$ lies in the x_1 - x_3 plane. The shear displacement can then be separated into its vertical (SV) and horizontal (SH) components.

This separation of the vector components in a Cartesian coordinate system is very useful in practical seismic reflection applications where the sub-surface reflectors are nearly parallel to the ground (observation) surface.

In the following analysis a fracture is modeled as a thin, planar layer filled with a material having elastic properties different from those of the surrounding medium. We consider first the normal incidence reflection of a plane P wave of frequency ω from a thin planar layer of thickness d, density ρ_1, and P wave velocity α_1 located in a homogenous, elastic whole-space of density ρ and P wave velocity α. This simple fracture model is shown in Figure II-1-2, and the analysis of this problem is taken from Rayleigh, 1945.

The solution to this problem is usually presented as a complex reflection coefficient R_α, which is the ratio of the displacements of the incident and reflected plane P waves measured at $x_3 = 0$. For this particular geometry, the complex reflection coefficient is:

$$R_\alpha = (z/z_1 - z_1/z)/(z/z_1 - z_1/z + 2i\cot\left(\frac{\omega d}{\alpha_1}\right)) \qquad \text{[II.1.4]}$$

where $z = \rho\alpha$ and $z_1 = \rho_1\alpha_1$.

R_α can be resolved into its amplitude $|R_\alpha|$ and phase ϕ_α spectra, which are presented in the following two equations.

$$|R_\alpha| = \left[\frac{(z/z_1 - z_1/z)^2}{(z/z_1 - z_1/z)^2 + 4\cot^2(\omega d/\alpha_1)}\right]^{1/2} \qquad \text{[II.1.5]}$$

$$\phi_\alpha = \tan^{-1}\left[\frac{-2\cot\left(\frac{\omega d}{\alpha_1}\right)}{(z/z_1 - z_1/z)}\right] \qquad \text{[II.1.6]}$$

It should be noted that this solution is equally valid for plane SH waves normally incident on the thin layer if the P wave velocities α and α_1 are replaced by the corresponding S wave velocities β and β_1. For example, the amplitude spectrum of the complex SH reflection coefficient is:

$$|R_\beta| = \left[\frac{(z/z_1 - z_1/z)^2}{(z/z_1 - z_1/z)^2 + 4\cot^2(\omega d/\beta_1)}\right]^{1/2} \qquad \text{[II.1.7]}$$

where $z = \rho\beta$ and $z_1 = \rho_1\beta_1$.

Since the objective of this research is concerned with fracture detection in crystalline (granitic) rock, the velocity and density values used for the surrounding medium were selected as typical values for a Raymond granite, i.e., β = 2500 m/s, α = 4235 m/s, and ρ = 2.75 gm/cm^3. Four different substances (air, water, calcite, and quartz) will be considered as interstitial material for the fracture. The P and S wave velocities and densities for these materials are summarized in Table II-1-1. Also, four different fracture thicknesses (0.1, 0.5, 1.0, and 2.0 mm) are included as a variable in the analysis. All of the calculations of reflection amplitude spectra are derived using the results of the thin layer solution given in Equation II.1.5 and II.1.7.

When air is the fracture interstitial material, the reflection coefficient for both P and SH waves is for all purposes unity in the frequency band 1-200 kHz. The density of air at atmospheric pressure is very small, although the P wave velocity in air is significant (approximately 310 m/s). However, the S wave velocity in air is zero, as the shear modulus of any non-viscous fluid is zero.

Table II-1-1

Calcite*

$\rho = 2.71\ gm/cm^3$ $\alpha = 6230\ M/S$

$\beta = 4590\ M/S$

Quartz*

$\rho = 2.65\ gm/cm^3$ $\alpha = 6000\ M/S$

$\beta = 4390\ M/S$

Air

$\rho \approx 0$ $\alpha \approx 300\ M/S$

$\beta = 0$

Water

$\rho = 1.0\ gm/cm^3$ $\alpha = 1500\ M/S$

$\beta = 0$

Raymond Granite

$\rho \approx 2.75\ gm/cm^3$ $\alpha = 4320\ M/S$

$\beta = 2500\ M/S$

*Values from Rzhevsky and Novik, 1971.

Because of this last result, then the reflection of SH waves from a water-filled fracture is also total, assuming that the small but finite viscosity of water can be neglected. This assumption seems reasonable in light of the work done by Fehler, 1979. Fehler's analysis is concerned with the reflection and transmission of plane SH waves normally incident on a viscous fluid layer. The viscosity is assumed to follow a Newtonian behavior, and the problem is solved assuming continuity of stress and displacement at all boundaries. Using a typical value for the viscosity of water, a frequency band of 1-200 kHz, and a variable fracture thickness of 0.1-0.2 mm, the results of Fehler's analysis indicate that the viscosity of water has a negligible effect on the SH reflection coefficient.

However, the plane P wave reflection coefficient of a water-filled fracture varies greatly as a function of frequency and fracture thickness, as can be seen in Figure II-1-3. Each of the four curves in this figure denote the amplitude spectrum of the P wave reflection coefficient over the frequency band of 1-200 kHz for fixed fracture thicknesses of 0.1, 0.5, 1.0, and 2.0 mm. The frequency and thickness dependence of the fracture reflection coefficient is due to the interference of the up- and down-going waves within the layer (fracture). This interference phenomenon is described mathematically in Equations II-1-(4 to 7), and the derivation of these equations is based on purely elastic theory. The results of Fehler's studies have shown that the small viscosity of water has negligible effect on the P wave reflection coefficient over the range of frequencies and thicknesses encountered in these experiments.

Figures II-1-(4a and b) are respectively the P and SH reflection amplitude spectra for a calcite-filled fracture over a similar frequency band and range of fracture thicknesses. Figures II-1-(5a and b) are similar presentations for the case in which the fracture is filled with quartz. Two notable observations may be made about the normal incidence reflection response of calcite and quartz-filled fractures:

1) The amplitude of the reflection coefficient is small for both minerals compared to that of an air or water-filled fracture.
2) The amplitude of the SH reflection coefficient is two or three times larger than the amplitude of the P reflection coefficient.

In theory, only P wave reflection data is needed to detect a subsurface fracture, be it filled with air, water, calcite, or quartz. In practical field applications, however, it is expected that limitations in the sensitivity of these techniques will cause fractures with small reflection coefficients (perhaps $|R_{\alpha,\beta}| < 0.1$) to be undetectable. Thus, SH reflection methods would seem perferable in detecting thin ($d \leq 0.5$ mm), water-filled fractures at seismic frequencies below 25 kHz. In this case, the use of both P and SH reflection data is required in order to differentiate between air or water as the particular interstitial fluid of the fracture. If the thin fracture is air-filled, both P and SH reflections could be detected, but if the fracture is water-filled then only the SH reflection would be large enough in amplitude to be detectable. In this practical case, calcite and quartz-filled fractures could not be detected because of their very small

reflection amplitudes. Thus, air and water will be the only fracture interstitial materials considered in this study.

Compressional (P) waves can be partially converted to vertically polarized shear (SV) waves when reflected at non-normal incidence from a planar boundary. Such a situation is shown in Figure II-1-6, in which an incident P wave is reflected from a free boundary as both P and SV waves. Mode conversions of this type then decrease the amplitude of the reflected P wave, as well as creating two reflected waves from a single incident wave. Mode conversion also occurs when a SH wave is reflected from a non-horizontal planar boundary (in which the strike line of the plane is not parallel to the direction of the SH displacement). In this case a reflected P and S wave (with both SV and SH components) are created from a single incident SH wave. For planar fractures with a shallow dip (less than 10° to 20°) the effect of mode conversion should not severely violate the assumption of horizontal reflection, but fractures with steeper dips will unquestionably present a severe practical limitation to use of these reflection techniques.

Based upon the previous analyses, it was decided that the primary emphasis of this research should be concerned with the detection of nearly horizontal fractures filled with either air or water using both P and SH reflection methods. Fractures filled with a solid material (e.g. quartz or calcite) were deemed a priori to be undetectable in a field situation (low frequencies) because of the very small reflection coefficients involved. However no experiments were conducted to investigate the actual reflection response of such solid-filled fractures.

Because any non-viscous fluid has zero shear strength (i.e., $\mu = 0$), then the reflection coefficient for a SH wave normally incident on a water-filled fracture is unity for all frequencies of interest in this study. However, in this same situation the P wave reflection coefficient varies considerably as a function of frequency and fracture thickness. In the case of an air-filled fracture, both the P and SH reflection responses are unity for frequencies in the band of 1-200 kHz. In theory, then it is possible to detect horizontal fluid-filled fractures of any reasonable thickness using SH reflection data, but the nature of the in filling fluid (air or water) cannot be determined from this data set alone.

Consider the case where the acoustic impedance z (product of the P velocity and density) of the upper half-space is known, but the thickness of the thin layer d and acoustic impedances of the thin layer and lower half-space (z_1 and z_2 respectively) are unknown. If the normal incidence plane P wave reflection coefficient of the thin layer can be measured over a sufficiently large band of frequencies, then in theory it is possible to determine the unknown parameters h, z_1, and z_2. In fact, it is necessary to obtain the P reflection coefficient at frequencies high enough so that the layer thickness h just equals a quarter wavelength of the incident wave in the layer. This high frequency condition may be expressed as:

$$f_m = \frac{\alpha_1}{4h} .$$

Taking h = 1 mm, and α_1 = 1500 m/s (from Table II-1-1 for a water-filled

fracture), then f_m = 375 kHz in this example. In a realistic field situation the distance that a P wave of frequency 375 kHz can propagate is severely limited by the effect of anelastic attenuation (see Chapter III, Section 1). Indeed, at 375 kHz a P wave can propagate only a few decimeters before anelastic attenuation has reduced the amplitude of the P wave below a detectable level. Thus, in a practical sense it is not possible to use the variation in the P reflection coefficient as a function of frequency to determine the unknown parameters h, z_1, and z_2 in a field study where the propagation distances are on the order of 1-10 m.

Since the P reflection response of a water-filled fracture depends strongly on frequency and fracture thickness, it is possible in theory to obtain the fracture thickness from the variation of the P reflection amplitude with frequency (after removal of the source spectrum) if the P velocity and density of the surrounding medium are known. If the fracture should be air-filled, then there will be no such variation with frequency, and the reflection should be total. Thus in theory it should be possible to detect a fracture and delineate the type of interstitial fluid (air or water) and fracture thickness (if filled with water) using only P wave reflection data. However, the P reflection coefficient for thin ($d < 0.5$ mm), water-filled fractures is small at lower frequencies, and it might not be practically possible to detect such thin fractures because of the small reflection amplitude. Then the development of both P and SH reflection systems seems justified if both the detection of thin fluid-filled fractures and the determination of the type of in-filling fluid (air or water) are design requirements. The following

sections in this chapter will then describe the development of both P and SH reflection systems.

Figure Captions

Figure II-1-1
Cartesian coordinate system used in separating shear and compressional components of the total displacement. $\underline{u}_p$ is the compressional component; u_s is the shear component. $\underline{\nu}$ is the wave normal of the plane wave. Shear wave motion u_s can be resolved into its vertical (SV) and horizontal (SH) components.

Figure II-1-2
Geometry used in the solution of the reflection response of a plane P wave normally incident on a thin, planar layer of thickness d. α_1, β_1, and ρ_1 are the P and S velocities and density, respectively, of the thin layer. α, β, and ρ are the P and S velocities and density, respectively, of the surrounding medium.

Figure II-1-3
Normal incidence P wave reflection coefficient as a function of frequency for a water-filled layer with thicknesses of 0.1, 0.5, 1.0, and 2.0 mm.

Figure II-1-4
Normal incidence P and SH reflection coefficients as a function of frequency for a calcite-filled layer with thicknesses of 0.1, 0.5, 1.0, and 2.0 mm.
a) P wave response (amplitude spectrum)
b) SH wave response (amplitude spectrum)

Figure II-1-5
Normal incidence P and SH reflection coefficients as a function of frequency for a quartz-filled layer with thicknesses 0.1, 0.5, 1.0, and 2.0 mm.
a) P wave response (amplitude spectrum)
b) SH wave response (amplitude spectrum)

Figure II-1-6
Mode conversion of an incident compressional wave on a plane with a unity reflection coefficient. α and β are the P and S velocities of the medium, and Snell's law is used to determine the angles θ_i, θ_r, and ϕ_r.

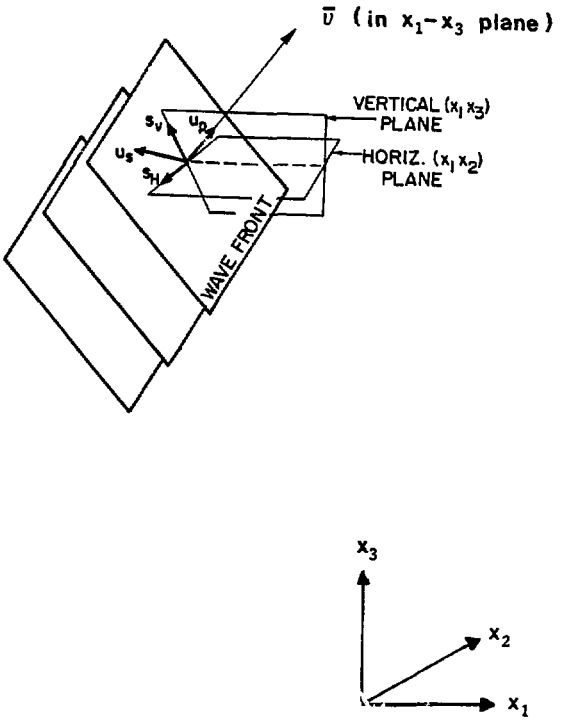

Figure II-1-1 XBL-837-1941

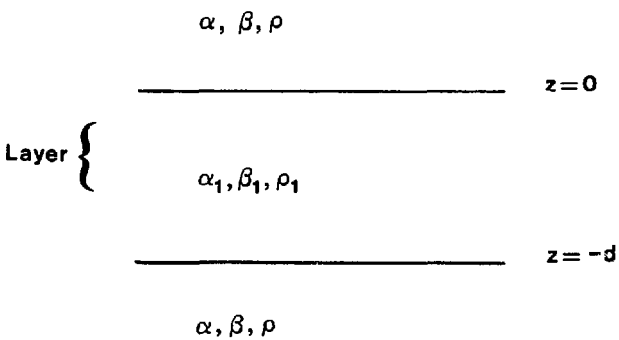

XBL 837-1942

Figure II-1-2

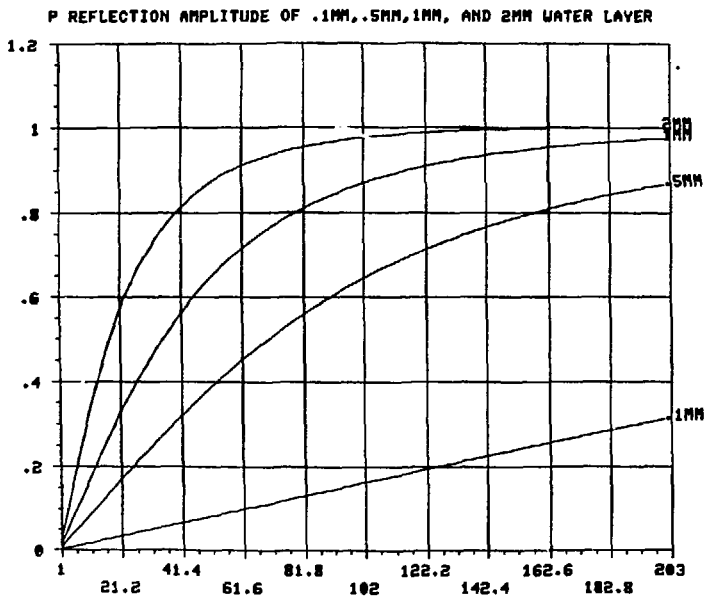

XBL 837-1943

Figure II-1-3

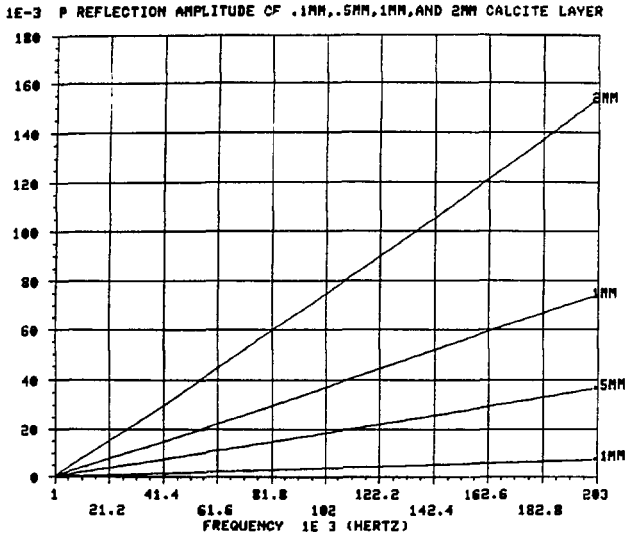

Figure II-1-4a

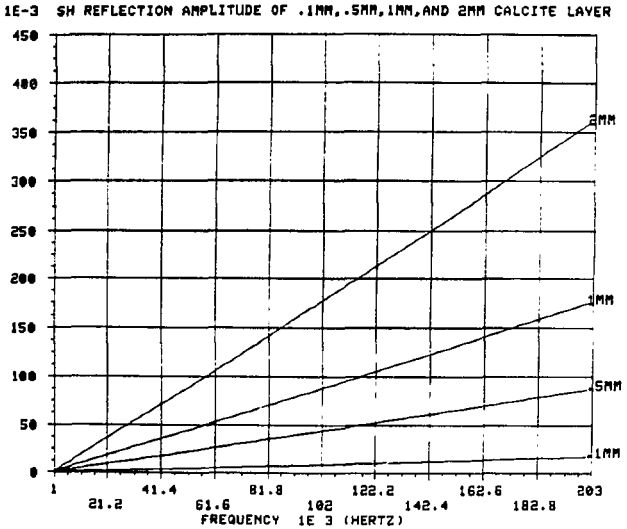

Figure II-1-4b

XBL 837-1944

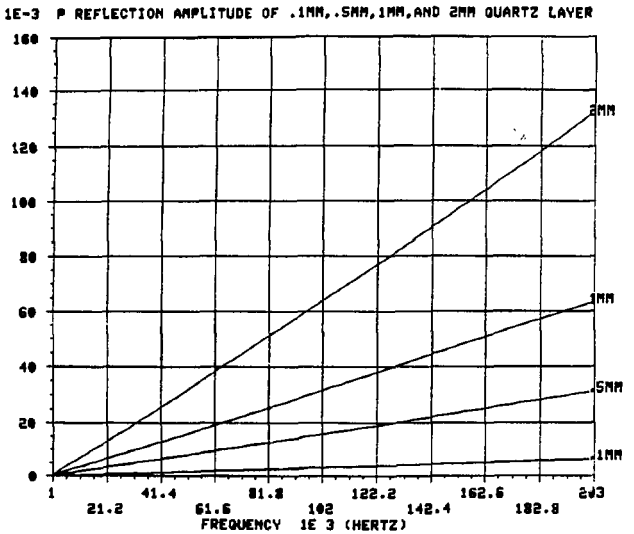

Figure II-1-5a

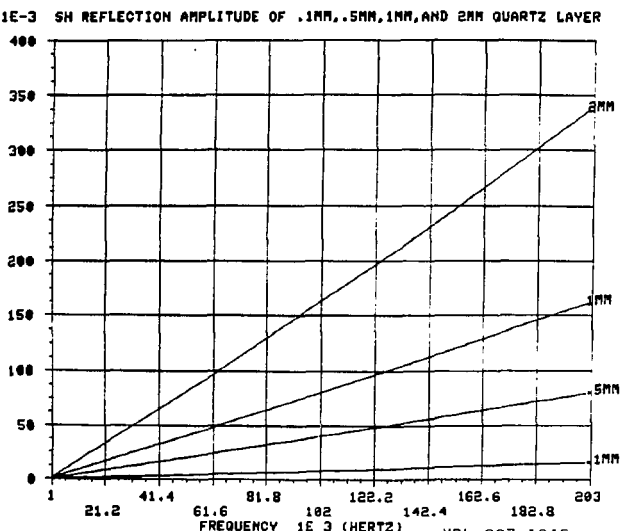

XBL 837-1945

Figure II-1-5b

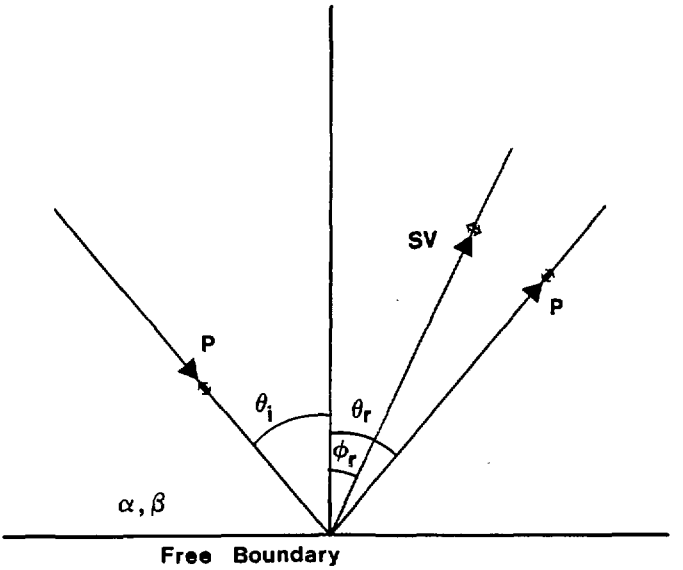

Snell's Law

$$\frac{\sin\theta_i}{\alpha} = \frac{\sin\theta_r}{\alpha} = \frac{\sin\phi_r}{\beta}$$

XBL 837-1946

Figure II-1-6

CHAPTER II

Section 2

Description of the Experimental System

Descriptions of the equipment and methods used to generate P and SH reflection data in the ultrasonic frequency band are presented in this section. The techniques used in the laboratory and field experiments are practically identical although the focus of this section will be concerned with the laboratory procedure. There is a great deal of similarity, usually intentional, in the reflection techniques developed in this study and those used in ultrasonic testing of metals and other materials. An excellent review of the ultrasonic testing of materials and flaw detection in metals is given in Banks, Oldfield, and Rawding, 1962, and Krautkramer, et al., 1969. The display and analysis of the laboratory P and SH reflection data will be described later in this chapter.

The generation and reception of elastic waves in these experiments is performed using transducers made from a common piezoelectric material, namely lead zinconate-titanate. The strain and electric displacement fields are coupled in a piezoelectric material, so that the deformation of such a material by external mechanical stresses will cause an electrical charge to be produced on the surface. This phenomenon is also reversible, so that application of an electrical potential across the solid will cause a physical deformation of the piezoelectric material. An excellent review of the piezoelectric phenomenon and its applications is presented in Mason, 1964.

In the laboratory experiments, a transient elastic wave is generated on the surface of a granite slab by applying a high voltage pulse of 1-3 μs duration across the surfaces of a piezoelectric plate that has been physically bonded to the rock surface. A schematic diagram of the experimental set-up is shown in Figure II-2-1. The transient elastic waves travel through the granite slab to a receiver, which uses the reversible nature of the piezoelectric phenomenon to convert the elastic motion of the granite surface into an electrical signal. This signal is amplified and displayed on an oscilloscope, and the seismic data (electrical signal) are then permanently recorded in either analog or digital form. Various signal processing techniques can then be applied prior to the analysis of these data.

A Velonix Model 350-R high power pulse generator produces the large voltage pulse used to excite the source piezoelectric plate. This particular model is capable of delivering a short (0.1 to 20 μs), high voltage (100-200 V) boxcar pulse into a 200 ohm resistive load with little edge distortion. The small capacitance of the piezoelectric plate does not seriously degrade the voltage pulse produced by the Velonix generator.

A Princeton Applied Research (PAR) Model 113 bandpass amplifier is used to amplify and filter the voltage signal from the receiver. This model amplifier has a variable gain of 20 to 80 dB, and a flat response (>3 dB loss) in the frequency band of 0-300 kHz. The receiver voltage signal is high-pass filtered at a corner frequency of 1 kHz using the standard PAR 113 internal bandpass filter. This is done in order to remove low frequency signals caused by building or wind vibra-

tion, 60 Hz electrical pick-up, etc. The amplified signal can then be displayed on any fast oscilloscope (1 MHz band or greater), using the leading edge of the high voltage pulse as the sync pulse.

In the initial phase of this research, a permanent record of the receiver signal was made using an X-Y plotter in conjunction with a boxcar integrator. The boxcar integrator, a PAR Model 162, performs an analog averaging of a repetitive signal. The averaging is performed slowly (at a controlled rate and over a controllable real-time span) so that the sweep rate of the oscilloscope is effectively reduced. The averaged signal can then be easily displayed on a standard X-Y recorder, in this case a Hewlett-Packard Model 7044A.

During the course of this research, the analog recording equipment was superceded by a more versatile digital recording system. The latter equipment is a Tektronix Model WP1200 waveform processing system controlled by a Digital Equipment Company (DEC) PDP 11/34 minicomputer. The Tektronix system has a high-speed A/D converter, a dual floppy-disc storage capability, and a graphics display terminal with a hardcopy printer. All of these devices are accessed through the PDP 11/34 using a version of Tektronix SPS BASIC. This digital acquisition capability facilitates the application of a number of signal processing techniques to the seismic data.

Piezoelectric ceramic materials are commercially available in plates that have an electrical response to deformation in only a given direction. Typically, this direction sensitivity is oriented either across or parallel to the largest faces of the plate (see Figure II-2-2). These types of plates are referred to as having a P or S orientation,

respectively. The source transducers used in these experiments are commercially available P or S piezoelectric plates that are epoxied to the surface of the granite slab (see Figure II-2-3). A conducting metal film is applied to the top and bottom faces of the plate to provide electrical contact for a pair of lead wires. After the epoxy has set, the source transducer can be connected to the pulse generator and operator.

A P wave source transducer expands in thickness when a step voltage is applied across the electrode faces (see Figure II-2-2a). This deformation creates a vertical traction (stress) between the plate and the material on which it is mounted. This traction causes an elastic wave to propagate into both materials. In the transducer this wave is reflected from the top and bottom surfaces, losing energy to the coupled medium (and the backing plate, if there is one), so that a damped reverberation takes place. These internal reflections may cause the elastic wavetrain radiated from the source to be very long and complex.

The P wave source transducers used in these experiments have circular faces with a diameter much larger than the plate thickness. Papers by Miller and Pursey, 1954 and 1956, and Bycroft, 1956, present solutions regarding the elastic radiation from a rigid, circular plate vibrating vertically on the surface of a homogeneous, isotropic, elastic half-space. Although the details of these solutions are dissimilar, there are important similarities in the type of elastic radiation described by each. Most notably, in the far-field both compressional and shear body waves radiate into the medium, and an evanescent surface wave, generally termed a Rayleigh wave, propagates along the surface of

the half-space. Indeed this general partition of elastic energy is observed when surface vibrators are used as seismic sources in petroleum exploration applications (Waters, 1981), and is also observed when a P type piezoelectric plate is used as a source transducer.

A quantitative analysis of the elastic radiation from a S type piezoelectric plate presents a more difficult problem. In these studies the S plate is square in shape, with the thickness much less than the side length of the largest faces. The piezoelectric orientation is chosen to be parallel to one edge of the square face, as can be seen in the photograph shown in Figure II-2-3b. Excitation of the S plate by a step voltage causes a rotational deformation of the plate about a horizontal axis, creating a horizontal traction between it and the material on which it is mounted (see Figure II-2-2b). A horizontally oriented stress wave is launched into both materials, and the consequent reverberation within the source plate creates a long and complex source wavelet.

In a paper by Cherry, 1962, the body and surface waves radiating from a horizontal stress applied at the surface of an elastic half-space are studied. Cherry's results use an asymptotic expansion for the Hankel functions $H_0^{'}(\xi r)$ and $H_1^{'}(\xi r)$ for large values of the argument ξr, and also assume that the horizontal source stress is distributed over a length small compared to the shortest wavelength emitted by the source. The radiation pattern of elastic waves produced by such a source must have a complex azimuthal dependence. The radiation pattern from this solution is least complicated in a vertical plane that bisects and is orthogonal to the applied horizontal stress. There is no vertical

angular dependence to the radiation pattern in this plane, and only shear waves with a SH orientation propagate in the far-field. The predominance of SH body wave propagation for this particular geometry is well demonstrated in a number of field experiments using mechanical devices to produce an approximation of a surface horizontal force (White, Heaps, and Lawrence, 1956; Jolly, 1956; Cherry and Waters, 1968; Erickson, Miller, and Waters, 1968).

The assumption that the horizontal source dimension is small compared to the shortest wavelength is not valid when a S piezoelectric plate is used in these experiments. However, the SH wavefield measured in the laboratory studies is very similar to that expected from theory, in which SH body wave propagation dominates in the far-field. Ultrasonic seismic sources constructed in these experiments from P and S piezoelectric plates produce elastic radiation patterns that reasonably approximate those expected from a small, distributed vertical or horizontal stress located on the surface of an elastic half-space.

In these experiments the ultrasonic seismic waves are detected using transducers that make use of the reversible nature of the piezoelectric phenomenon. To construct P or SH receivers, a very small P or S piezoelectric plate is mounted on the end of a long brass backing rod which provides mechanical support as well as an electrical contact for the positive lead. After insulating the brass rod, the whole transducer is covered with aluminum foil to provide an electrical ground shield (see Figure II-2-4). The receiver stands vertically on the rock surface under its own weight, and a stiff silicone grease is used as a coupling agent.

A typical experimental set-up is depicted in the photograph shown in Figure II-2-5. A SH source and receiver are located on the surface of the granite slab in this figure. The PAR 113 amplifier is to the right of the receiver, and the Velonix pulse generator is in the far left-hand side of the picture. The recording, processing and analysis of the laboratory P and SH reflection data will be outlined in the following sections of this chapter.

Figure Captions

Figure II-2-1
Schematic of the equipment used in the laboratory study. The lower box outlined by dashed lines is the original analog equipment. This was later replaced by the more versatile digital recording and processing system shown in the upper box.

Figure II-2-2
Two common polarization directions of commercially available piezoelectric plates. Application of a step-voltage across the largest faces causes the plates to be deformed as shown by the dashed lines.
a) P type polarization
b) S type polarization

Figure II-2-3
Piezoelectric plates used in the laboratory experiments as P or SH source transducers. Plates are attached to the polished granite surface using a 24 hour setting epoxy.
a) P wave source (polarization normal to rock surface)
b) SH wave source (polarization as shown)

Figure II-2-4
P and SH receivers used in the laboratory experiments. Receivers are shown with and without aluminum foil ground shields.
a) P wave receiver (polarization parallel to axis of backing rod)
b) SH wave receiver (polarization direction as shown)

Figure II-2-5
Typical experimental set-up showing a SH source connected to the Velonix pulse generator at left, and a SH receiver connected to the PAR 113 amplifier.

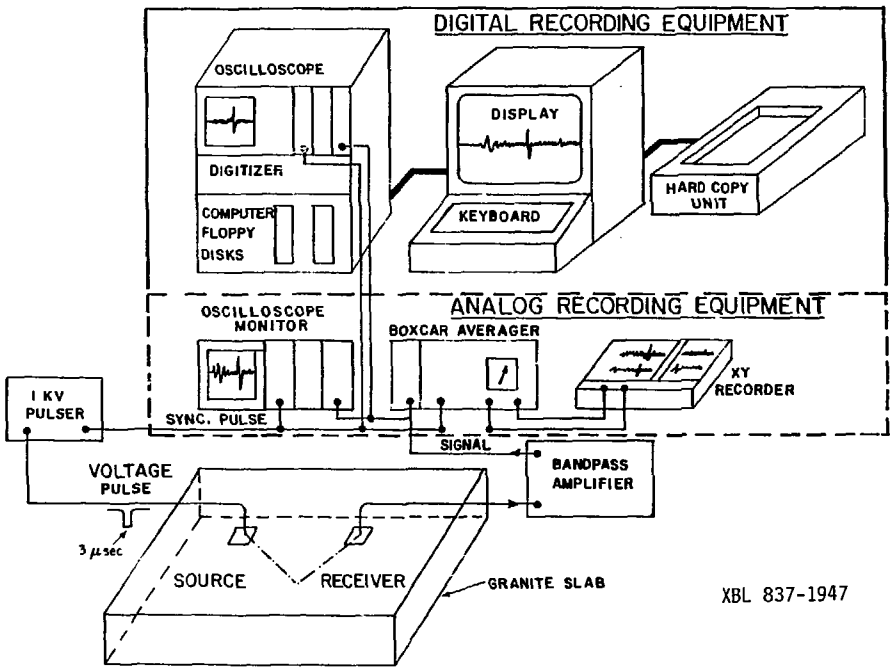
DIGITAL RECORDING EQUIPMENT
OSCILLOSCOPE
DIGITIZER
COMPUTER FLOPPY DISKS
DISPLAY
KEYBOARD
HARD COPY UNIT
ANALOG RECORDING EQUIPMENT
OSCILLOSCOPE MONITOR
BOXCAR AVERAGER
XY RECORDER
I KV PULSER
SYNC. PULSE
SIGNAL
BANDPASS AMPLIFIER
VOLTAGE PULSE
3 μsec
SOURCE
RECEIVER
GRANITE SLAB
XBL 837-1947

Figure II-2-1

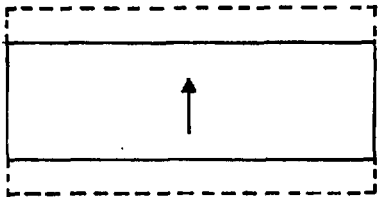

P Type

Figure II-2-2a

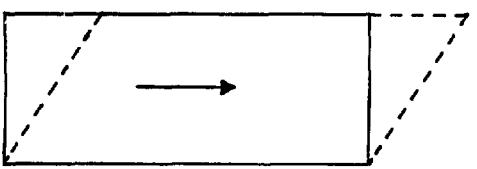

S Type

Figure II-2-2b

XBL 837-1948

XBB 837-6612

Figure II-2-3a

XBB 837-6611

Figure II-2-3b

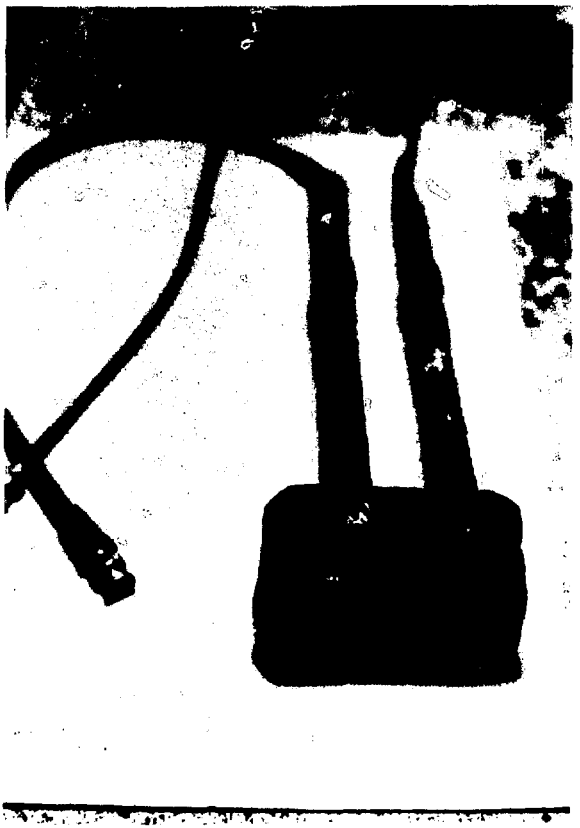

XBB 837-6609

Figure II-2-4a

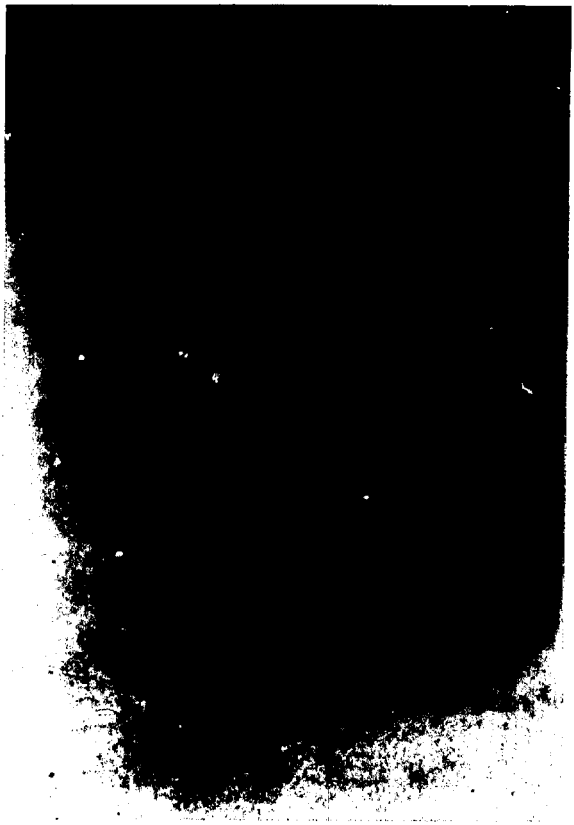

XBB 837-6610

Figure II-2-4b

Figure II-2-5

CHAPTER II

Section 3

Initial SH Experiments

The initial series of SH reflection experiments performed in the laboratory will be discussed in this section. The method of recording and displaying the SH reflection data is described, and a simple X^2-T^2 velocity analysis was performed in the analysis of the reflection event. The results of a simple experiment verify that the event interpreted as the SH reflection was indeed reflected from the far face of the granite slab. Modern data processing techniques were applied to the SH reflection data using the digital recording equipment. Deconvolution and directive array synthesis were found to be effective techniques when used to maximize the visual standout of the SH reflection event. The SH system which evolved was tested on two laboratory models, a planar free boundary and an irregular, air-filled fracture, with positive results.

The granite slab depicted in Figure II-2-1 (Section 2) is a 0.91 m × 0.91 m × 0.30 m block obtained from a quarry located in Raymond, California. This rock is a medium grained (1-5 mm) muscovite-bearing quartz monzanite locally used for monument and building stone. This rock is quite homogeneous, with no visual lineation or foliation of the crystalline grains. Very little fracturing is apparent in outcrops of this rock, which is a necessary requirement in the application of modern quarrying techniques.

In the laboratory experiments the SH source was a S type piezoelectric plate with dimensions 38 mm × 28 mm × 9.6 mm. It was found that this source would launch a transient SH pulse with a frequency band of roughly 5-160 kHz into the rock. The wavelengths in the granite slab would be, accordingly, 0.52-0.01625 m for a shear wave velocity β = 2600 m/s. The laboratory SH receiver was constructed as described in the previous section using a S type piezoelectric plate with dimensions 6.4 mm × 6.4 mm × 1.6 mm, and are shown in Figure II-2-4b (Section 2). The small size and thickness of this plate presumably gives the receiver a reasonably flat amplitude response with little phase shift within the frequency band of 5-160 kHz.

The SH reflection data referred to in these experiments is recorded along a traverse line that is orthogonal to the direction of polarization of the SH source (see Figure II-3-1). According to the results of Cherry, 1962, this is the azimuth of maximum far-field body SH wave radiation and minimum P-SV body wave radiation. Indeed this method of recording is standard practice in most land-based SH wave reflection experiments (Waters, 1982).

The reflection data are displayed as a series of time traces in which the receiver is sequentially moved away from the fixed source by equal distance increments. This is termed the common source gather in petroleum reflection seismology. An example of such a display, recorded on the largest face of the 0.91 m × 0.91 m × 0.30 m granite slab, is shown in Figure II-3-2. In this display the SH receiver is moved by 1 cm increments along a source-receiver separation that ranged from 7 cm to 50 cm, as measured from the center of the source to the

center of the receiver. The position of this traverse is shown in plan view in Figure II-3-3.

The earliest event observed in the SH data of Figure II-3-2, occurring from 25 μs to 150 μs, is a body SH wave that travels directly from source to receiver. This event will have a constant moveout (difference of arrival times for two adjacent receiver locations) because of the fact that the receivers are moved in constant increments parallel to the direction of propagation of this event. Thus, the shear wave velocity of the rock can be easily estimated from the phase velocity of the direct SH event shown in Figure II-3-2.

The horizontal phase velocity c for a plane shear wave in a homogeneous medium is defined as:

$$c = \beta/\sin\theta \qquad \text{[II.3.1]},$$

where θ is the angle between the wave normal and vertical. Then a direct SH wave propagating horizontally ($\theta=90°$) will have a phase velocity $c_{90°} = \beta$. If there is negligible dispersion of the direct SH pulse, then a common point on the transient waveform may be chosen as a phase reference. For example, the lowest point of the intial trough of the direct SH wavelets shown in Figure II-3-2 may be chosen as such a phase reference. If the arrival times of this reference point for each seismic trace are plotted against the source-receiver separation for that particular trace, then a linear relation (constant moveout) should exist, within the assumption of plane wave propagation in a homogeneous, non-dispersive elastic medium. The inverse slope of this

X-T plot (arrival time as a function of offset distance) will then give the phase velocity. For a direct SH event (θ=90°), the shear wave velocity β is just equal to the phase velocity of this event.

In actual practice, the arrival times obtained by picking a common reference point will have some non-zero error associated with the measurement. These errors result from inaccuracy in the position and orientation of the receiver, digitization error, and equipmental noise. The cumulative effect of these errors is not large in these laboratory studies, but some statistical method is required in the determination of the shear wave velocity from the inverse slope of the X-T plot. This linear relationship is established using the minimization of the sum of the squares of the deviations between the observed and estimated data values. The degree of uncertainty in the estimation of the velocity and zero-offset constant resulting from the least-squares fit can be evaluated using methods described in Bevington, 1969.

Let a variable y depend linearly on another variable x, i.e., $y = a_0 + b_0x$. Consider an experiment where N number of measurements of y_i (i=1,2,...,N) are made at corresponding values of x_i. In a realistic situation, experimental uncertainties will be introduced into the measurements of x_i and y_i so that the relation $y_i = a_0 + b_0x_i$ will not be exact. However, since x_i and y_i are somehow linearly related, this experimental relationship may be expressed as:

$$y_i = a + bx_i \qquad \text{[II.3.2]}$$

where experimental values a and b are used to estimate the corresponding

parent coefficients a_0 and b_0. Using the method of least-squares, in which the sum of the squares of the deviations $\Delta_i^2 = [y_i - a - bx_i]^2$ are minimized, the coefficients a and b are estimated from the data (x_i, y_i) using the expressions:

$$a = \frac{\Sigma x_i^2 \Sigma y_i - \Sigma x_i \Sigma x_i y_i}{N \Sigma x_i^2 - (\Sigma x_i)^2} \qquad \text{[II.3.3]}$$

$$b = \frac{N \Sigma x_i y_i - x_i \Sigma y_i}{N \Sigma x_i^2 - (\Sigma x_i)^2} \qquad \text{[II.3.4]}$$

It has been assumed in this analysis that the standard deviations σ_i for each of the data points y_i are equal ($\sigma_i = \sigma$). If it can also be assumed that the uncertainties in the experiment arise from instrumental error, and that most of this error occurs in the measurement of the dependent quantity y_i, then the standard deviation σ can be approximated by the sample variance s defined as:

$$\sigma^2 \approx s^2 = \frac{1}{(N-2)} \sum (y_i - a - bx_i)^2 \qquad \text{[II.3.5]}$$

The standard deviation σ_z of the determination of any parameter z is given by:

$$\sigma_z^2 = \sigma^2 \sum \left[\frac{\partial z}{\partial y_i}\right]^2 \qquad \text{[II.3.6]}$$

Using this equation, the standard deviations (σ_a and σ_b) of the zero-offset coefficient a and slope b are determined by:

$$\sigma_a^2 = \frac{\sigma^2 \Sigma x_i^2}{N\Sigma x_i^2 - (\Sigma x_i)^2} \approx \frac{s^2 \Sigma x_i^2}{N\Sigma x_i^2 - (\Sigma x_i)^2} \qquad \text{[II.3.7]}$$

$$\sigma_b^2 = \frac{N\sigma^2}{N\Sigma x_i^2 - (\Sigma x_i)^2} \approx \frac{Ns^2}{N\Sigma x_i^2 - (\Sigma x_i)^2} \qquad \text{[II.3.8]}$$

This best-fit analysis was applied to the arrival time data obtained from the direct SH event shown in Figure II-3-2, in which the minimum value (largest negative trough) is used as a reference point in picking the arrival times. Since the direct event has an angle of incidence of $\theta = 90°$, then the best-fit slope of the X-T plot gives an estimated shear wave velocity of $\beta = 2545$ m/s ± 10 m/s. The zero-offset constant determined in this analysis is a = 2.69 μs ± 0.36 μs.

The constant a calculated using Equation II.3.3 represents the arrival time of the direct SH body wave at zero source-receiver offset (coincident source and receiver). It is sensible to argue that the direct wave should arrive at time zero when the source and receiver occupy the same point in space. The positive value for the constant a then represents some average time delay between the arrival time reference point (the first negative trough) and the initial arrival of body SH energy. Since the least-squares analysis places no limits on the sign of the zero-offsent constant, negative values can occur when the direct SH data set is noisy.

The large event occurring in the time window from 225-325 μs is a SH body wave reflected from the opposite large face of the granite slab. To assure that event is indeed the primary SH reflection, a simple experiment was performed in an attempt to demonstrate that the raypath of this event reflects from the opposite face.

In this experiment a lead block was pressed against the lower surface of the granite slab at the point of reflection mid-way between source and receiver. A hydraulic jack was used to vary the upward force against the lead block (see Figure II-3-4). The supposition of this experiment was that some energy in the incident SH wavelet would be transmitted into the lead block, thereby decreasing the amplitude of the reflected wavelet.

The SH source-receiver pair was fixed during this experiment, and all equipment settings were unchanged as the force on the lead block was increased. A number of SH traces recorded during such a loading cycle are shown in Figure II-3-5. The large amplitude event occurring between 240-280 μs was thought to be the SH reflection from the far face, as it arrived at very nearly the time predicted using the known thickness and shear wave velocity of the granite slab. As can be seen in this figure, the amplitude of the reflected SH wavelet decreased as the force on the lead block was increased. However, other events with raypaths unaffected by the presence of the lead block (e.g. the direct SH event occurring between 80-100 μs) remained constant in amplitude as the force was increased. An effective reflection coefficient was obtained by dividing the amplitude of the reflected wavelet (measured from peak to following torugh) at a given force by the reflected amplitude when the lead block was removed.

Repeated experiments of this sort have demonstrated that the response shown in Figure II-3-6 is representative. The reflection coefficient decreases linearly as the load is applied, until a stress of approximately 225 psi is reached (stress = force/area of the lead

block). The reflection coefficient then remains relatively constant as the stress is further increased. The initial linear decrease of the reflection coefficient is thought to result from the effective increase in contact area as the lead block is deformed to fit into the micro-irregularities of the granite surface. When most of these irregularities have been filled, further increased loading will not produce any change in the contact area, and consequently the reflection coefficient will remain constant. The results of these experiments verify that the large amplitude event occurring between 225-325 μs is indeed a SH wavelet reflected from the opposite face of the granite slab, and that gross changes in the nature of the reflecting interface can produce observable variation in the amplitude of the reflected wavelet.

A second estimate of the shear wave velocity of the granite slab can be made from a standard X^2-T^2 plot of the SH reflection arrival times, if the reflecting interface is horizontal and the propagation velocity is constant. The geometry of this situation is shown in Figure II-3-7, and in summary, the reflection arrival time is determined by the relation:

$$[T(X)]^2 = X^2/V^2 + 4d^2/V^2 \qquad \text{[II.3.9]}$$

where, $T(X)$ = reflection arrival time at offset distance

X = source-receiver offset distance

d = depth to the horizontal reflector

V = constant propagation velocity of the medium.

Thus, if the square of the reflection arrival times (T^2) is graphed

as a function of the square of the offset distance (X^2), then a linear relation between T^2 and X^2 becomes apparent. The square-root of the inverse slope of this line is commonly termed the moveout velocity, and the remaining constant $\frac{4d^2}{V^2}$ is the squared reflection arrival time at zero source-receiver offset. For a constant velocity medium, the moveout and propagation velocities are exactly equal if the reflector is horizontal.

Again the actual measurement of reflection arrival time data will require statistical methods to be used in the data analysis. The best-fit slope of the X^2-T^2 plot will be determined using the least-squares algorithm discussed previously. The moveout velocity (inverse square root of the X^2-T^2 slope) is used to estimate the propagation velocity assuming a constant velocity medium. This method of data analysis can be applied to either P or SH reflection arrival time data. The remaining zero-offset constant can be used with this moveout velocity to calculate the depth to the horizontal reflector.

The SH reflection arrival times are picked from the record section shown in Figure II-3-2 using the bottom of the initial trough of the wavelet as a reference point. An X^2-T^2 plot of these data is made, and the best-fit slope, zero-offset constant and their associated standard deviations are calculated. From the slope of X^2-T^2 curve, the shear wave velocity is estimated as β = 2610 m/s ± 15 m/s, and the zero-offset arrival time is 231.2 μs ± 9.3 μs. Using the velocity and zero-offset values, the calculated depth to the reflector is 30.2 cm ± 1.2 cm, which compares favorably with the actual measured depth of 29.8 cm ± 0.2 cm. This estimate of the shear wave velocity (β =

2610 m/s) is slightly (but significantly) higher than the estimate obtained using the direct SH data (β = 2525 m/s). This means that the S velocity distribution is not homogeneous, and that the value of the moveout velocity then represents some sort of spatially weighted average of the true S wave velocity structure through the granite slab. However, since the difference in the two shear velocity measurements is only 4%, the effects due to the inhomogeneous velocity structure will be small.

Two different data processing techniques commonly employed in petroleum exploration seismology are applied to the laboratory SH data. The purpose of these additional procedures is to increase the detectability of reflected SH body wave energy in the seismic record section. One method used is the deterministic deconvolution of the source wavelet from the reflection data, and the other is the synthesis of a beamforming array from the individual seismic traces.

Deconvolution, in general, is a process which undoes the action of a previous convolution, or filter. A simple model of the earth considers the received waveform r(t) to result from the convolution of the seismic source input s(t) and the impulse response of the earth i(t), i.e.,

$$r(t) = s(t) \otimes i(t) \qquad \text{[II.3.10]}$$

In the Fourier transform domain, this convolution may be rewritten as the product:

$$\tilde{R}(\omega) = \tilde{S}(\omega)\tilde{I}(\omega) \qquad \text{[II.3.11]}$$

where $\tilde{R}(\omega)$, $\tilde{S}(\omega)$ and $\tilde{I}(\omega)$ are the Fourier transforms of r(t), s(t) and i(t) respectively. Then, $\tilde{I}(\omega) = \tilde{R}(\omega)/\tilde{S}(\omega)$, and the response of the earth i(t) can be recovered using the inverse Fourier transform on $\tilde{I}(\omega)$. The result of deconvolution processing is that each event on the seismogram is replaced by a symmetrical, condensed signal whose central peak (maximum value) occurs at the arrival time of the event. In the case of these laboratory experiments the deconvolution process differs from that used in exploration seismology because the outgoing source pulse s(t) can actually be measured.

In the laboratory experiments it is possible to obtain an estimate of the source wavelet by placing the receiver directly below the source on the opposite side of the granite slab. Figure II-3-8a shows the measured source wavelet truncated in time due to the fact that energy received at later times will have travelled along paths other than the direct one. The pulse is also shifted to start at time t=0 in order to eliminate time shifts that would occur during deconvolution.

With the facilities afforded by the digital recording system, the amplitude spectrum of the measured source pulse can be readily obtained and plotted. The amplitude spectrum corresponding to the wavelet shown in Figure II-3-8a is given in Figure II-3-8b. The received waveform is shown in Figure II-3-9a and the corresponding amplitude spectrum is shown in Figure II-3-9b. Spectral division is performed with the complex values (amplitude and phase spectra) of the spectral components over a frequency band where the signal/noise ratio is high. Figures

II-3-8b and II-3-9b show that this band must be from 10 kHz to 160 kHz. The final deconvolved version of the received waveform is retrieved from the complex quotient (Figure II-3-10a is the amplitude spectrum) by an inverse Fourier transform, and the resulting deconvolved trace is shown in Figure II-3-10b. Since the source output pulse starts at zero time, the peak of the symmetrical pulse representing the primary SH reflection occurs at exactly the same time (233 μs) as the much less distinguishable onset of the unprocessed SH reflection event.

The deconvolution processing is applied to each of the individual traces in Figure II-3-2, with the resulting record section shown in Figure II-3-11. Note the ease of picking the arrival times of the deconvolved reflection events, especially for the closer offset data. The maximum of the deconvolved wavelet is used as the arrival time reference since this value should correspond to the onset arrival time of the reflection event. An X^2-T^2 analysis of this data gives a shear wave velocity β = 2585 m/s ± 15 m/s and a zero-offset arrival time of 226.2 μs ± 10.0 μs. The calculated depth to the reflector is 29.2 cm ± 1.3 cm, which is statistically comparable to the actual depth of 29.8 cm ± 0.2 cm. The shear wave velocity estimated from the deconvolved reflection event is also in agreement with the value derived from the unprocessed SH reflection data (2610 m/s ± 15 m/s).

A multiplicity of seismic traces, such as those shown in Figure II-3-2, may be weighted and summed in order to create a directional sensitivity, i.e., a seismic atenna. The directional properties of a simple receiver antenna will be illustrated in the following analysis.

Consider N discrete omnidirectional point receivers situated with constant offset ℓ along the surface of a half-space with constant acoustic velocity V. A plane acoustic wave of frequency ω and unity amplitude propagates upward with an angle θ from the vertical, and is measured at each receiver point as a function of time t. The signals of all receivers are then summed with equal (unity) weighting to give the array response $\psi(\omega,\theta)$, i.e.,

$$\psi(\omega,\theta) = 1/N \left[e^{i\omega t} + \left[e^{i\omega(t + \frac{\ell \sin\theta}{V})} \right] + \ldots + \left[e^{i\omega(t + \frac{N\ell \sin\theta}{V})} \right] \right] \quad \text{[II.3.12]}$$

This response function is complex valued, so that the results of the array response are usually expressed in terms of amplitude and phase spectra (Officer, 1958). The array amplitude spectral response can be written (for temporal frequency $f = \omega/2\pi$):

$$|\psi(f,\theta)|^2 = \left[\sin(\frac{N\pi f \ell \sin\theta}{V}) / N\sin(\frac{\pi f \ell \sin\theta}{V}) \right]^2 \quad \text{[II.3.13]}$$

and the phase spectral response is:

$$\phi(f,\theta) = \tan^{-1}\left[\frac{N\pi f \ell \sin\theta}{V} \right] \quad \text{[II.3.14]}$$

These two equations are commonly used to estimate the array response as a function of angle of incidence θ for fixed values of receiver number N and spacing ℓ, frequency f, and half-space velocity V. For the SH laboratory data set a six element (N=6) array with spacing ℓ = 1 cm, velocity V = 2550 m/s and frequencies f = 20, 70 and 120 kHz

is studied. These last values are chosen in order to sample the lower, middle, and upper limits of the frequency band of the SH wavelet. The amplitude and phase spectra for this particular array are shown in Figures II-3-(12a and b), respectively.

The purpose of this trace summation technique is to increase the amplitude of seismic events with nearly vertical angles of incidence ($\theta \approx 0°$) with respect to horizontally propagating events ($\theta \approx 90°$). When this process is applied to the SH data of Figure II-3-2, the amplitude of the body SH reflection should be increased relative to the amplitude of the direct SH body wave. Figure II-3-12a shows that for a fixed frequency the amplitude response for waves with incidence angles of 15° or less is much larger than the response for waves with a horizontal propagation direction. This amplitude enhancement is much more pronounced at higher frequencies, and in this particular case very little enhancement occurs for waves with a frequency of 20 kHz or less. The phase response curves shown in Figure II-3-12b indicate that rather large phase shifts are introduced even at low incidence angles by this simple summation procedure.

The SH receiver data presented in Figure II-3-2 are summed in unweighted groups of six successive traces to yield a single array waveform. The source-receiver offset for this summed trace is defined as the distance from the center of the source to the center of the receiver distribution used in the array synthesis. Thus, the 44 individual traces in Figure II-3-2 (offsets from 7 cm to 50 cm) are summed to give 39 composite traces with offsets from 9.5 cm to 47.5 cm, which are shown in Figure II-3-13. Comparison of these two figures shows unques-

tionable SH reflection amplitude enhancement (relative to the direct event) resulting from the discrete array synthesis. Note also that some amplitude enhancement occurs in the time interval from 400-500 μs, although the exact nature of these events is unclear. For offsets of 20 cm or less the single event in this time window is believed to be the first multiple SH reflection from the far face of the slab. At larger offset distances a number of different events arrive in this time window, and the resulting interference pattern masks the arrival of each discrete event. Some of these events are thought to be seismic energy scattered from the edges of the slab which then sideswipes across the receiver line. The arrival of these scattered seismic events places a limit on the use of a one-dimensional model in analysis of the data obtained from a finite size laboratory model. In the case of a 0.91 m × 0.91 m × 0.30 m granite slab, only the first 450-500 μs of each trace can be successfully interpreted using the previously described one-dimensional methods of analysis.

Deconvolution and directive array synthesis may be applied in cascade in order to increase the detection capability of these ultrasonic reflection methods. The deconvolved SH data presented in Figure II-3-11 are summed as before to synthesize the response of an unweighted 5 cm array, and the results of this operation are shown in Figure II-3-14. Comparison of this figure and Figure II-3-2 shows that the application of both deconvolution and directive array processing further enhances the visibility of the reflection event when compared to data processed using only deconvolution or array synthesis techniques.

Figure II-3-15 is a photograph of a large fractured granite cylinder used in the initial laboratory phase of this research, and Figure II-3-16 is a diagram of the top of the cylinder showing the location of several experimental traverses. The experiments here were designed to simulate work with naturally occurring fractures which are irregular and dipping with respect to the observation surface. A tensile fracture (see Figure II-3-15) was induced in the 2.0 m (long) × 1.0 m (diameter) cylinder at a depth of approximately 0.5 m below the plane surface depicted in Figure II-3-16. The axial hole from the surface to the fracture was not relevant to these reflection experiments. When the upper and lower halves of the cylinder were placed together, a fracture was created that was relatively thin (approximately 1 mm). A very thorough description of this granite model (including more photographs) is given in Witherspoon, Amick, and Gale, 1977.

This fracture was air-filled in all of the cases reported in the following discussion, all data obtained from this fracture model were recorded using the analog acquisition system. In order to utilize the full operating range of the boxcar integrator the amplifier gain was continually adjusted so that the amplitude of the direct SH event remained relatively constant from trace to trace.

Figure II-3-17 shows the offset SH data obtained along profile line L1L on August 15, 1978. Numerous seismic events are visible on this record, but only three of these events are easily identified. Event A in this figure is the first detectable seismic energy on the record, and probably represents some sort of "parasitic" P wave created by the SH source that travels directly to the receiver. The large

amplitude event B is undoubtedly the direct SH event. Event C of this figure is thought to be the SH reflection from the air-filled fracture because of its arrival time and hyperbolic moveout. The numerous, large amplitude events visible in the time window 100-300 μs are believed to result from seismic energy diffracted by the axial hole located at the center of the circular face. Ray-path tracing indicates that such diffraction events should indeed arrive in this time window.

Figure II-3-18 presents a repeatability check obtained on August 25, 1978 of the SH data recorded along profile line L1L. The comparison between this figure and Figure II-3-17 is good, and indicates that the errors inherent in repositioning the receiver are not overwhelming. Figure II-3-19 is a SH data set recorded along profile line L2R which demonstrates that it was possible to detect the SH reflection event along profile lines other than L1L.

In Figures II-3-17, 18, 19, the slopes of the straight lines A and B are used to estimate the P and S velocities ($\alpha = V_A$ and $\beta = V_B$). No statistical information regarding the fit of these slopes to the arrival time data is available using this crude method of analysis. For these data sets the P and S velocities lie in the range of α = 3.1-3.3 km/s and β = 2.2-2.4 km/s. For a horizontal reflector and constant velocity medium, the moveout velocity V_C should be the same as the direct SH velocity V_B. This relationship is valid within the errors expected in hand-fitting curves along profile line L2R, but there is significant disagreement between velocities V_B and V_C along profile L1L. Thus, either the fracture is dipping beneath L1L, or the S velocity beneath L1L is very (unreasonably) low.

For a dipping reflector, the moveout velocity derived from an X^2-T^2 plot of the reflection arrival times will not equal the propagation velocity of a constant velocity medium. The moveout velocity for L1L shows that the fracture (reflector) has a significant amount of dip beneath this profile line. By combining the reflection arrival time data from L1L (Figure II-3-18) and L1R (data not shown) to obtain a symmetrical spread, a derivation given by Telford et al., 1976, can be used to obtain the dip angle of the reflector (angle from the horizontal). In this analysis only data from source-receiver separations of 20 cm or less are used, so that the assumption of constant reflector dip would remain valid. Table II-3-1 tabulates the arrival time data used in the calculation, and the resulting calculated dip angle. These computed angles are very comparable to the observed dip of the fracture surface beneath the SH source common to L1L and L1R, the observed dips ranging from 3° to 6°. The equation used in calculating the dip angle from the arrival time data is:

$$\theta = \sin^{-1}[\beta(t_1-t_2)/2d] \qquad \text{[II.3.15]}$$

where, β = shear wave velocity = 2410 m/s

t_1 = arrival time of reflection event on down-dip receiver (L1L)

t_2 = arrival time of reflection event on up-dip receiver (L1R)

d = source-receiver separation

θ = angle of dip from horizontal.

It should be noted that the Poisson's ratio for this granite model (using the measured P and S velocities of Figure II-3-18) has a value

Table II-3-1

Tabulation of data used to calculate dip angle of the reflector

d (mm)	t_1 along L1L (μs)	t_2 along L1R (μs)	θ L1L down-dip from source (degrees)
100	413.0	406.2	4.7
120	414.5	407.0	4.3
140	417.5	408.1	4.6
160	420.5	407.7	5.5
180	422.0	410.0	4.6
200	425.4	413.4	4.1

Averaged measure dip is 4.6° with L1L down-dip from the source.

σ = 0.0064. This is an extremely low value, and is due to an uncommonly low P wave velocity. Previous experiments were performed on this granite cylinder in which it was subjected to numerous large axial loads (Witherspoon, Amick, and Gale, 1977), and it is possible that microfracturing of the granite during these tests is the cause of the anomalously low P wave velocity.

The initial SH experiments performed on the granite slab model were successful in detecting a discrete SH reflection from the opposite face of the slab. Shear wave velocities estimated from both the direct and reflected SH events indicate that the model has a fairly homogeneous S velocity structure, and that errors inherent in the experimental technique are not overwhelming. The signal processing techniques of deconvolution and directive array synthesis were found to significantly increase the amplitude of the reflected SH event in comparison to the direct SH amplitude. Experiments performed on a fractured granite model determined that an air-filled, irregular, dipping fracture could be easily detected using these ultrasonic SH reflection methods. The successes of these laboratory studies confirmed the practicality of the SH reflection method in fracture detection at this size scale. The results of this initial work are encouraging, and suggest that an investigation of P wave reflection methods should follow a similar course.

Figure Captions

Figure II-3-1
Photograph of laboratory SH source and receiver at 13 cm source-receiver offset. Polarization direction of SH source and receiver is orthogonal to the traverse line.

Figure II-3-2
Unprocessed SH traces recorded on the 0.91 m × 0.91 m × 0.30 m granite slab. Note the direct (25-150 μs) and reflected (230-270 μs) SH events.

Figure II-3-3
Plan view of the top face of the granite slab showing location of SH source and profile line. Position of P wave traverse discussed in the next section is also shown.

Figure II-3-4
Schematic of an early test in which a decrease of the SH reflection event is caused by pressing a lead plate onto the surface of the granite slab at the point of reflection.

Figure II-3-5
Variation in the amplitude of the reflection event as the force on the lead block is increased. Note that the amplitude of the direct SH and other events remain constant.

Figure II-3-6
Typical response of the SH reflection coefficient as a function of axial stress across the lead-granite boundary. It is assumed that total reflection (R_{SH}=1.0) occurs when the lead block is removed from the reflecting point.

Figure II-3-7
Geometry of a single horizontal reflector at a depth d beneath the surface in a constant velocity V medium. The reflection arrival time T(X) is a function of source-receiver offset X.

Figure II-3-8
a) Display of SH source pulse measured on the lower face of the granite slab. It has been shifted to start at zero time, and truncated to avoid arrivals from different travel paths.
b) Amplitude spectrum of SH source pulse.

Figure II-3-9
a) Received SH waveform. Note asymmetrical character of the reflection wavelet and the difficulty in measuring the arrival time (≅235 μs).
b) Amplitude spectrum of the received SH waveform.

Figure II-3-10
a) Result of dividing received spectra by source spectra (only amplitude spectrum shown).
b) Result of retransformation of the spectral quotient. Note the sharp peak now at the SH arrival time (233 μs).

Figure II-3-11
Deconvolved SH traces. Unprocessed data shown in Figure II-3-2.

Figure II-3-12
Plane wave response of a 6 element array 5 cm in length on a half-space with velocity V = 2550 m/s as a function of angle of incidence θ.
a) Amplitude response at frequencies of 20, 70, and 120 kHz
b) Phase response at frequencies of 20, 70 and 120 kHz

Figure II-3-13
Traces of Figure II-3-2 summed in unweighted groups of 6 to simulate a 5 cm array. Offset is from 9.5 cm to 47.5 cm using 1 cm increments.

Figure II-3-14
Traces of Figure II-3-11 summed in unweighted groups of 6 to simulate a 5 cm array. Offsets from 9.5-47.5 cm by 1 cm increments.

Figure II-3-15
Photograph of a large granite cylinder with an axial tensile fracture approximately 0.5 m from one face of the cylinder. From Witherspoon, Amick, and Gale, 1977.

Figure II-3-16
Diagram of SH traverses made on the upper face of the fractured granite cylinder shown in Figure II-3-15.

Figure II-3-17
SH reflection record obtained along profile L1L on August 15, 1978. Event A is a direct P wave, event B is a direct SH wave, and event C is a SH wave reflected from the fracture. The large amplitude events occurring between 120-300 μs are probably diffractions from the axial hole at the center of the circular face.

Figure II-3-18
SH profile recorded along line L1L on August 25, 1978 in order to check the repeatability of these techniques.

Figure II-3-19
SH reflection profile recorded along line L2R on August 15, 1978. Note the similarity of this and profiles recorded along L1L.

XBB 837-6607

Figure II-3-1

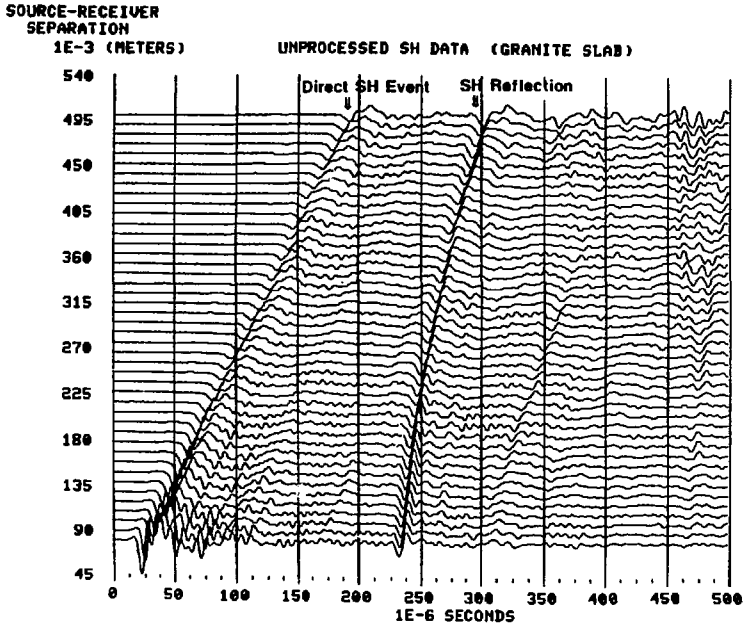

XBL 837-1949

Figure II-3-2

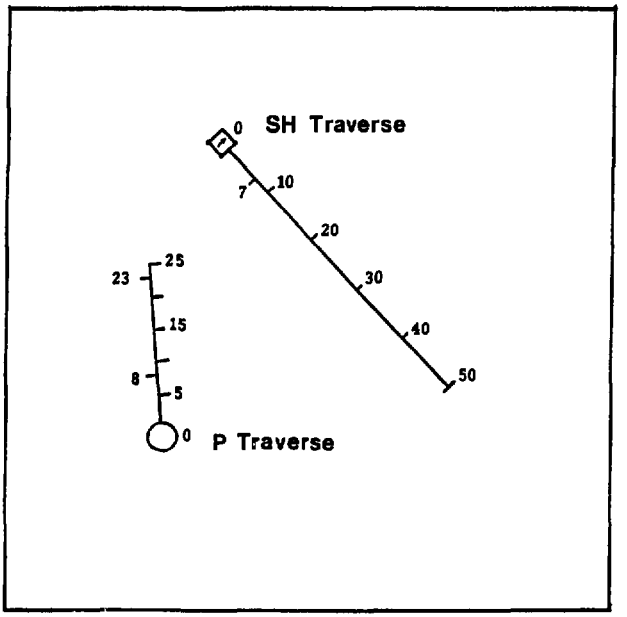

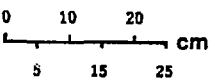

XBL 837-1950

Figure II-3-3

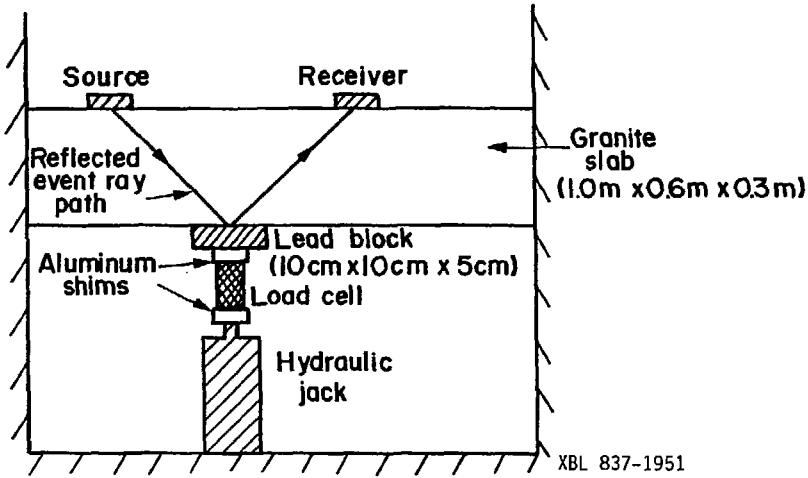
Source
Receiver
Reflected event ray path
Granite slab (1.0m x0.6m x0.3m)
Lead block (10cm x10cm x 5cm)
Aluminum shims
Load cell
Hydraulic jack
XBL 837-1951

Figure II-3-4

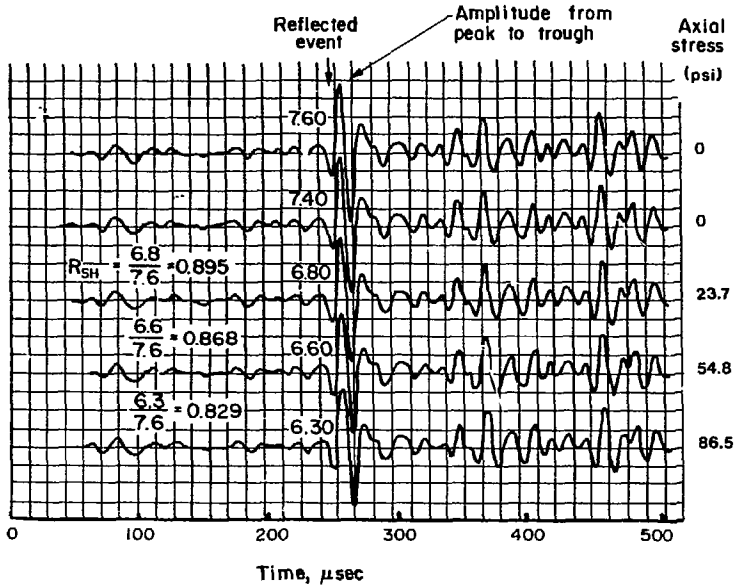

XBL 837-1952

Figure II-3-5

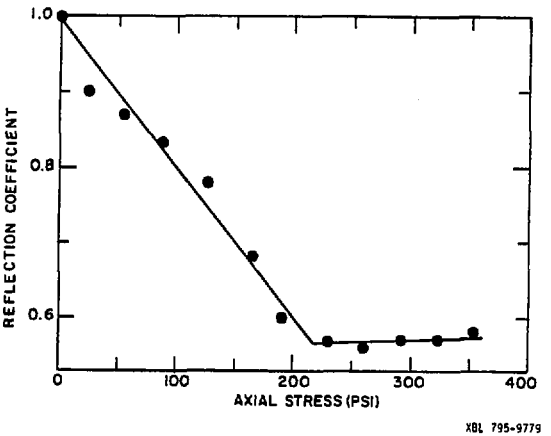
1.0
0.8
0.6
REFLECTION COEFFICIENT
0
100
200
300
400
AXIAL STRESS (PSI)
XBL 795-9779

Figure II-3-6

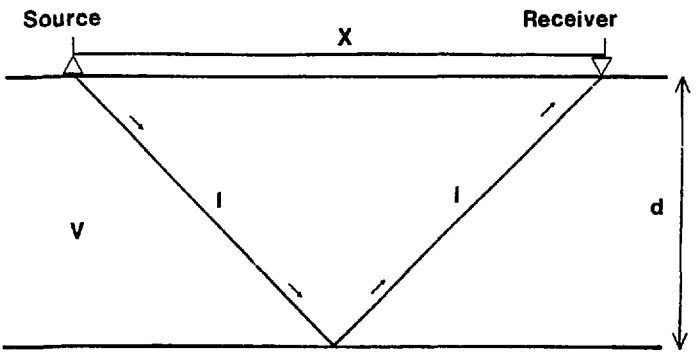

$$T[X] = {}^{2l}/_{V}$$

$$l^2 = {}^{X^2}/_{4} + d^2$$

$$\Rightarrow T[X]^2 = {}^{X^2}/_{V^2} + {}^{4d^2}/_{V^2}$$

XBL 837-1953

Figure II-3-7

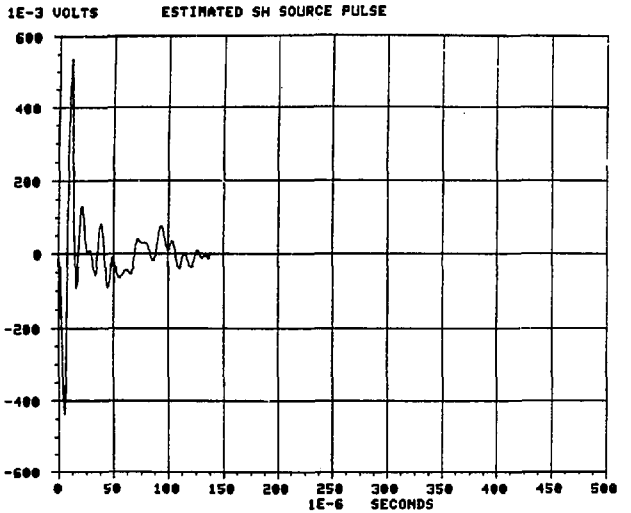

Figure II-3-8a

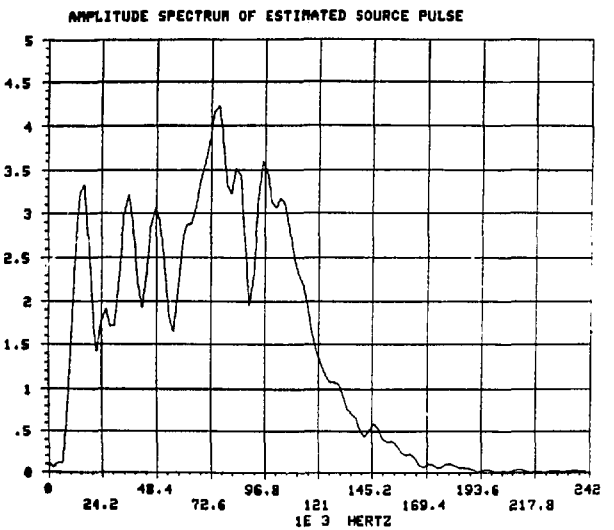

Figure II-3-8b

XBL 837-1954

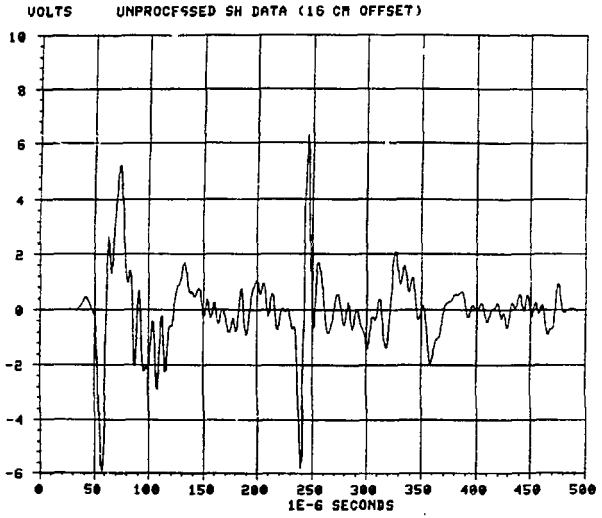

Figure II-3-9a

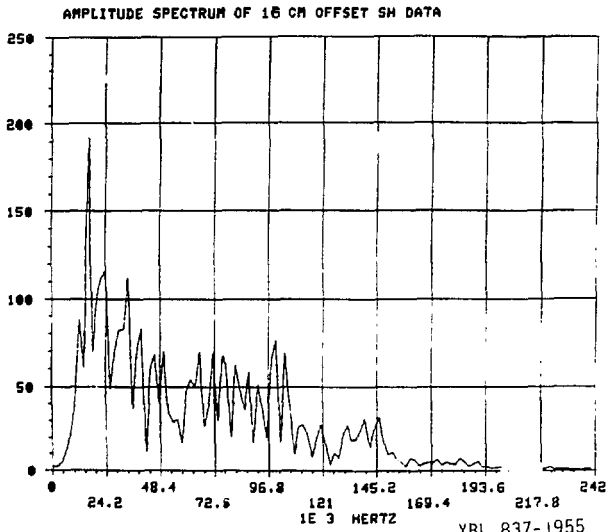

XBL 837-1955

Figure II-3-9b

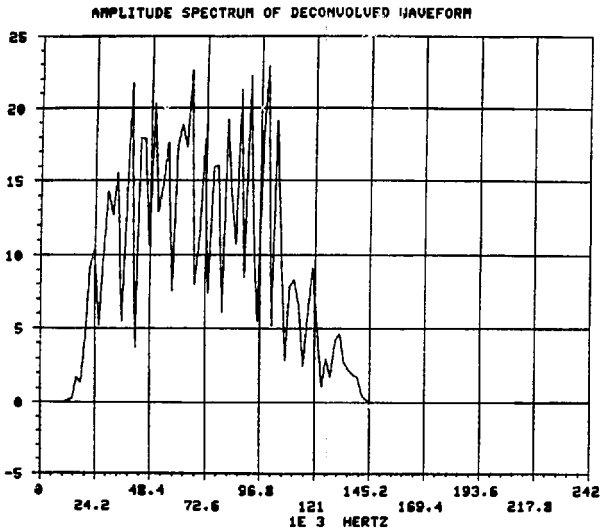

Figure II-3-10a

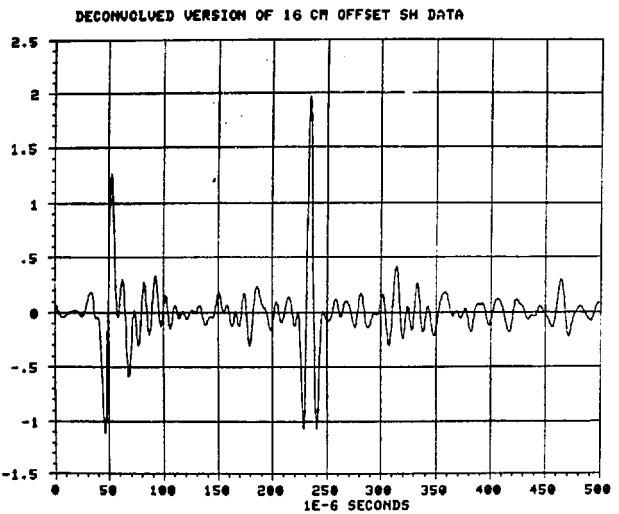

Figure II-3-10b

XBL 837-1956

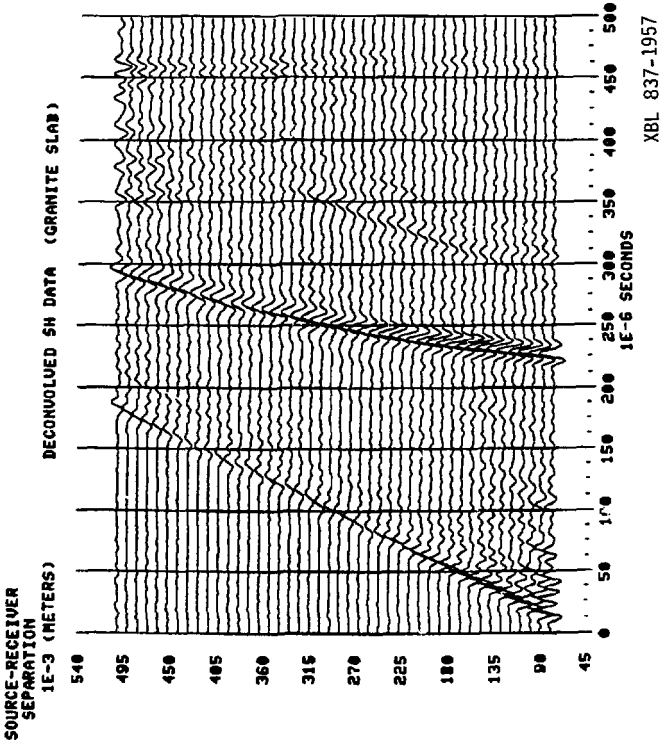

Figure II-3-11

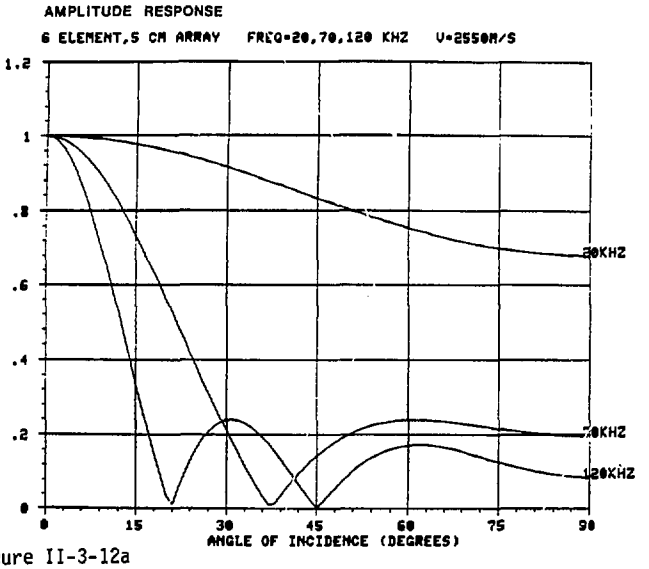

Figure II-3-12a

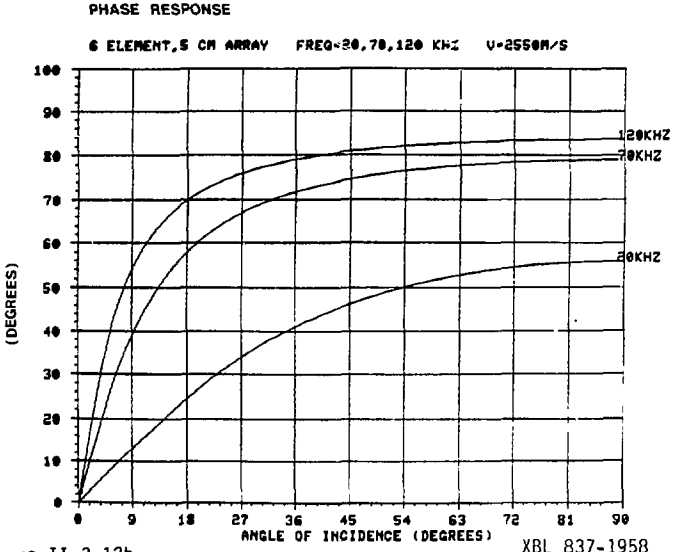

Figure II-3-12b

XBL 837-1958

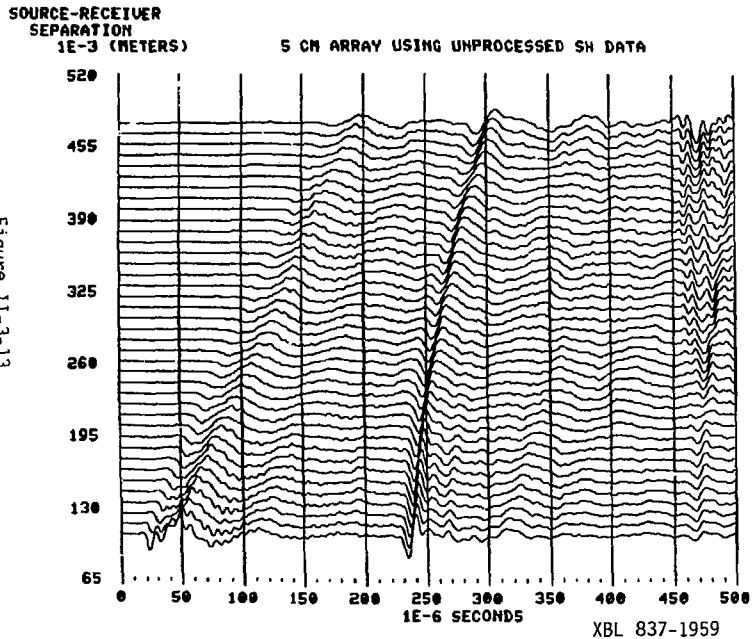

Figure II-3-13

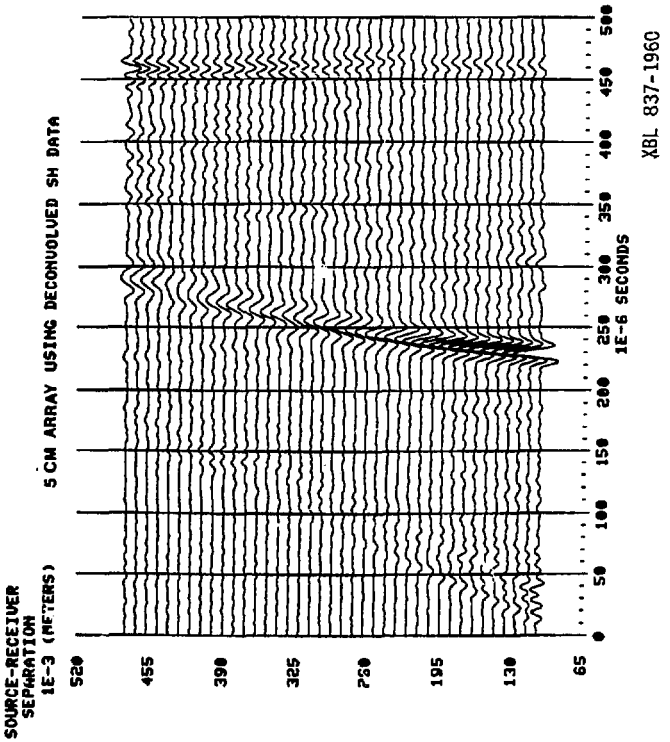

Figure II-3-14

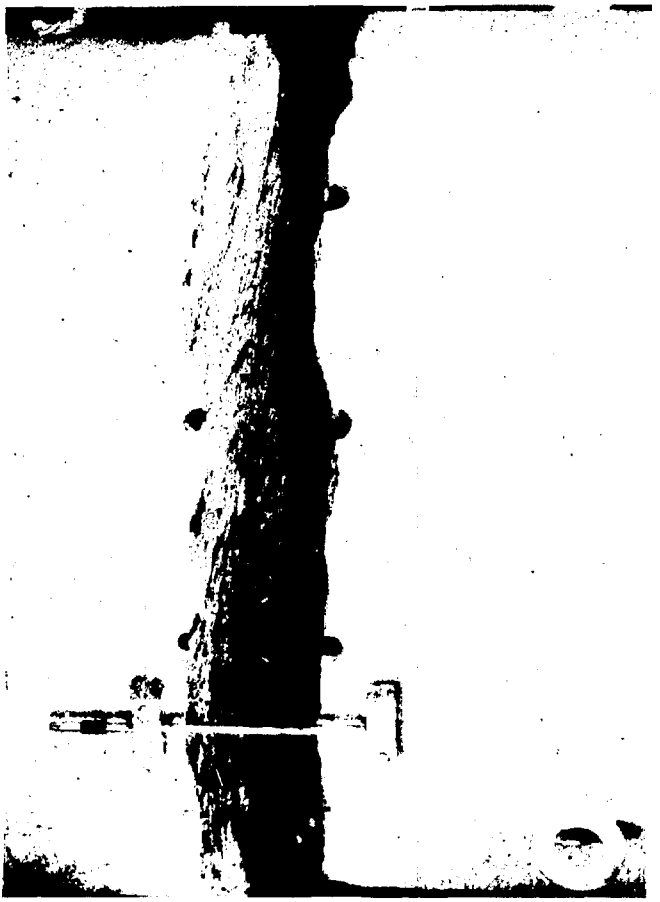

XBB 837-6603

Figure II-3-15

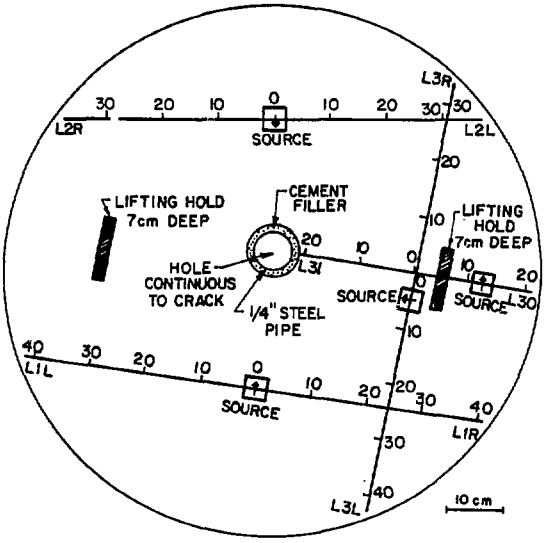

XBL 795-9780

Figure II-3-16

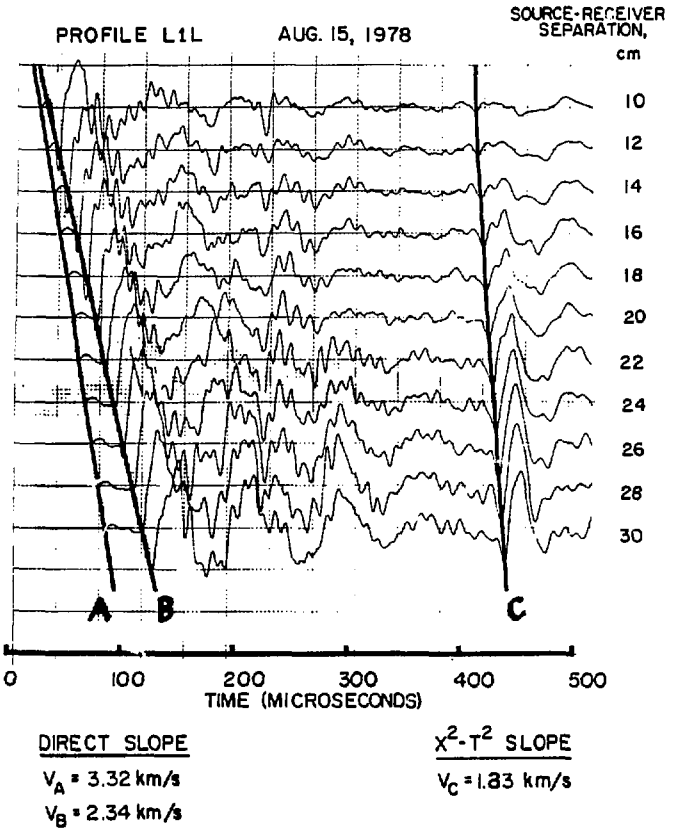

Figure II-3-17

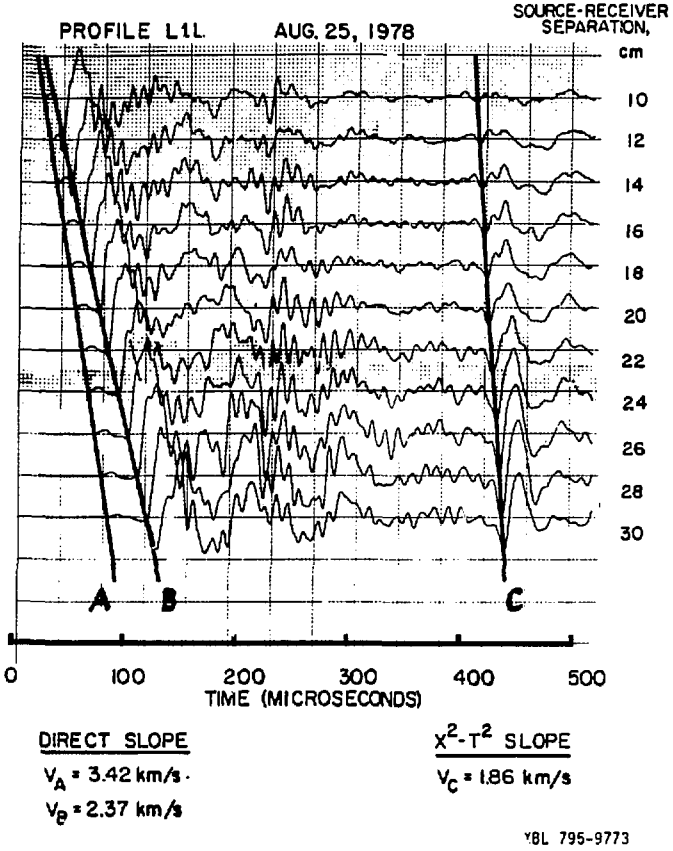

Figure II-3-13

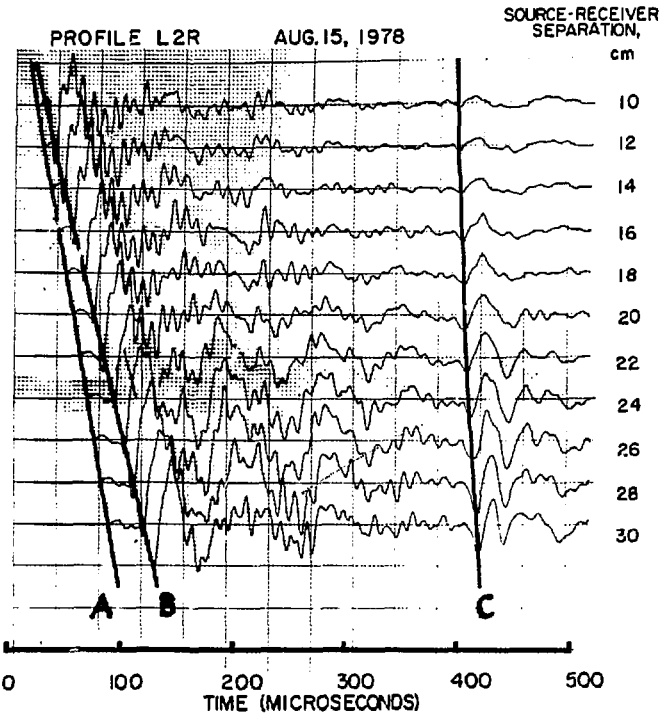

DIRECT SLOPE

$V_A = 3.13$ km/s

$V_B = 2.27$ km/s

X^2-T^2 SLOPE

$V_C = 2.16$ km/s

XBL 795-9772

Figure II-3-19

CHAPTER II

Section 4

Initial P Experiments

The initial series of P wave reflection experiments performed in the laboratory will be discussed in this section. Because of the similarity in the processing techniques applied to both the P and SH laboratory data, much of the background discussion regarding these techniques has already been presented in the previous section. For reasons to be elaborated, the application of directive array synthesis and deterministic deconvolution is necessary in order to produce interpretable P wave reflection data in the laboratory setting. Thus, useful P wave reflection data were obtained only after incorporation of digital recording into the experimental system.

The far-field radiation pattern of a circular disk of finite radius vibrating normally to the surface of an isotropic, homogeneous elastic half-space is given in Miller and Pursey, 1954. The elastic wavefield radiated from such a source is complicated, and consists of both P and SV body waves and Rayleigh waves travelling away from the source. The largest fraction of the input source energy travels as a Rayleigh wave (approximately 68%). SV body waves take up about 26% of the impressed source energy, leaving only 6% of the total energy to radiate into the half-space as body P waves (Miller and Pursey, 1956). Thus the piezoelectric disks used as P wave sources in these experiments are very inefficient radiators of body P wave energy. Also, while Rayleigh

waves diminish in amplitude as $R^{-1/2}$, where R is the distance from the source, the compressional (P) body waves diminish as R^{-1}. In these experiments P wave reflections travel at least twice as far as direct Rayleigh waves, so for a given receiver offset the P reflections will be proportionally reduced in amplitude compared with the direct Rayleigh wave.

A circular P type disk of piezoelectric material has two predominant modes of oscillation, the thickness mode and the radial mode (Mason, 1948). An additional complication for P type circular disks arises because the radial and thickness modes are coupled through Poisson's ratio. The interaction of these oscillatory modes causes the radiated elastic pulse to be long and complicated. This "ringing" source detracts from the resolution of individual events on the unprocessed P wave record section.

In the laboratory experiments, the P wave source was a P type circular piezoelectric plate 50 mm in diameter and 3.2 mm thick. It was found that this source would launch a transient elastic pulse (P, SV, and Rayleigh wave) with a frequency band of 20-350 kHz into the granite slab. This would correspond to wavelengths of 0.23-0.0131 m for a P wave velocity of α = 4600 m/s. The laboratory P receiver was constructed using a P type disc 6.4 mm in dimater and 1.6 mm thick, and is shown in Figure II-2-4a. It was presumed that this receiver had a relatively flat response over the frequency band 20-350 kHz.

A P wave traverse was made on the 0.91 m × 0.91 m × 0.30 m granite slab as shown in Figure II-3-3 (previous section). The unprocessed data are shown in Figure II-4-1, with the receiver moved in 0.5 cm

increments over a source-receiver offset of 8 cm to 23 cm. The P wave reflection from the far face of the slab is just recognizable (by visual coherence from trace to trace) in the time interval from 140-160 μs. The P reflection event is preceded by a very large Rayleigh wave having a time length of about 100 μs. An X-T plot of the Rayleigh wave event is made using the minimum value of the wavelet as a phase reference point in the time window from 15-90 μs. The Rayleigh wave velocity determined by this method is V_R = 2400 m/s ± 20 m/s. The direct P and SV wave travelling from source to receiver are difficult to identify due to their small amplitude and close arrival times with the much larger Rayleigh wave.

Directive array synthesis of the data shown in Figure II-4-1 is performed using 5 unweighted traces to simulate the response of a 2 cm discrete array. The results of this summation are shown in Figure II-4-2, and display an immediate increase in the visual standout of the P wave reflection occurring at 140-160 μs. This increased standout results from the filtering effect of the directive array on the surface-travelling Rayleigh wave. The amplitude spectral response curves of a 5 element, 2 cm array for half-space velocities of 2400 m/s and 4600 m/s are shown in Figure II-4-3a,b. The frequencies of 40, 170, and 300 kHz were chosen to span the effective band generated by the laboratory P wave source. Cancellation of high-frequency Rayleigh waves (V_R = 2400 m/s) is easily observed in the response curve of Figure II-4-3a.

Deconvolution of the unprocessed P wave data (Figure II-4-1) is attempted using a source pulse measured on the far face of the granite slab directly beneath the P source plate. The measured waveform is

shown in Figure II-4-4, and exemplifies the complex seismic wavefield radiated from the P type piezoelectric plate used as a source. The difficulty in separating the direct body P wave from the complex series of events that comprise this waveform is obvious. Figure II-4-5a shows the part of the waveform which is due primarily to the direct P wave body event. This windowed event has been shifted to start at zero time in this figure to prevent the introduction of fictitious time lags during deconvolution processing. The amplitude spectrum of this estimated source pulse is shown in Figure II-4-5b.

The unprocessed P wave reflection data for a source-receiver separation of 8.5 cm is shown in Figure II-4-6a. This trace is also shown in Figure II-4-1 at the appropriate offset. The amplitude spectrum of this waveform is shown in Figure II-4-6b. Spectral division (deconvolution) is performed to remove the effect of the source wavelet from the received waveform. The amplitude spectrum of the deconvolved waveform resulting from the spectral division is shown in Figure II-4-7a, and the deconvolved waveform is shown in Figure II-4-7b.

Again, the primary effect of the deconvolution processing is to replace the P wave reflection event with a symmetric waveform which achieves maximum value at the arrival time of the reflection. Because of the choice of pass-band in this case, deconvolution has also filtered out the lower frequency components of the Rayleigh wave, thus improving the visual standout of the P reflection event. Wrap-around problems resulting from the use of a discrete FFT are visible at the beginning and end of the deconvolved record, but are not significant. These effects are clearly visible in Figure II-4-8, which is a decon-

volved version of the unprocessed P wave data shown in Figure II-4-1. The P reflection is clearly visible on most traces in the deconvolved record section.

The deconvolution technique is applied to the 2 cm array data shown in Figure II-4-2, with the results of this processing shown in Figure II-4-9. The action of both of these processing methods yields a clearly visible P reflection event in the time interval 132-144 μs. The arrival times of the P reflection are obtained from this section by picking the time corresponding to the maximum amplitude in the window from 120-160 μs. The P wave velocity derived from the least-squares X^2-T^2 plot is α = 4510 m/s ± 135 m/s, and the zero-offset arrival time is 134.9 μs ± 6.2 μ/s. The calculated depth to the reflector is 31.1 cm ± 1.7 cm, which agrees with the measured depth of 29.8 cm ± 0.2 cm.

Three velocity estimates have been made from the P and SH data sets measured on the granite slab. These results are:

P wave velocity	α = 4610 m/s
S wave velocity	β = 2610 m/s
Rayleigh wave velocity	V_R = 2400 m/s

Using the values for α and β, Poisson's ratio for the Raymond granite is calculated to be σ = 0.264, very typical for an unweathered granitic rock. For this value of Poisson's ratio, the Rayleigh wave velocity should be equal to 0.92β = 2400 m/s, which is equal to the observed Rayleigh wave velocity. Thus, the above values of α,β and V_R are internally consistent, and will be considered to be representative values for the Raymond granite.

The initial P wave experiments performed in the laboratory demonstrate the necessity of using data processing techniques in order to generate useful P wave reflection data. The large Rayleigh waves radiated from the laboratory P source are chiefly responsible for "masking" the P reflection in the unprocessed record section. Application of directive array synthesis and deconvolution processing are found to preferentially filter the Rayleigh waves, resulting in a visibly larger standout of the P wave reflection. Reflection arrival times can then be used in order to calculate the compression wave velocity using an X^2-T^2 analysis.

Figure Captions

Figure II-4-1
Unprocessed P wave reflection profile showing a very large Rayleigh wave (0-140 μs) preceding the faintly distinguishable P reflection (between 140-160 μs).

Figure II-4-2
Data in Figure II-4-1 summed in unweighted groups of 5 to simulate a discrete 2 cm array.

Figure II-4-3
Amplitude response as a function of incidence angle θ for a 5 element, 2 cm array for frequencies of 40, 170 and 300 kHz.
a) Half-space velocity V = 2400 m/s
b) Half-space velocity V = 4600 m/s

Figure II-4-4
Seismic wavefield measured beneath laboratory P wave source. Initial direct P wave pulse (60-100 μs) is followed by a complex series of other P and S events, causing the wavefield to be visibly complex.

Figure II-4-5
Truncated estimate of the direct P wavelet shown in Figure II-4-4 shifted to start at zero time to avoid time lags after deconvolution.
a) Estimated P source wavelet
b) Amplitude spectrum of the wavelet

Figure II-4-6
Unprocessed received P data at a 8.5 cm source-receiver offset. P reflection arrives at approximately 140 μs.
a) P receiver data
b) Amplitude spectrum

Figure II-4-7
Deconvolved P data resulting from division of receiver and source spectra.
a) Deconvolved amplitude spectrum
b) Inverse Fourier transform yields the time domain deconvolved P receiver data

Figure II-4-8
Results of applying deconvolution to unprocessed P data shown in Figure II-4-1. Note symmetrical P reflection visible on most traces in this record.

Figure II-4-9
Results of applying deconvolution to 2 cm array P data shown in Figure II-4-2. Note the easily distinguishable P wave reflection on all traces in this record.

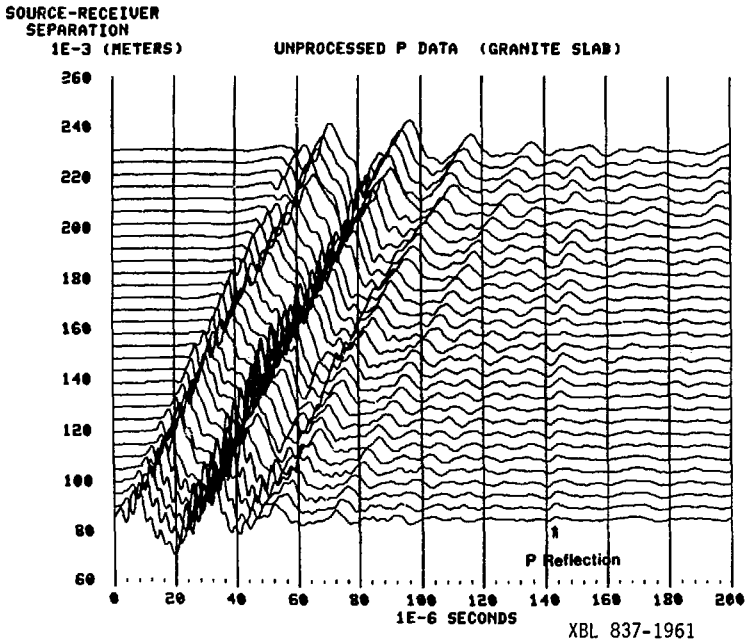

XBL 837-1961

Figure II-4-1

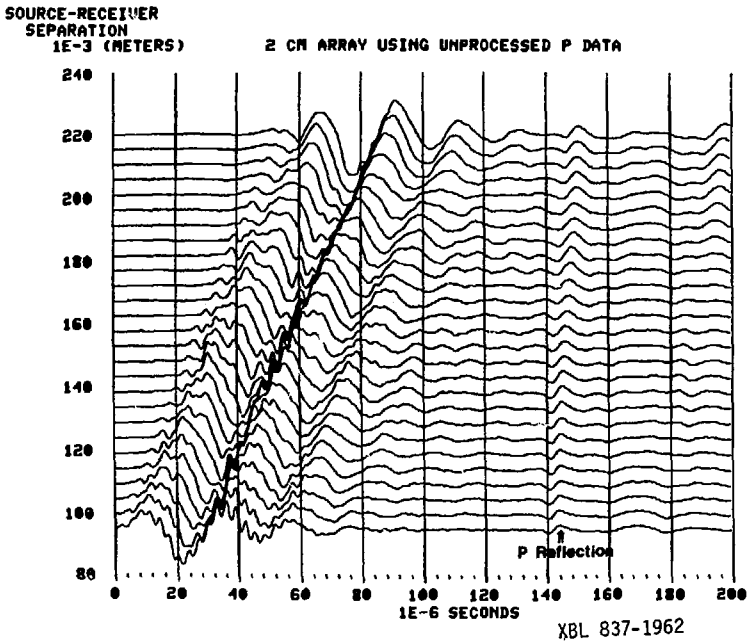
SOURCE-RECEIVER
SEPARATION
1E-3 (METERS)
2 CM ARRAY USING UNPROCESSED P DATA
240
220
200
180
160
140
120
100
80
0
20
40
60
80
100
120
140
160
180
200
1E-6 SECONDS
P Reflection
XBL 837-1962

Figure II-4-2

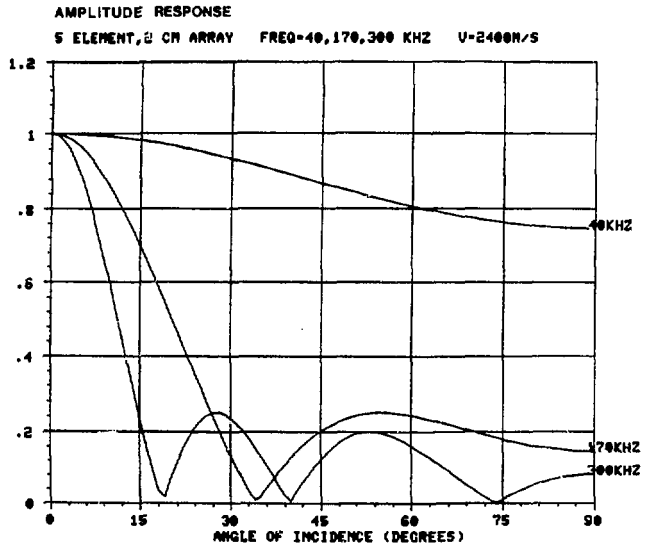

Figure II-4-3a

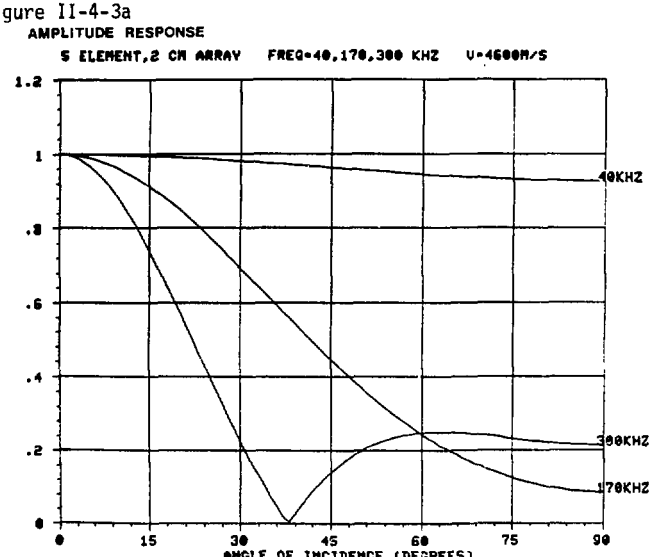

XBL 837-1963

Figure II-4-3b

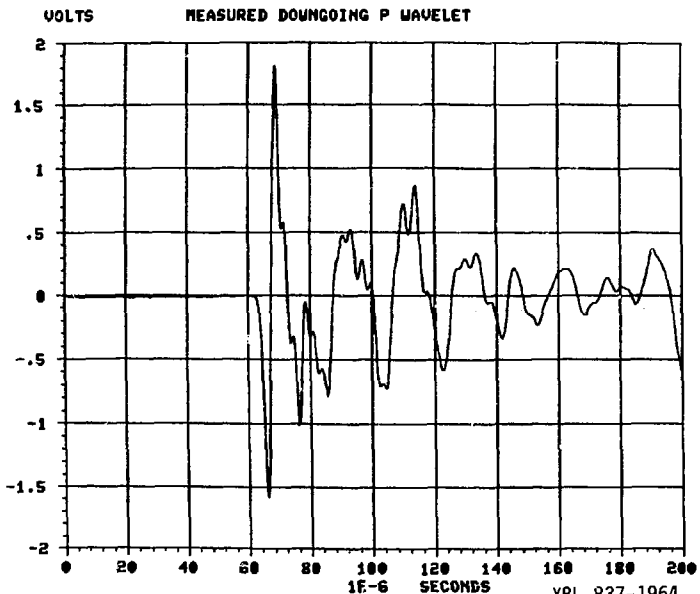
VOLTS
MEASURED DOWNGOING P WAVELET
2
1.5
1
.5
0
-.5
-1
-1.5
-2
0
20
40
60
80
100
120
140
160
180
200
1E-6 SECONDS
XBL 837-1964

Figure II-4-4

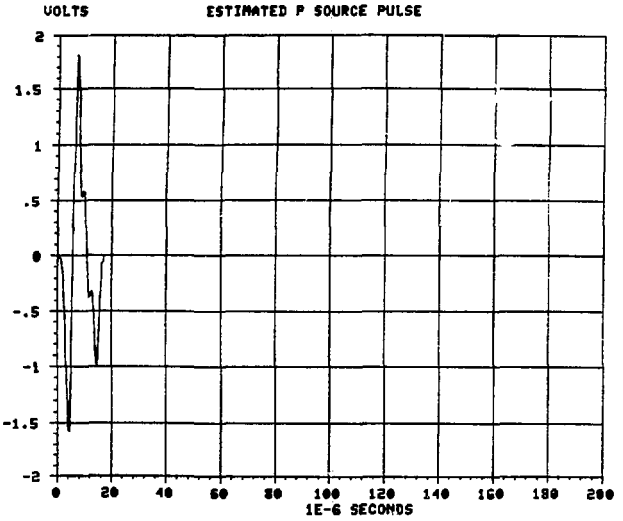

Figure II-4-5a

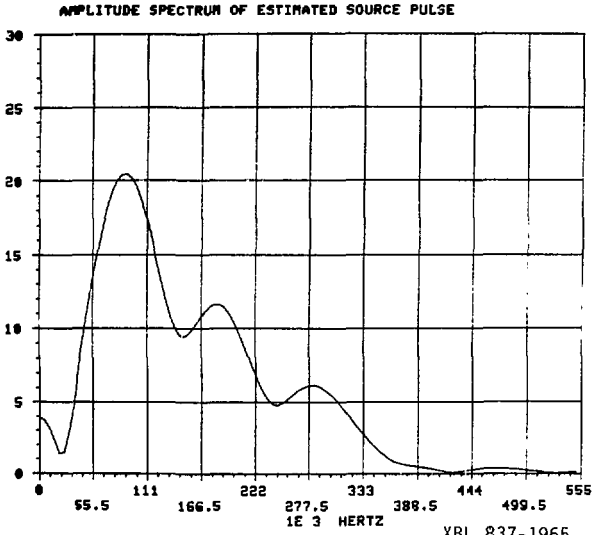

XBL 837-1965

Figure II-4-5b

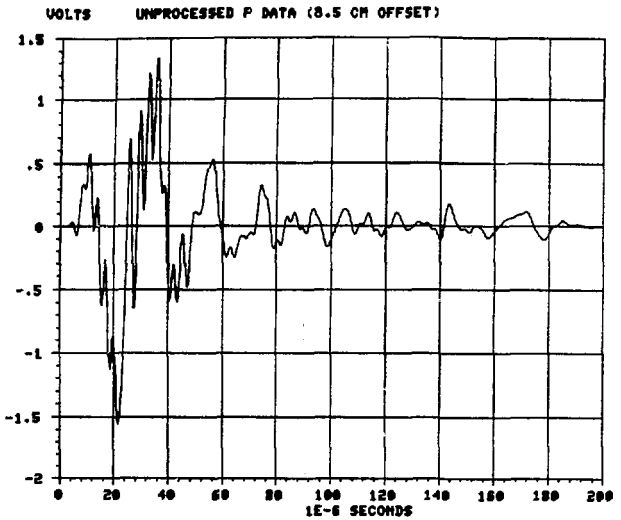

Figure II-4-6a

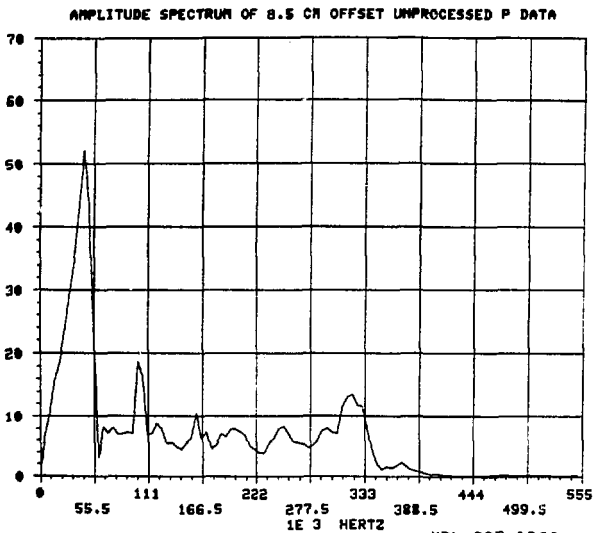

Figure II-4-6b

XBL 837-1966

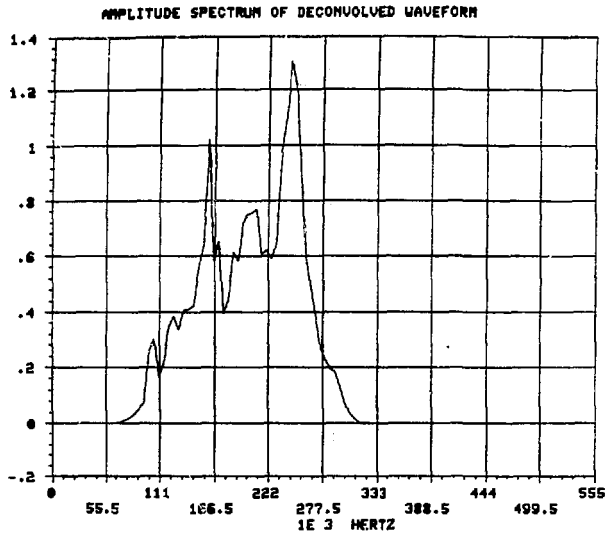

Figure II-4-7a

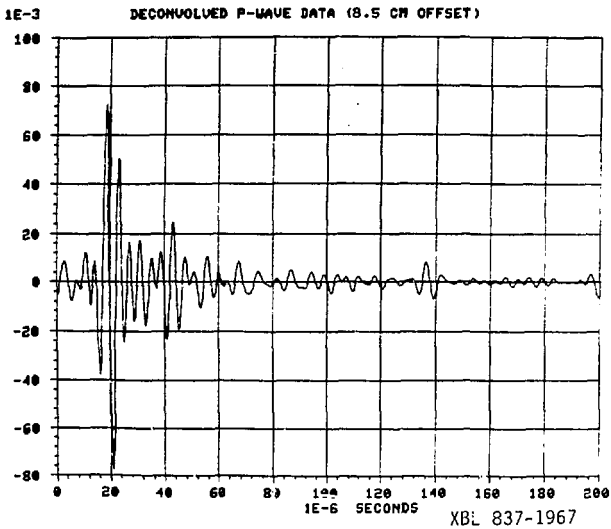

XBL 837-1967

Figure II-4-7b

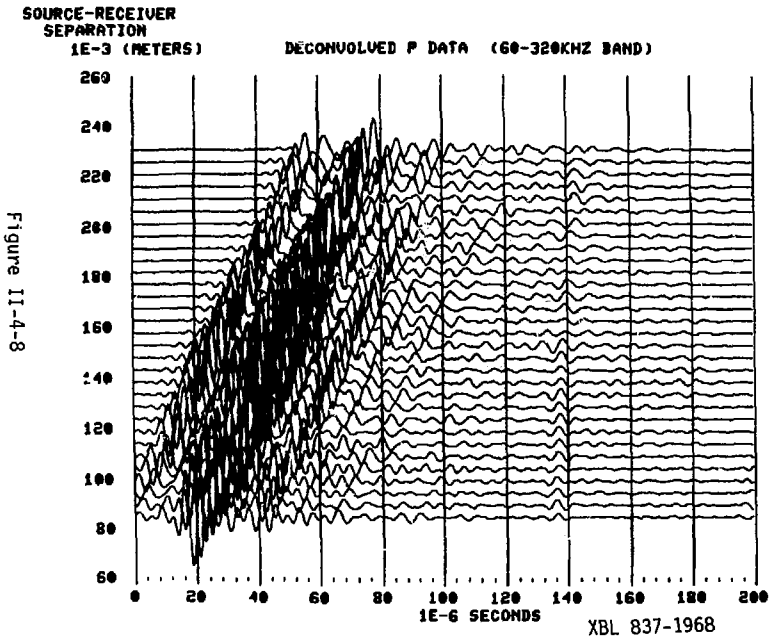
SOURCE-RECEIVER
SEPARATION
1E-3 (METERS)
DECONVOLVED P DATA (60-320KHZ BAND)
260
240
220
200
180
160
140
120
100
80
60
0
20
40
60
80
100
120
140
160
180
200
1E-6 SECONDS
XBL 837-1968

Figure II-4-8

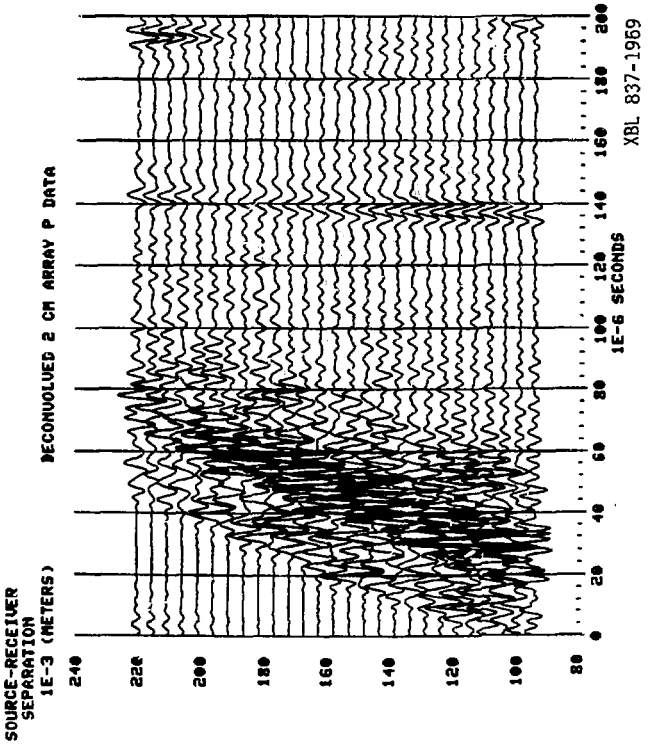
DECONVOLVED 2 CM ARRAY P DATA
SOURCE-RECEIVER SEPARATION 1E-3 (METERS)
240
220
200
180
160
140
120
100
80
0
20
40
60
80
100
120
140
160
180
200
1E-6 SECONDS
XBL 837-1969

Figure II-4-9

CHAPTER II

Section 5

Conclusions

The series of laboratory experiments detailed in this chapter have been conducted in an initial attempt to apply ultrasonic seismic reflection techniques in the detection of fracture discontinuities in a crystalline (granitic) rock. A theoretical study of the P and SH reflection coefficients from a simple planar fracture model was performed. The results of this study showed that the amplitude of the P wave reflection is small if the fracture is thin compared to the P wavelength within the fracture. Thus, it is necessary to have both P and SH reflection data in order to reliably detect both air and water-filled thin fractures and to determine the type of infilling fluid (air or water). Development of both P and SH reflection systems seemed to be desirable since information about the type of fracture interstitial material (gaseous or liquid) can be a critical engineering factor.

The initial SH experiments (performed on a 0.91 m × 0.91 m × 0.30 m granite slab) were successful in detecting a discrete reflection from the opposite face of the slab. Signal processing techniques borrowed from the field of exploration seismology, such as deconvolution and directive array synthesis, were used to improve the visual standout of the reflection event and to simplify the picking of arrival times. Experiments performed on a fractured granite model determined that an irregular, dipping fracture (as would be found in nature) can be easily detected using SH reflection methods.

It was much more difficult to obtain a distinct P wave reflection event in the laboratory study because of the presence of large amplitude Rayleigh waves emitted by the source. Application of deconvolution and directive array processing greatly improved the visual standout of the P reflection, and greatly simplified the determination of the reflection event arrival time. The application of these digital processing techniques was critical to the success of the initial P wave experiments. The results of these laboratory studies confirmed the practicality of using P and SH reflection methods in fracture detection at this size scale, and suggested that a field investigation of this technique should be performed.

References--Chapter II

Banks, B., Oldfield, G. E., and Rawding, H.; 1962; Ultrasonic Flaw Detection in Metals; Prentice-Hall, Inc.; Englewood Cliffs, N.J.; 256 pp.

Bevington, P. R.; 1969; Data Reduction and Error Analysis for the Physical Sciences; McGraw-Hill Book Co.; 336 pp.

Bycroft, G. N.; 1956; "Forced Vibrations of a Rigid Circular Plate on a Semi-Infinite Elastic Space And On An Elastic Stratum"; Philos. Trans. Royal Soc. London; Ser. A; V. 248; pp. 327-368.

Cherry, J. T.; 1962; "The Azimuthal and Polar Radiation Patterns Obtained from a Horizontal Stress Applied at the Surface of an Elastic Half Space"; Bull. Seismological Soc. America; V. 52; No. 1; pp. 27-36.

Cherry, J. T. and Waters, K. H.; 1968; "Shear-Wave Recording Using Continuous Signal Methods; Part I - Early Development"; Geophys.; V. 33; No. 2; pp. 229-239.

Erickson, E. L., Miller, D. E., and Waters, K. H.; 1968; "Shear-Wave Recording Using Continuous Signal Methods; Part II - Later Experimentation"; Geophys.; V. 33; No. 2; pp. 240-254.

Fehler, M. C.; 1979; Seismological Investigation of the Mechanical Properties of a Hot Dry Rock Geothermal System; submitted in partial fulfillment of the Ph.D. requirements, Massachusetts Institute of Technology; 344 pp.

Jolly, R. N.; 1956; "Investigation of Shear Waves"; Geophys.; V. 21; No. 4; pp. 905-938.

Krautkramer, J. and Krautkramer, H.; 1969; Ultrasonic Testing of Materials; Springer-Verlag, Ind.; New York; 521 pp.

Mason, W. P.; 1948; "Electrostrictive Effect in Barium Titanate Ceramics"; Physical Review; V. 74; No. 9; pp. 1134-1147.

Mason, W. A.; 1964; Physical Acoustics; V. 1; Part A; Academic Press; Washington, D.C.

Miller, G. F. and Pursey, H.; 1954; "The Field and Radiation Impedance of Mechanical Radiators on the Free Surface of a Semi-Infinite Isotropic Solid"; Proc. Royal Soc. London; Ser. A; V. 223; pp. 521-541.

Miller, G. F. and Pursey, H.; 1956; "On the Partition of Energy Between Elastic Waves in a Semi-Infinite Solid"; Proc. Royal Soc. London; Ser. A; V. 225; pp. 55-69.

Officer, C. B.; 1958; Introduction to the Theory of Sound Transmission; McGraw-Hill Book Co.; New York; 284 pp.

Pao, Yih-Hsing and Mow, Chao-Chow; 1973; Diffraction of Elastic Waves and Dynamic Stress Concentrations; Crane, Russak, and Co.; New York; 694 pp.

Rayleigh, Lord; 1945; The Theory of Sound; Dover Publications; New York; 2nd Edition; 504 pp.

Rzhevsky, V. and Movek, G.; 1971; The Physics of Rocks; Mir Publications; Moscow; 320 pp.

Telford, W. M., Geldart, L. P., Sheriff, R. E., and Keys, D. A.; 1976; Applied Geophysics; Cambridge University Press; London; 860 pp.

Waters, K. H.; 1981; Reflection Seismology; 2nd Edition; John Wiley and Sons; New York; 453 pp.

White, J. E., Heaps, S. N., and Lawrence, P. L.; 1956; "Seismic Waves from a Horizontal Force"; Geophys.; V. 21; No. 3; pp. 715-723.

Witherspoon, P. A., Amick, C. A., and Gaie, J. E.; 1977; "Stress-Flow Behavior of a Fault Zone with Fluid Injection and Withdrawal"; Annual report for period June 1, 1974 to December 30, 1976, to U.S. Geol. Survey under Contract no. 14-08-0001-14583; 159 pp.

CHAPTER III

Section 1

Introduction

The results of the preliminary laboratory study presented in Chapter II prompted a series of field experiments that were performed during the summers of 1979 and 1980. These experiments attempted to detect naturally occurring fractures *in situ* using the high frequency SH reflection techniques developed during the laboratory studies. A very suitable field site was found with the assistance of Bob Warnert of the Raymond Granite Company. This site is located in the Shaw quarry, an old granite monument and building stone quarry inactive since the Depression era of the 1930's. The Shaw quarry is located at the end of Road 411 near the town of Knowles, Madera County, California, and is easily located on the map in Figure III-1-1. Living accommodations at the nearby San Joaquin Experimental Range were provided through the courtesy of Jeanne Larson and Don Duncan of the United States Forest Service, Department of Agriculture.

A photograph of the particular site studied at the Shaw quarry is shown in Figure III-1-2. The SH reflection data were gathered on the sunlit, exposed face behind the truck in this photograph. This observation face is shown in greater detail in Figure II-1-3. The SH source and receiver are visible in the right-center of this picture mounted to the rock face.

The purpose of this study is to detect the two jointing fractures lying below the observation face as shown in Figure III-1-2. Only SH reflection methods were used during this field study since detection of the target fractures was deemed of primary importance. The results shown in Figure II-1-3 (Chapter II, Section 1) seemed to indicate that P wave reflection events from a thin (< 0.5 mm), water-filled fracture would be very small in amplitude in the frequency band 2-20 kHz, and consequently would be much more difficult to detect. Since reflection of SH waves from a water-filled fracture is assumed to be total, the use of SH reflection methods seemed preferable in the field experiments.

The two target fractures appear at the outcrop to be roughly parallel (within 5-10°) to the observation surface, so that mode conversion of the incident SH wavelet should not be a serious problem. The shallower of the two fractures, at a depth of approximately 1.5 m, is not continuous along the vertical cut near the truck in Figure III-1-2, and may not be completely continuous beneath the observation face. The deeper fracture, at a depth of approximately 2.5 m, is continuous across the vertical cut, and can be seen terminating in the exfoliation blocks at the top of the quarry. The visible lateral extent of this fracture strongly supports the assumption that at least this fracture extends beneath the locations of the SH traverses on the observation face. We then expect that there is a fracture discontinuity roughly parallel to the observation face and at a depth between 1 and 3 meters. The goal of these field experiments was to detect this probable fracture using ultrasonic SH reflection methods.

SH reflection data were collected during August and September of 1979 and 1980 at two locations on the observation face, as shown in Figure III-1-4. This figure may be compared to the photograph shown in Figure III-1-3. Two SH profiles were recorded at each location in an attempt to estimate both the dip and depth of the fracture, and the near-surface S velocity of the Shaw quarry granite. The SH source and receiver used in the field experiments were secured on the rock face with a platform attached to the surface using four 1/2" rock bolts (see Figure III-1-3). A close-up view of the SH source and receiver attached to the rock surface is shown in Figure III-1-5. The granite surface was ground flat along the traverse line in a strip about 10 cm wide so that good coupling of the source and receiver to the rock face would be insured.

The SH source was constructed using a 51 mm × 51 mm × 10 mm S piezoelectric plate mounted to an epoxy backing rod. The backing rod and source plate were connected by swivels to the support platform. The source plate was bonded to the rock surface using a piece of lead foil (to smooth surface irregularities) coated on both sides with a sticky resin (see Figure III-1-5). The receiver used in the field experiments is similar in design to the laboratory receivers, except that a 12.7 mm × 12.7 mm × 3.2 mm S plate was used in the field receiver. Again, this receiver is expected to have a relatively flat amplitude response because of its small size in comparison to the wavelength of the incident seismic waves.

It was not possible to transport the digital recording equipment to the field site, so it was necessary to use an analog tape recorder

to record the SH reflection data at the site. This analog recording could then be played back into the digital system at a later time. The instrumentation tape recorder used in this study was a Hewlett-Packard Model 3964A. Since this is a four channel recorder the receiver signal, trigger pulse, and a voice annotation could be simultaneously recorded. This particular model, at a tape speed of 15 ips, has a pass-band (± 3 dB) of 0.5-64 kHz, a time-base error of ± 4 μs, and a S/N ratio of 38 dB. The frequency band limitation of the tape recorder will not be important because of our choice of seismic frequencies for the field experiments. The timing error should not be significant as the digital sampling interval was set at 10 μs during the A/D conversion of the field tapes. The limitations on the dynamic range (S/N ratio) of the analog recorder may present a severe problem in recording reflected events that have been strongly attenuated.

Previous analyses have been based on the assumption of perfect elasticity, which provides only an idealized explanation of seismic wave propagation. Actual observations have shown that elastic energy is dissipated as a seismic wave propagates through rock. For the purposes of the following analysis, a specific model of anelastic attenuation will be adopted.

In this model, which is described by Aki and Richards, 1980, a plane seismic wave (P or S) is assumed to be travelling in the x direction, and the direction of maximum attenuation is along this axis. The attenuation factor Q is defined as:

$$1/Q = -1/\pi \frac{\Delta A}{A} \qquad [III.1.1]$$

where A is the maximum amplitude of a monochromatic plane wave, and ΔA is the loss of amplitude of the plane wave over one spatial cycle. The spatial attenuation of such a plane wave is described by:

$$A(x) = A_0 e^{-\left(\frac{\pi f |x|}{Qc}\right)} \qquad \text{[III.1.2]}$$

where, $A(x)$ = amplitude after the wave has travelled a distance $|x|$

A_0 = reference amplitude at $x = 0$

c = phase velocity of the wave

f = temporal frequency (Hertz).

The choice of phase velocity depends on whether compressional ($c = \alpha$) or shear ($c = \beta$) wave propagation is being considered. This model is commonly used in the geophysical literature (Johnson and Toksoz, 1980a; Winkler and Nur, 1981) in the quantitative analysis of anelastic attenuation in rock.

However, there is no specific requirement that the value of Q is the same for both P and S waves in a given material. In fact, if it is assumed that there is no elastic loss in the compressibility cycle of a seismic wave, then the following relation can be developed (Anderson and Archembeau, 1964):

$$Q_S/Q_P = 4/3\,[\beta^2/\alpha^2] \qquad \text{[III.1.3]}$$

where, Q_S = attenuation factor for S wave propagation

Q_P = attenuation factor for P wave propagation.

This kind of relation between Q_P and Q_S is typically observed in satu-

rated, porous sandstones (Johnson and Toksoz, 1980a), although it is unreported whether this effect occurs in low porosity granitic rocks.

Equation III.1.2 will be used to quantify the attenuation loss of a band-limited SH plane wave pulse due to anelastic effects. The choice of values for the variables in III.1.2 will attempt to approximate the conditions expected at the Shaw quarry. A typical S velocity for a Raymond (Shaw quarry) granite in air-dry room conditions is β = 2000 m/s, which is considerably less than the S velocity typical of the Raymond granite used in the laboratory models (β = 2600 m/s). An attenuation constant Q_p = 120 is quoted from Johnson and Toksoz, 1980b, for an air-dry Westerly granite at room temperature and pressure. The value Q_S = 55 is calculated using the relation given in Equation III.1.3. Since the fracture is expected at a depth of 1-3 meters, then the propagation distance $|x|$ will range from 2-6 meters. A_0, the reference amplitude at $|x| = 0$, is set equal to one.

These values are used to calculate the amplitude loss (in dB) as a function of propagation distance at three different frequencies (2, 10, and 20 kHz). The results of these calculations are presented in Figure III-1-6, and also denoted in this figure is the dynamic range of the analog tape recorder (-38 dB). If the reference amplitude is recorded on the analog recorder, then the -38 dB level represents the minimum amplitude signal that can be reproduced above the inherent background noise of the tape recorder. Attenuation of the SH reflection wavelet due to anelastic loss does not fall below the -38 dB level for the ranges of the variables used in these calculations. If anelasticity is the only loss mechanism acting on the SH wavelet, then both the

initial and attenuated wavelets can be recorded on the same channel within the 38 dB dynamic range of the recording machine. Since the 38 dB level represents the optimum dynamic range of the analog recorder, this analysis presents a "best case" estimate of the effects of anelastic attenuation on the amplitude of the recorded signal (SH reflection data).

However, the SH sources used in these experiments emit spherical, rather than plane, waves so that the consequent decay in amplitude due to spherical spreading of the SH wavefront must also be taken into account. In a typical field situation the depth to the reflector (fracture) is approximately 2-5 times the source-receiver offset distance. This means that the reflected SH event will travel about 4-10 times the distance of the direct SH event. Thus, the reflected event is reduced to 1/4-1/10 of the amplitude of the direct event by spherical spreading alone. This then represents an additional loss of -12 dB to -20 dB to the amplitude of the reflected SH event beyond any losses due to anelastic effects.

Since both geometric and anelastic attenuation will decrease the amplitude of the reflected SH wavelet, the loss due to geometric spreading should be included in the amplitude loss curves shown in Figure III-1-6. Since the geometric loss appears to be on the order of -12 to -20 dB, the curves in this figure should be decreased by this amount. However, even this additional loss causes the amplitude curves in Figure III-1-6 to become depressed below the -38 dB level only at the longest propagation distances and highest frequencies used in the calculations of these curves. The dynamic range of the analog tape recorder should

not severely limit the ability to reproduce a seismic trace containing both the direct SH event and a SH event reflected from a deep (> 2 m) fracture. The validity of this conclusion depends very strongly on the estimate of Q_S, which at best represents a limited guess at the actual value of Q_S at the Shaw quarry field site.

The SH reflection data recorded during this field study are presented in the following sections of this chapter. Processing and analysis of these data was performed in a manner similar to that used in the previous laboratory experiments. Two different models were developed to explain the origin of the events arriving after the direct SH body wave. The first model interprets these later arriving events as primary SH reflections from irregularly dipping fracture segments. This model assumes a homogeneous S velocity in the layer above the fracture, and that SH reflection from the fracture is total.

The second model used in interpreting the later-arriving events in the field data assumes that the S velocity of the granite at the survey site increases with depth. This inhomogeneous velocity structure will create a surface-propagating, dispersive Love wave in addition to the other SH body wave events expected in the seismic section. A dispersion analysis was performed on these later-arriving events to determine if these events could be interpreted as Love waves. However, presentation of the Love wave analysis will be deferred until Chapter V.

The analysis of the SH field data using the dipping reflector model was indecisive for a number of reasons. The ambiguity of these results suggested that further laboratory experiments be performed to investigate:

1) the assumption that SH reflection from a water-filled fracture is total, and,

2) the assumption of a homogeneous S velocity for the quarry granite.

The results of these laboratory experiments will be presented in Chapter IV.

Figure Captions

Figure III-1-1
Map of Madera County, California and surrounding area showing the location of the Shaw quarry.

Figure III-1-2
View of the study site at the Shaw quarry, showing the two fracture targets and observation face.

Figure III-1-3
Close-up view of the observation face showing the SH source and receiver bolted to the rock face at Location 2.

Figure III-1-4
Diagram of the position of Locations 1 and 2 on the observation face shown in Figure III-1-3.

Figure III-1-5
Detailed view of the field SH source and receiver shown in Figure III-1-3.

Figure III-1-6
Amplitude loss of a plane SH wave as a function of propagation distance at three different frequencies (2, 10, and 20 kHz). S velocity β = 2000 m/s and Q_S = 55 are used in the calculation of these curves.

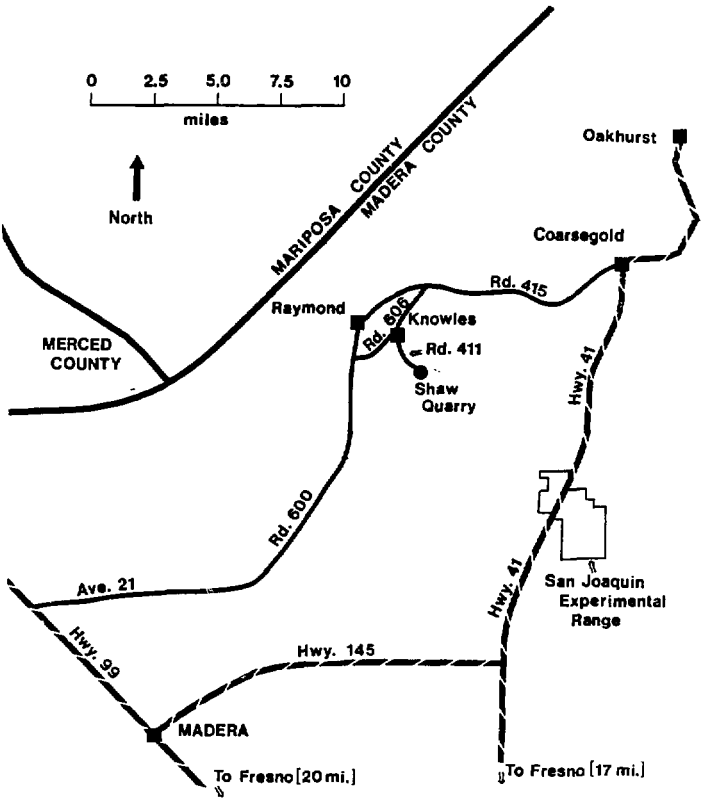

XBL 837-1970

Figure III-1-1

XBB 837-6605

Figure III-1-2

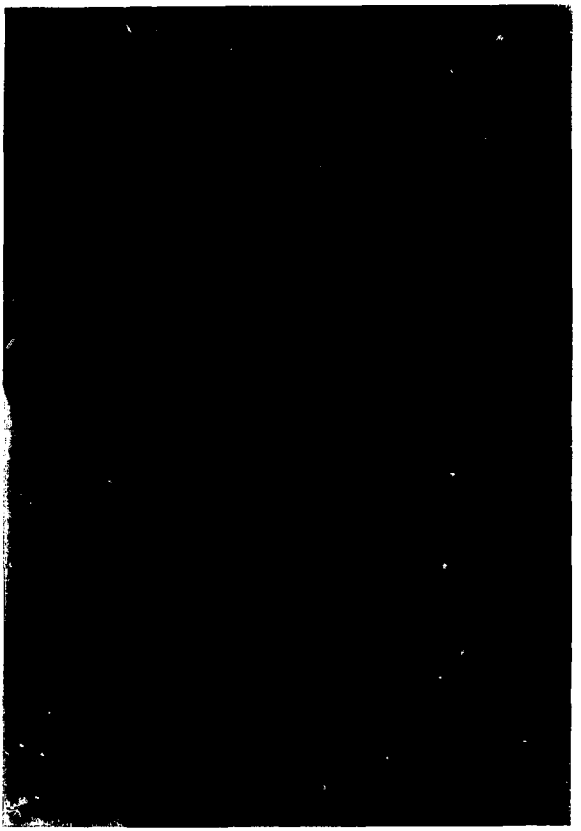

XBB 837-6606

Figure III-1-3

OBSERVATION FACE AT THE SHAW QUARRY

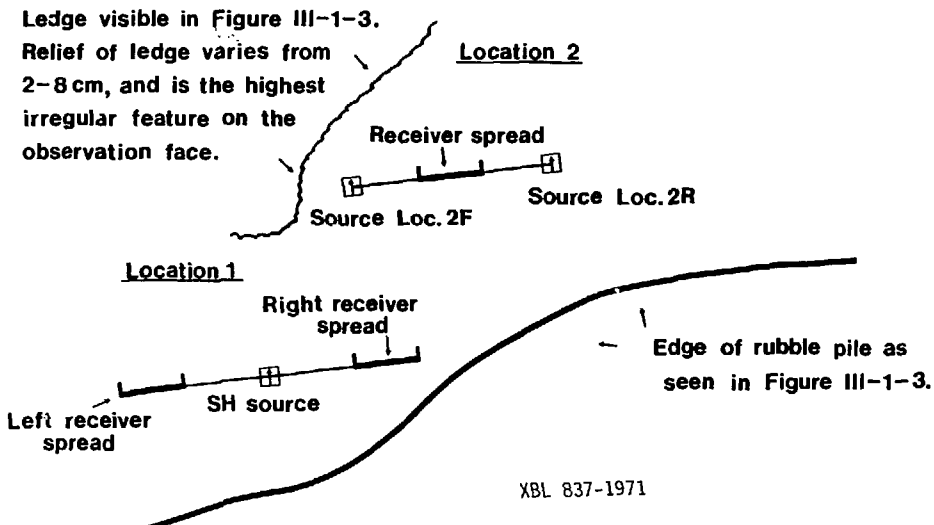

Figure III-1-4

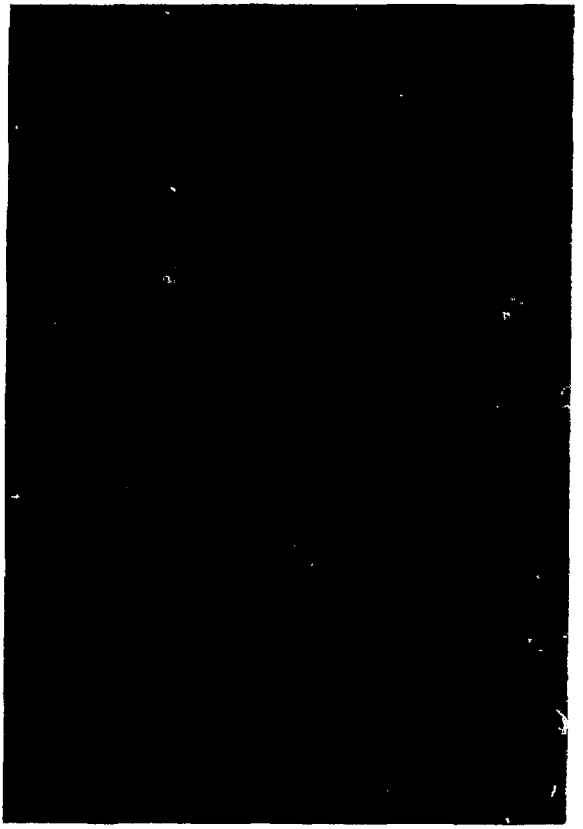

XBB 837-6604

Figure III-1-5

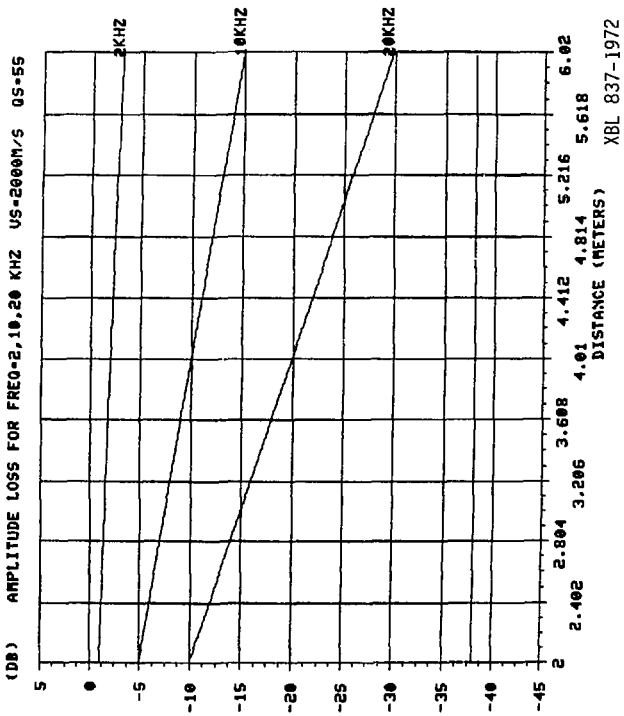

XBL 837-1972

Figure III-1-6

CHAPTER III

Section 2

Field Experiments at the Shaw Quarry

The SH field experiment performed at the Shaw Quarry during 1979 and 1980 are discussed in detail in this section. The unprocessed SH profiles recorded at the two survey locations are presented. Array synthesis techniques similar to those used in previous laboratory experiments were applied to the unprocessed field data. A number of events visible in these array-processed SH profiles could potentially be regarded as reflections from a subsurface fracture. Analysis of the arrival time data from these events was performed using a X^2-T^2 method modified to take into account reflection from a dipping, planar interface. The results of X^2-T^2 analysis at both survey locations are inconsistent with any model that uses only a single, dipping, planar reflector beneath each survey location. Rather, the arrival time data of these events requires that two planar reflector segments with opposing dips occur beneath each survey location.

A number of SH seismic profiles were recorded at two separate locations on the observation face, as shown in Figure III-1-4 (Section 1). A symmetric source-receiver spread, similar to the recording geometry used previously in the cylindrical laboratory model experiments, was used at field site Location 1. At site Location 2 a "split-spread" geometry was used (Dobrin, 1960). In this method a series of evenly spaced receivers record separate data sets for source positions that are symmetrically disposed to either side of the receiver spread.

The relationship between the dip angle of a reflecting interface and the moveout velocity obtained from the slope of the X^2-T^2 curve will be derived in the following analysis. The geometric model, shown in Figure III-2-1, consists of a planar, dipping reflector underlying a constant velocity layer. Two receivers are disposed symmetrically about a source in order to simulate the "symmetric spread" geometry. The planar reflector has a true dip angle θ from the horizontal when the profile line and dip direction of the reflector are parallel. When the profile line is not in the direction of dip, the angle θ is the apparent dip of the reflector, i.e., the projection of the true dip angle onto the vertical plane containing the profile line. The depth measured perpendicular to the reflector is denoted h, and the overlying layer is assumed to have a constant velocity V. The square of the reflection arrival times $T_U^2(X)$ and $T_D^2(X)$ at up-dip receiver R_U and down-dip receiver R_D are, respectively,

$$T_U(X)^2 = \frac{(X-2h\sin\theta)^2}{V^2} + \frac{4h^2\cos^2\theta}{V^2}$$

$$T_D(X)^2 = \frac{(X+2h\sin\theta)^2}{V^2} + \frac{4h^2\cos^2\theta}{V^2} \qquad \text{[III.2.1]}$$

If we define the instantaneous moveout velocity $\tilde{V}$ (valid for $x > 0$) as:

$$1/\tilde{V}^2 = \frac{T(X)^2}{X^2}, \qquad \text{[III.2.2]}$$

Then the moveout velocities $\tilde{V}_U$ and $\tilde{V}_D$ at receivers R_U and R_D are (neglecting the zero-offset constants):

$$\tilde{V}_U^2 = \frac{V^2X^2}{[X-2h\sin\theta]^2}$$

$$\tilde{V}_D^2 = \frac{V^2X^2}{[X+2h\sin\theta]^2} \qquad \text{[III.2.3]}$$

When $\theta = 0$ (no dip), then the moveout velocities become $\tilde{V}_U = \tilde{V}_D = V$, as is expected for a horizontal reflector underlying a constant velocity layer. For a non-zero dip θ at any $x > 0$, the moveout velocity $\tilde{V}_U$ determined using receivers located up-dip from the source is always greater than the constant propagation velocity V. Also the moveout velocity $\tilde{V}_D$ determined using receivers down-dip from the source is always less than V. This peculiar property of the moveout velocity will be used later in this section in the analysis of the SH field data.

The unprocessed SH data recorded in 1979 at Location 1 along the right receiver spread are shown in Figure III-2-2. The true amplitude of the individual SH traces was lost because of field recording procedures. In the field the amplifier gain was continuously adjusted to fully use the dynamic range of the tape recorder. Although these unprocessed data are "noisy," a number of arrival events occur in this record section that might be interpreted as reflected SH energy. The most obvious arrival events in Figure III-2-2 are in the direct SH event between 0.4-0.8 msec, and a later event occurring between 1.1-1.7 msec.

Directive array synthesis was found to smooth the irregularities in the unprocessed SH data, and to exhibit the expected cancellation properties. An 11 element array 10 cm in length was found to give adequate cancellation of horizontally propagating events, and minimum can-

cellation of events with small vertical angles of incidence (< 25°). The amplitude response curves for this array at three different frequencies (2, 10, and 20 kHz) for a half-space velocity of 2000 m/s are shown in Figure III-2-3. The amplitude spectrum of the unprocessed SH trace at .75 m offset in Figure III-2-2 is shown in Figure III-2-4. This figure shows that the frequency band of this SH field trace is limited to roughly 2-25 kHz, which was a typical bandwidth in these SH field experiments.

The array summed SH record section is shown in Figure III-2-5, where III-2-5b is an expanded scale version of the later time portion of III-2-5a (using a gain factor of four). The direct SH event is clearly visible between 0.4-1.0 msec, and three other events arriving later in time (termed events E#1, E#2, and E#3) are clearly coherent from trace to trace across Figure III-2-5. Event E#1 occurs between 1.1-1.7 msec, event E#2 between 2.1-2.7 msec, and event E#3 between 3.2-3.6 msec. The arrival times for all events were picked using the point of maximum amplitude within the time windows about each event shown in Figure III-2-5. Both X-T and X^2-T^2 best fits were obtained for all except the direct SH event. Table III-2-1 presents the velocities derived from the slopes of the X-T and X^2-T^2 curves, and the zero-offset constant from the X^2-T^2 fit. The S wave velocity along the right spread of Location 1 estimated using the direct SH event is 2080 m/s ± 55 m/s (from Table III-2-1). This value is then assumed to represent the constant layer velocity of the simple reflector model. The moveout (X^2-T^2) velocities of the three later events given in Table III-2-1 are slower than the assumed half-space velocity of

Table III-2-1

Location 1 Right Spread 1979

Event	X-T Velocity (m/s)	X^2-T^2 Velocity (m/s)	X^2-T^2 Arrival Time (msec)
Direct	2080 ± 55	————	————
E#1	3115 ± 85	1465 ± 45	1.159 ± 0.107
E#2	2825 ± 155	1045 ± 60	2.197 ± 0.213
E#3	6115 ± 1120	1290 ± 250	3.329 ± 0.311

granite (2080 m/s). Then the results of Equation III.2.3 indicate that the planar reflector associated with these events dips downward from source to receiver.

At this point it must be noted that if SH reflection from a fracture is total, then it is not possible to detect any fracture beyond the first encountered using SH reflection methods. Under this assumption events E#2 and E#3 cannot be interpreted as reflection arrivals from progressively deeper fractures, but must propagate along other possible raypaths. The relationship of the zero-offset arrival times suggest that events E#2 and E#3 could be the first and second multiple reflections of the primary SH reflection event E#1. However, the move-out velocities for these events are inconsistent with the expected move-out velocities of the first and second multiple reflections originating from the fracture associated with event E#1. Because of the assumption of total SH reflection at a fracture, only event E#1 will be interpreted as possibly being a primary SH reflection from a sub-surface fracture, and no further interpretation of events E#2 and E#3 was attempted in this study.

The unprocessed SH data recorded in 1980 at Location 1 along the left receiver spread are shown in Figure III-2-6. Again, arrival events are visible at later times in this somewhat "noisy" record section. These data are summed into an 11 element, 10 cm array as before, and the summed record section is shown in Figure II-2-7. Three distinct later-arriving events (E#1, E#2, and E#3) are coherent from trace to trace across Figure III-2-7. These three events can also be correlated by arrival time to events E#1-3 observed in the right spread data shown in

Figure III-2-5. The arrival times for the three events are again obtained by using the point of maximum amplitude within the time windows about each event (see Figure III-2-7). Again X-T and X^2-T^2 fits were obtained for each arrival time data set, and the results of these calculations are presented in Table III-2-2.

The constant S wave velocity of the layer beneath the left spread is estimated using the direct SH event, and has a value of 1995 m/s ± 50 m/s. This is in good agreement with the previous estimate from the right spread data (2080 m/s ± 55 m/s).

The moveout velocity obtained for event E#1 left-spread data is slower than the S wave velocity estimate obtained from the direct SH event (1995 m/s). The slower moveout velocity of event E#1 again indicates that the reflector associated with this event dips downward along the receiver profile.

The X^2-T^2 analysis of events E#1 in the left and right-spread data at Location 1 indicate that the reflector associated with this event must dip downward from the source along both receiver spreads. Thus, any interpretation that associates only a single planar reflector with event E#1 will not be consistent with the arrival time data of this event.

The perpendicular depth to the reflector h and dip angle θ of a single planar reflector beneath a receiver spread can be calculated using the constant layer velocity V, the zero-offset arrival time T(0), and the reflection arrival time $T(X_0)$ at an offset distance X_0. Using the results in Equations III.2.1 and 3 for the case in which the receivers are downdip from the source ($\tilde{V}_D < V$), h and θ are given by:

Table III-2-2

Location 1 Left Spread 1980

Event	X-T Velocity (m/s)	X^2-T^2 Velocity (m/s)	X^2-T^2 Zero-Offset Arrival Time (msec)
Direct	1995 ± 50	———	———
E#1	2700 ± 110	1350 ± 60	1.108 ± 0.136
E#2	2585 ± 90	1025 ± 40	2.060 ± 0.178
E#3	2535 ± 160	850 ± 60	3.028 ± 0.285

$$h = \frac{T(0)V}{2} \qquad \text{[III.2.4]}$$

$$\theta = \sin^{-1}\left[\frac{[T(X_0)^2 - T(0)^2]V}{2X_0T(0)}\right] \qquad \text{[III.2.5]}$$

The zero-offset arrival time T(0) is obtained as a result of the X^2-T^2 best-fit analysis of the reflection event, and the constant layer velocity V is estimated using the X-T moveout of the direct SH event. The arrival time $T(X_0)$ is obtained using both the moveout velocity $\tilde{V}$ and zero-offset constant T(0) determined from the X^2-T^2 fit in the equation:

$$T(X_0)^2 = \frac{X_0^2}{\tilde{V}^2} + T(0)^2 \qquad \text{[III.2.6]}$$

The depth h and dip angle θ associated with event E#1 are determined for each receiver spread at Location 1 separately, and the results of these calculations are summarized in Table III-2-3.

Figure III-2-8 is a view of the vertical plane through the SH profile at Location 1, showing the source and receiver positions, and the interpreted location of the reflector segments associated with event E#1. Because of geometric considerations a finite length receiver spread will sample reflected energy from a proportionally smaller length along the reflecting interface (Waters, 1982). Thus only the portion of the reflector E#1 actually sampled by the left and right receiver spreads is shown in Figure III-2-8. An explanation of the graphical method used to determine the portion of a dipping reflector sampled by a finite length receiver spread is given in Appendix I.

Table III-2-3

	Event E#1 Left Spread Location 1	Event E#2 Right Spread Location 1
Constant Layer Velocity V(m/s)	1995	2080
Moveout Velocity $\tilde{V}$(m/s)	1350	1465
Zero-Offset Arrival Time T(0) (msec)	1.108	1.159
Calculated Arrival Time $T(X_0)$ at X_0 = 1.0 m (msec)	1.333	1.345
Calculated Depth h (m)	1.11	1.21
Calculated Dip Angle θ	29.6°	24.7°

In Figure III-2-8 the dip of the reflector segments is consistent with the slow moveout velocity of event E#1 along each receiver spread. However the steep dip of these reflectors causes the portion of the reflector sampled by the receiver spread to be displaced laterally. In this particular case the reflector segment associated with the right receiver spread is displaced to the left of the source, and likewise the segment associated with the left spread is displaced to the right of the source. This figure demonstrates that the true reflection point migrates updip from the mid-point of a source-receiver pair.

Three SH data sets were recorded at Location 2 using the "split-spread" geometry previously described. The forward traverse at this location (Loc. 2F) was surveyed separately in 1979 and 1980 as a test of the yearly repeatability of the SH reflection data. A single reverse profile (denoted Loc. 2R) was recorded during 1980 at this location. The position of Location 2 on the observation face at the quarry is shown in Figure III-1-4 (Section 1).

Figure III-2-9 shows the unprocessed SH data recorded at Loc. 2F during the summer of 1979. A direct SH event is clearly observable (0.15-0.60 msec), and other later-arriving events are visibly coherent from trace to trace. The unprocessed traces are summed into 10 cm array as before, and the summed record section is shown in Figure III-2-10. The largest amplitude event arriving after the direct SH event occurs between 1.1-2.0 msec, and will be termed event E#1. The arrival times of event E#1 at Loc. 2F have good correspondence with the arrival times of event E#1 observed at Location 1.

Figure III-2-11 shows the unprocessed SH data recorded at Loc. 2F during the summer of 1980. Events on this record section are easily correlated with those on the section recorded in 1979 at this same location (shown in Figure III-2-9). The unprocessed SH data shown in Figure III-2-11 is summed to simulate the response from an 11 element, unweighted 10 cm array, and the resulting summed SH record section is shown in Figure III-2-12. Comparison of this figure and Figure III-2-10 shows that major events arriving before 2.0 msec are easily correlated in both of these SH profiles. In fact the summed SH data recorded at this location during 1979 and 1980 is visually very repeatable.

As before, the arrival times of the direct SH event and E#1 were picked using the point of maximum amplitude within the time window about each event. The arrival time data sets obtained at Loc. 2F during 1979 and 1980 were analyzed using X-T and X^2-T^2 methods. The X-T and X^2-T^2 velocities, and X^2-T^2 zero-offset arrival time obtained from this analysis, are given in Table III-2-4. The velocity values shown in this table for the 1980 survey at Loc. 2F are consistently 5-7% lower than the velocities obtained from the 1979 survey at this location.

Only the SH data recorded in 1980 at Location 2 will be treated in the following analysis. The S wave velocity of the constant velocity layer at Loc. 2F is estimated from the direct SH to be 1925 m/s ± 25 m/s. The moveout velocity (930 m/s ± 20 m/s) for event E#1 along this profile is much slower than the estimated S velocity of the granite (1925 m/s). Again, this slower moveout velocity indicates that the reflector associated with E#1 has a component of dip with the receivers down-dip from the source.

Table III-2-4

Location (Year)	Event	X-T Velocity (m/s)	X^2-T^2 Velocity (m/s)	X^2-T^2 Zero-Offset Arrival Time (msec)
2F (1979)	Direct	2050 ± 25	———	———
	E#1	2040 ± 35	1000 ± 20	1.190 ± 0.097
2F (1980)	Direct	1925 ± 20	———	———
	E#1	1730 ± 25	930 ± 20	1.146 ± 0.104
2R (1980)	Direct	1880 ± 25	———	———
	E#1	1785 ± 30	935 ± 15	1.171 ± 0.092

The unprocessed SH data recorded at Loc. 2R during 1980 are shown in Figure III-2-13, and the summed 10 cm array profile is shown in Figure III-2-14. Again, the direct SH event (0.15-0.70 msec) and event E#1 (0.90-2.0 msec) are clearly visible in this figure. Arrival times for these events were determined using the point of maximum value within the time windows shown about each event. X-T and X^2-T^2 analyses of these arrival time data were performed, and the results of these calculations are shown in Table III-2-4. Once again the results of the direct and moveout velocities indicate that the reflector must dip downward from source to receiver.

Figure III-2-15 is a view of the vertical plane through the profile line at Location 2, showing the source and receiver positions, and the reflector segments calculated from E#1 arrival time data at each source position. The perpendicular depth h and dip angle θ are determined separately for each receiver spread at Location 2 using Equations III.2(4 and 5), and the results of these calculations are given in Table III-2-5. From these results the positions of these reflector segments are derived using the graphical method described in Appendix I. The arrival times data for event E#1 require that the reflectors have a very steep dip, and as a consequence the reflection point for a given source-receiver pair is displaced laterally, as seen in Figure III-2-15. This lateral displacement requires that the steeply dipping reflector segments be located quite near the ground surface, and not at the 1-3 meters depth expected from the outcrop projection of the two target fractures. Visual inspection of the observation face demonstrated that these hypothetical fracture segments did not extend vertically and outcrop on the surface near Location 2.

Table III-2-5

	Event E#1 Loc. 2F	Event E#1 Loc. 2R
Constant Layer Velocity V(m/s)	1925	1880
Moveout Velocity $\tilde{V}$(m/s)	930	935
Zero-Offset Arrival Time T(0) (msec)	1.146	1.171
Calculated Arrival Time $T(X_0)$ at Offset X_0 = 1.0 m (msec)	1.571	1.586
Calculated Depth h (m)	1.10	1.10
Calculated Dip Angle θ	75.9°	66.7°

In review, a number of later-arriving events were observed in the SH reflection data recorded at two locations at the Shaw quarry in 1979 and 1980. These later-arriving events were interpreted using a model based on the following two assumptions:

1) SH reflection from the first fracture encountered is total, and,
2) the S wave velocity of the quarry granite at the survey location is constant.

Because of the first assumption, only the major arrival occurring between 1-2 msec (and termed event E#1) could be interpreted as a primary SH reflection from a fracture. Events arriving after E#1 (termed E#2 and E#3 at Location 1) could not then be considered as primary SH reflections from deeper fractures, and no further analysis of these events was attempted.

An X^2-T^2 analysis of event E#1 was performed on the SH reflection profiles recorded at both locations. The results of these analyses indicate that the observed arrival times of E#1 cannot be explained using only a single, dipping, planar fracture as a model. However, two planar fracture segments with opposing dips can be used as a model that is consistent with the arrival times of event E#1 (see Figures III-2-(8 and 15)) at both survey locations. To this point we have tried to interpret the field data using a model in which the event E#1 is considered as the primary SH reflection from a sub-surface fracture. At each receiver spread, interpretation of event E#1 indicated that the reflector associated with this event dips downward from source to receiver. The coincidence that a down-dip interpretation is required

for each SH profile recorded during this field study is indeed suspicious, and alternate interpretations of event E#1 should be sought.

An X-T fit of the arrival time data for event E#1 was also performed at both survey locations, and the phase velocities derived using this X-T fit are given in Tables III-2-(1, 2, and 4). These velocities all range in value from 1700-3100 m/s, which is within the range of S wave velocities observed for a Raymond granite. The uncertainties in the phase velocity estimates summarized in these tables are no larger, in percentage terms, than the uncertainties in the moveout velocity derived from the X^2-T^2 fit. Using the percentage uncertainty as a criterion, neither of the X-T or X^2-T^2 fits to the arrival time data of event E#1 are superior to the other.

The good X-T fit to event E#1 suggests that this event may propagate in a direction nearly parallel to the ground surface. If horizontal propagation is assumed, the apparent velocities of event E#1 obtained using Equation II.3.1 (Chapter II, Section 3) fall within the range of S velocities observed in field and laboratory specimens of Raymond granite. These observations suggested that a second model be considered in the interpretation of event E#1. In this model, event E#1 was interpreted as a fundamental mode Love wave, and a dispersion analysis of this event was performed. However, in keeping with the basic chronological order of this dissertation, the Love wave analysis of the SH field data will be deferred until Chapter V, the concluding chapter.

Figure Captions

Figure III-2-1
Geometry of a dipping, planar reflector underlying a constant velocity layer. Reflector has a dip angle θ from the horizontal, and a perpendicular depth h. Layer has a constant velocity V. R_U is the up-dip receiver, and R_D is the down-dip receiver.

Figure III-2-2
Unprocessed SH data recorded along the right spread at Location 1 during 1979. Straight line traces indicate that no SH data could be recorded at that particular offset.

Figure III-2-3
Amplitude response of an unweighted 11 element array 10 cm in length for frequencies of 2, 10, and 20 kHz. Half-space velocity is 2000 m/s.

Figure III-2-4
Amplitude spectrum of the unprocessed SH trace shown in Figure III-2-2 at a 0.75 m offset. Note that the frequency band of the trace is limited to the range of 2-25 kHz.

Figure III-2-5
Array summed SH profile obtained using the unprocessed right spread data in Figure III-2-2. 11 unprocessed traces are summed into a 10 cm linear array. Arrival times for the direct SH event, and events E#1-3, are obtained by picking the point of maximum amplitude within the time windows shown about each event.
a) Summed traces clearly showing direct SH event and event E#1
b) Expanded scale version of a) using a gain of four to more clearly show events E#2 and E#3

Figure III-2-6
Unprocessed SH data recorded along the left spread at Location 1 during 1980.

Figure III-2-7
Unprocessed left spread data summed to give response of an unweighted 11 element array 10 cm in length. Arrival times of events picked using the point of maximum amplitude within the time windows shown.
a) Summed traces clearly showing direct SH and event E#1
b) Expanded scale version of a) using a gain of four

Figure III-2-8
View of the vertical plane through the SH profile at Location 1, showing the source and receiver positions, and the interpreted locations of the reflector segments associated with event E#1. The locations of these reflector segments were determined using the graphical method described in Appendix I.

Figure III-2-9
Unprocessed SH data recorded at Loc. 2F during the summer of 1979.

Figure III-2-10
Unprocessed SH data at Loc. 2F (1979) summed to give response of an 11 element array 10 cm in length. Arrival times of events are picked using the point of maximum amplitude within the time windows shown.

Figure III-2-11
Unprocessed SH data recorded at Loc. 2F during the summer of 1980. Comparison of this figure and Figure III-2-9 gives a visual comparison of the yearly repeatability of the SH data recorded at a particular location.

Figure III-2-12
Unprocessed SH data at Loc. 2F (1980) summed to give response of an 11 element array 10 cm in length. Arrival times of events are picked using the point of maximum amplitude within the time windows shown. Comparison of this figure and Figure III-2-10 gives a visual comparison of the yearly repeatability of the summed SH data sets recorded at this location.

Figure III-2-13
Unprocessed SH data recorded at Loc. 2R during the summer of 1980.

Figure III-2-14
Unprocessed data recorded at Loc. 2R summed to give response of an 11 element array 10 cm in length. Arrival times are picked using the point of maximum amplitude within the time windows shown.

Figure III-2-15
View of the vertical plane through the SH profile at Location 2, showing the source and receiver positions, and the interpreted locations of the reflector segments associated with event E#1. The locations of these reflector segments were determined using the graphical method described in Appendix I.

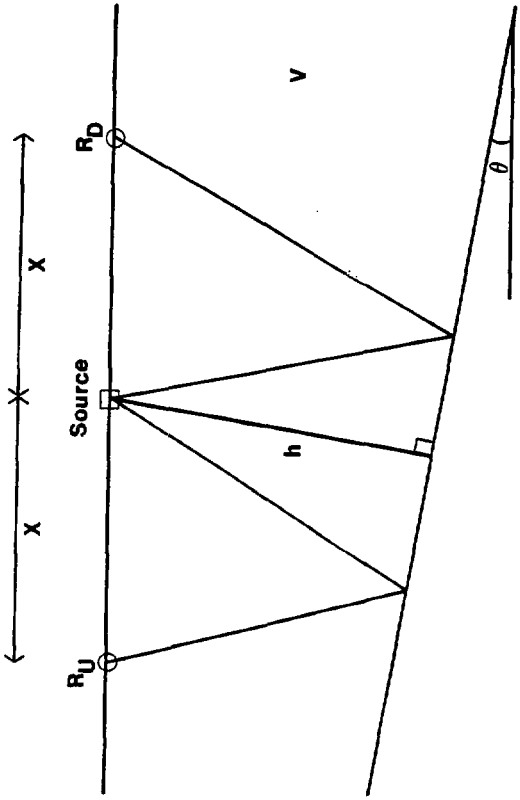

XBL 837-1973

Figure III-2-1

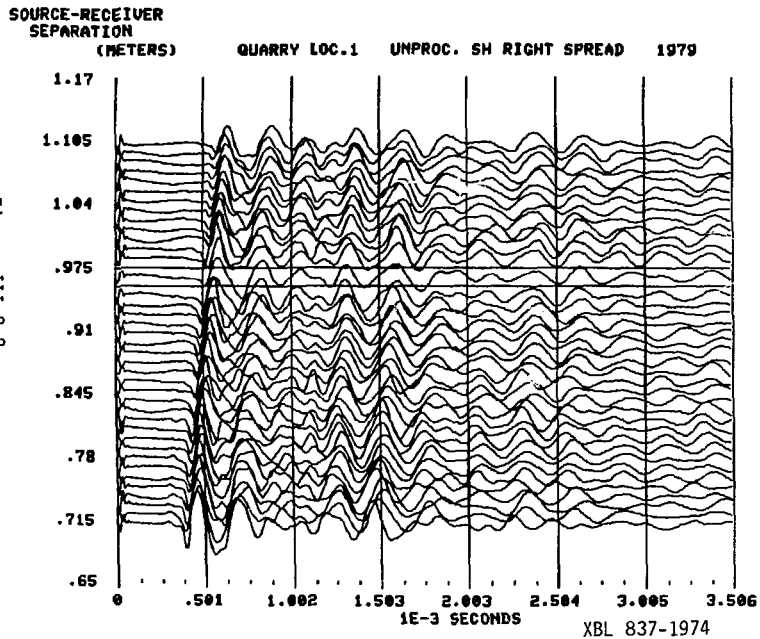

XBL 837-1974

Figure III-2-2

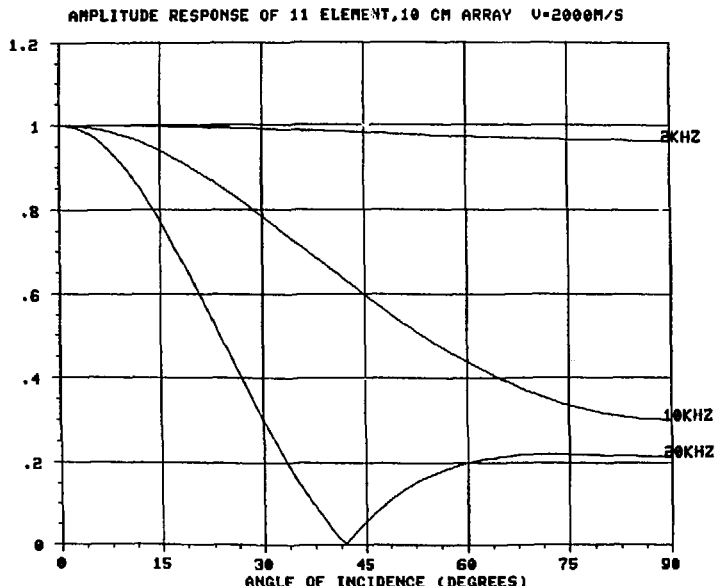

XBL 837-1975

Figure III-2-3

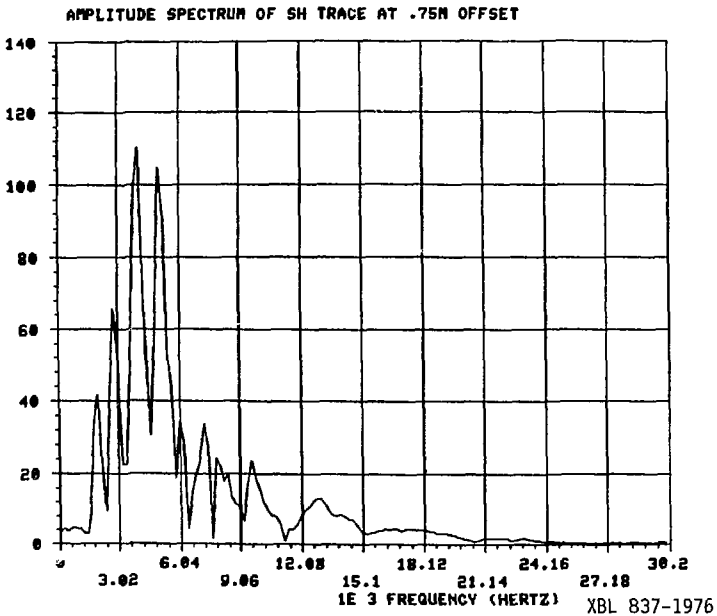

XBL 837-1976

Figure III-2-4

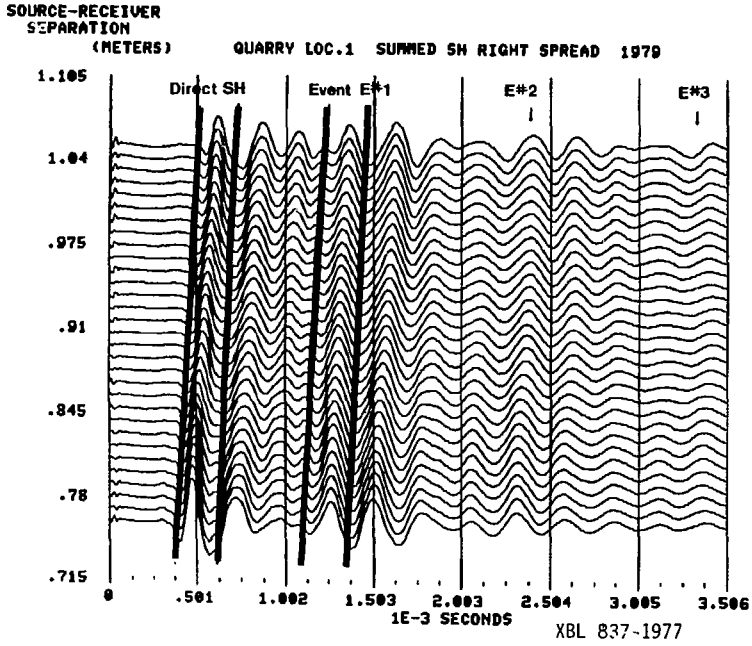

Figure III-2-5a

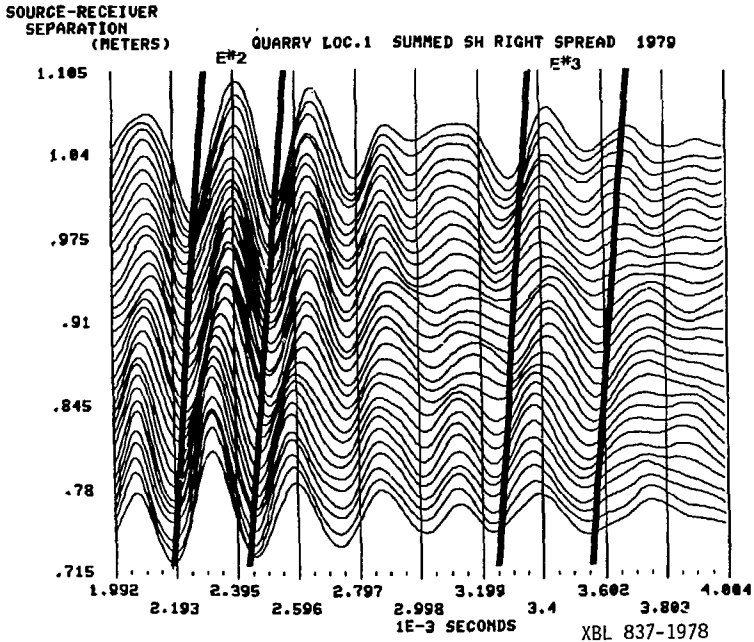

Figure III-2-5b

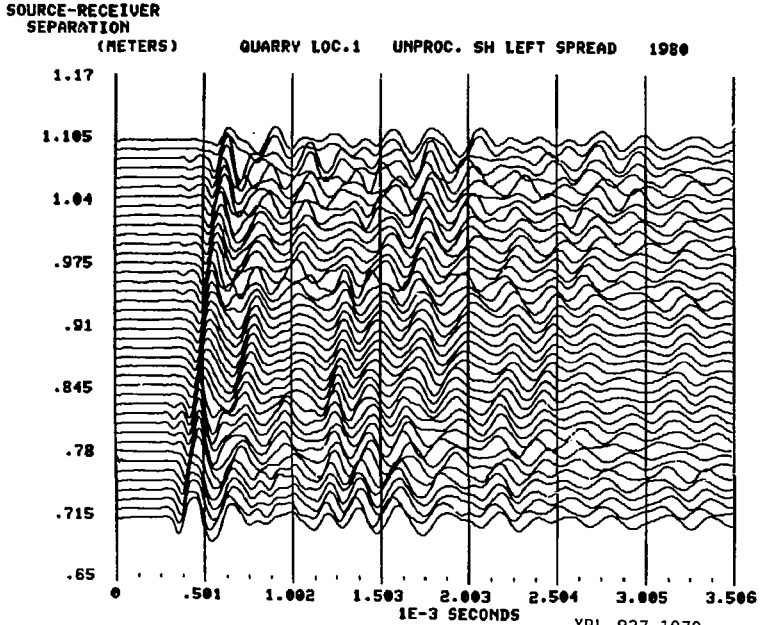

XBL 837-1979

Figure III-2-6

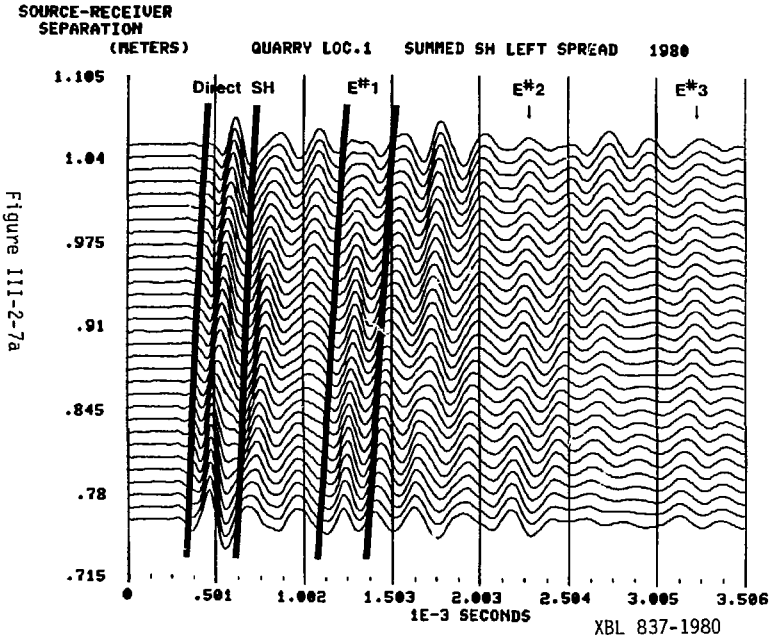

Figure III-2-7a

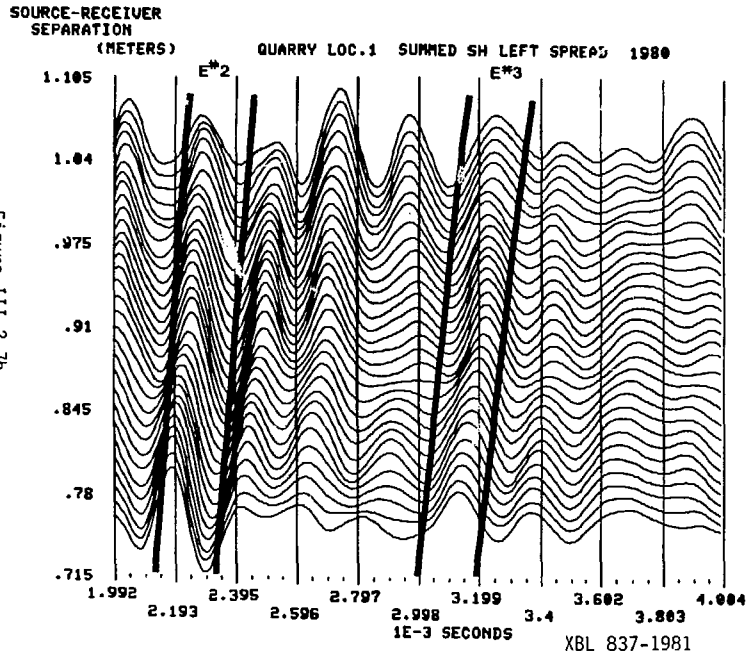

Figure III-2-7b

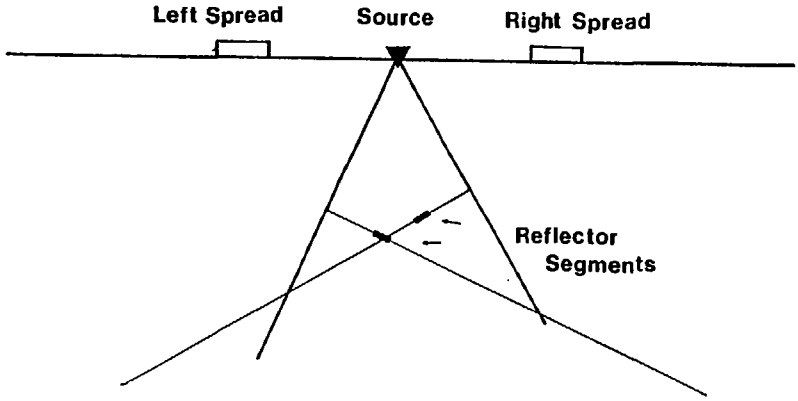

LOCATION #1

XBL 837-1982

0 75
cm

Figure III-2-8

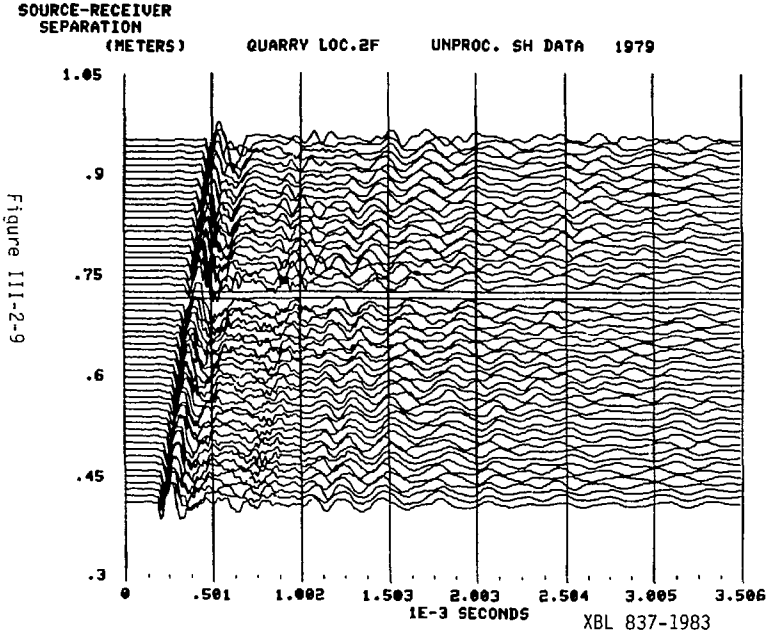

Figure III-2-9

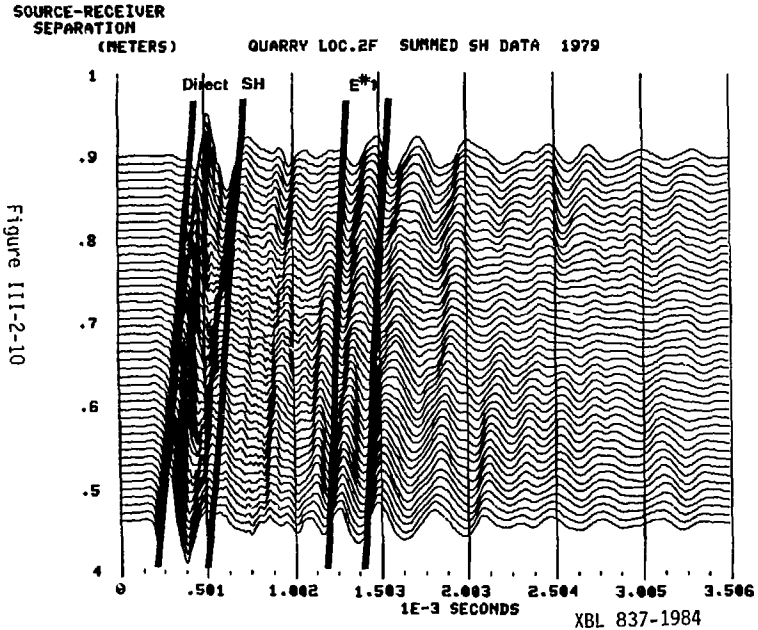

XBL 837-1984

Figure III-2-10

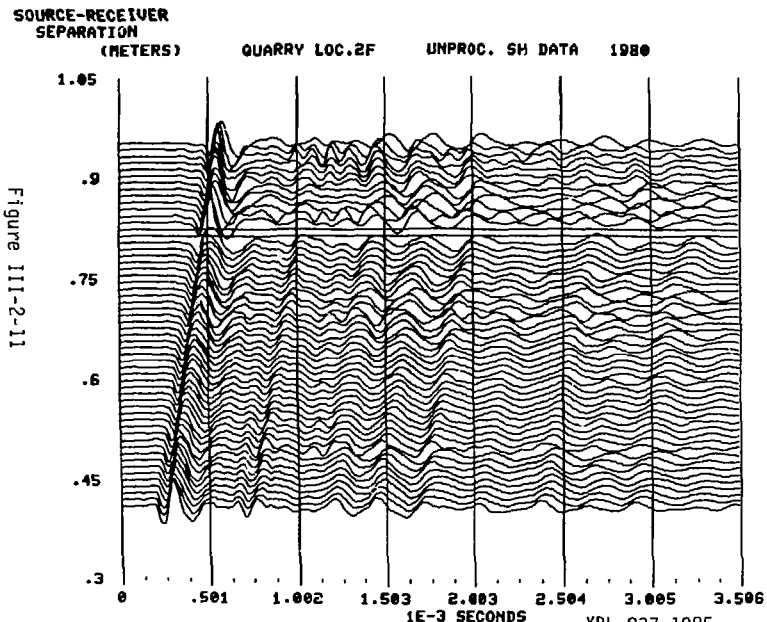

XBL 837-1985

Figure III-2-11

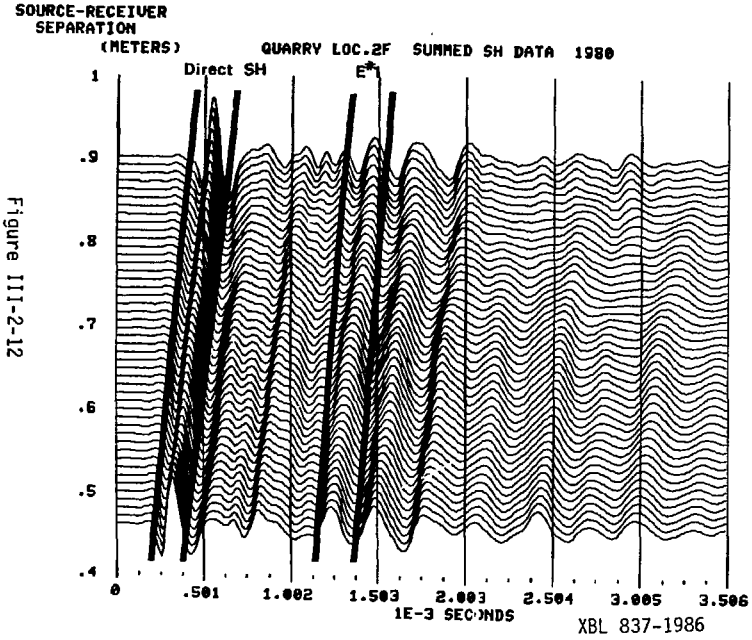

XBL 837-1986

Figure III-2-12

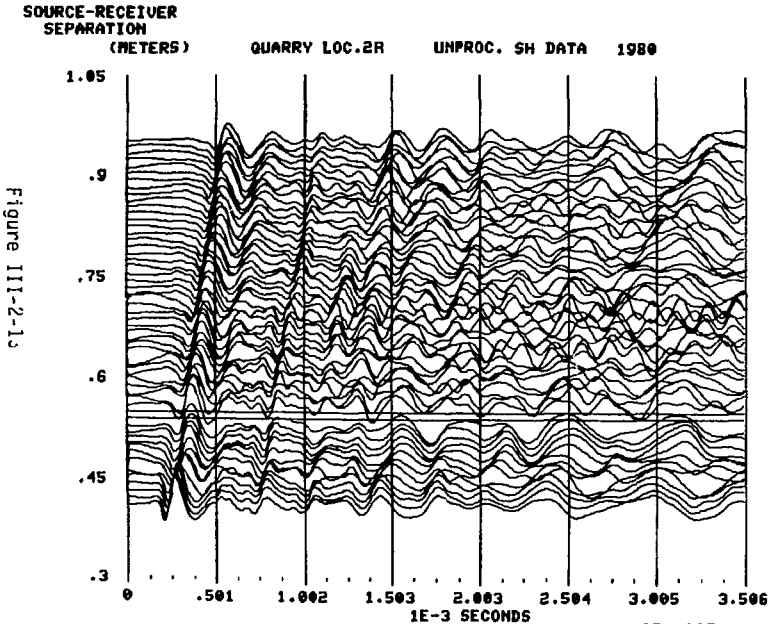

XBL 837-1987

Figure III-2-13

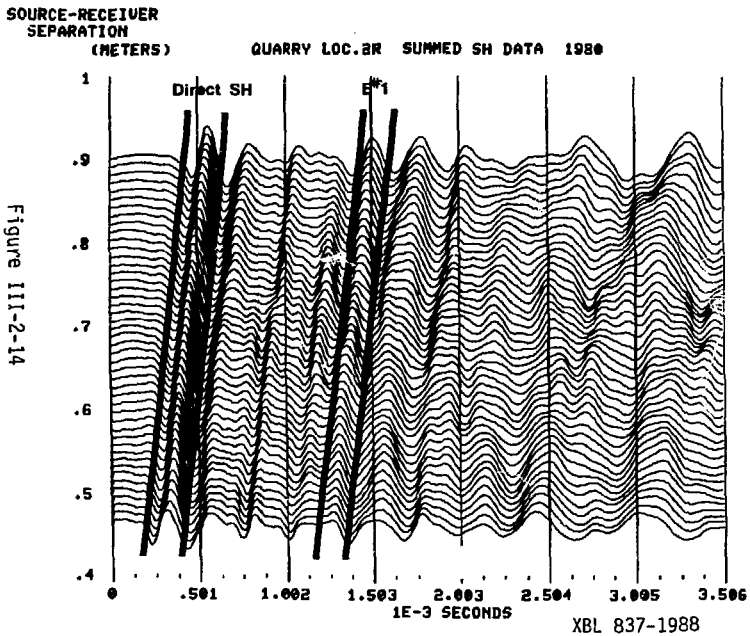

XBL 837-1988

Figure III-2-14

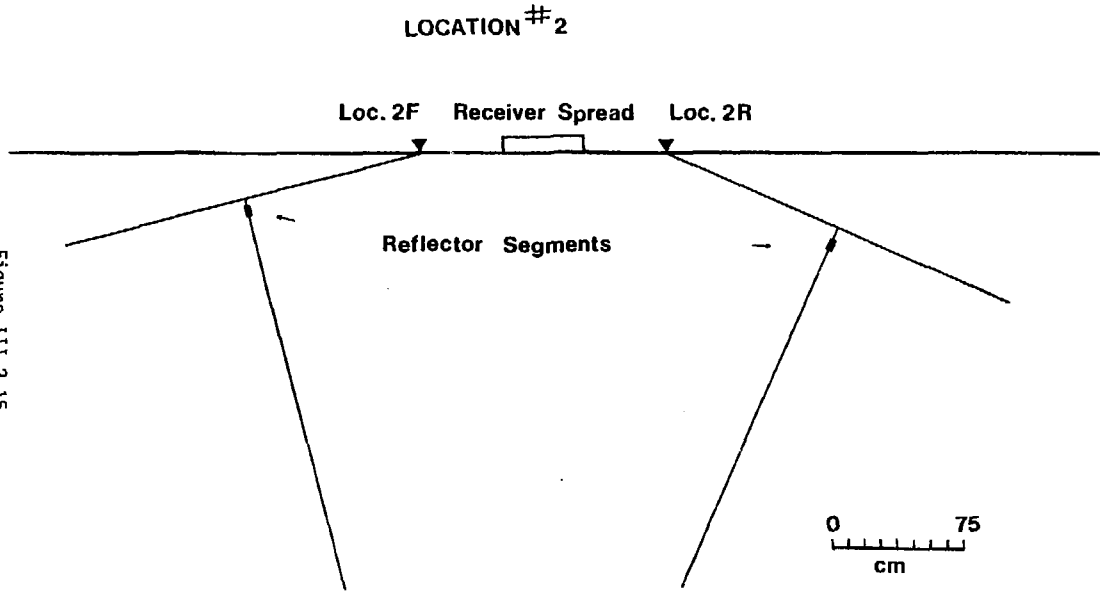

XBL 837-1989

Figure III-2-15

CHAPTER III

Section 3

Conclusions

Field experiments were performed in the late summers of 1979 and 1980 at an abandoned granite quarry in an attempt to detect in situ fractures using high-frequency SH reflection techniques. An ideal site was found (Figure III-1-(2 and 3)) where a fracture sub-parallel to an accessible observation surface can be expected to occur at a depth of 1-3 meters. Numerous SH reflection profiles were recorded at two locations on this observation face. Processing and analysis of these data were performed in a manner similar to those used in the laboratory reflection experiments.

A number of events arriving after the direct SH body wave were consistently observed in the SH profiles. X^2-T^2 fits of the arrival time data for these events were performed, and in each case the small value of the moveout velocity obtained from the X^2-T^2 fit indicated that the reflector had a significant amount of dip, with the receivers always downdip from the source. In this chapter the SH field data was interpreted using a model that assumes:

1) SH reflection from any sub-surface fracture is total, and,
2) the S velocity of the granite is homogeneous beneath each survey location.

Because of this first assumption, only event E#1 could be interpreted as a primary SH reflection from a sub-surface fracture. Events

occurring after E#1 could not then be considered as primary SH reflections from deeper fractures, and no further interpretation of these events was attempted. The dip angle and depth of the reflector associated with event E#1 were calculated separately for each SH profile using Equations III.2.(4 and 5). A homogeneous S velocity distribution is necessary so that the S velocity of the granite at a given profile location can be estimated from the X-T fit of the direct SH event. This constant S velocity estimate is necessary in calculating the dip angle and depth of the reflector.

The results of these calculations indicate that the observed arrival times of event E#1 at each of the two survey locations cannot be explained using only a single, planar, dipping fracture as a model. However, two planar fracture segments with opposing dips can be used to model consistently the arrival time data of E#1, and the fracture geometries at the two survey locations are shown in Figures III-2-(8 and 15). The positions of the reflector segments shown in these figures were derived using a graphical method described in Appendix I.

The irregular, steeply dipping nature of the fracture segments interpreted from the SH reflection data is not consistent with the relatively planar nature of the fractures observed in outcrop. Also, the down-dip interpretation required for event E#1 at each SH profile makes this interpretation somewhat suspect. Finally, the good X-T fits to the arrival time data of event E#1 suggest that this event may propagate nearly parallel to the observation surface. All of these factors taken together require that alternative interpretations of event E#1 be considered. A second model will be considered in which E#1 is interpreted

as a Love wave event. However, for chronological consistency, discussion regarding the Love wave model will be deferred until Chapter V.

The ambiguous results of the analysis of the SH field data using a dipping reflector model suggested that further laboratory experiments be performed to verify the assumptions inherent in this model. The results of experiments investigating SH reflection from a water-filled fracture and the variation of S velocity with water saturation of the Raymond granite will be presented in Chapter IV.

References--Chapter III

Aki, K. and Richards, P. G.; 1980; Quantitative Seismology: Theory and Methods; W. H. Freeman and Company; San Francisco; 932 pp.

Anderson, D. J. and Archembeau, C. B.; 1964; "The Anelasticity of the Earth"; J.G.R.; Vol. 69; pp. 2071-84.

Dobrin, M. B.; Introduction to Geophysical Prospecting; McGraw-Hill Book Company; New York; 1960; 446 pp.

Johnson, D. H. and Toksoz, M. Nafi; 1980a; "Ultrasonic P and S Wave Attenuation in Dry and Saturated Rocks Under Pressure"; J.G.R.; Vol. 85; No. B2; pp. 925-36.

Johnson, D. H. and Toksoz, M. Nafi; 1980b; "Thermal Cracking and Amplitude Dependent Attenuation"; J.G.R.; Vol. 85; No. B2; pp. 937-42.

Waters, K. H.; Reflection Seismology; 2nd Edition; John Wiley and Sons; New York; 1981; 453 pp.

Winkler, K. W. and Nur, A.; 1981; "Seismic Attenuation: Effect of Pore Fluids and Frictional Sliding"; Geophys.; Vol. 47; No. 1; pp. 1-15.